Polarization modeling and predictions for Daniel K. Inouye Solar Telescope, part 6: fringe mitigation with polycarbonate modulators and optical contact calibration retarders

David M. Harrington,[a,*] Sarah A. Jaeggli,[a] Tom A. Schad,[a] Amanda J. White,[b,c] and Stacey R. Sueoka[a]

[a]National Solar Observatory, Makawao, Hawaii, United States
[b]National Solar Observatory, Boulder, Colorado, United States
[c]University of Colorado, Department of Astrophysical and Planetary Sciences, Boulder, Colorado, United States

Abstract. Interference fringes are a major source of systematic error in astronomical spectropolarimeters. We apply the Berreman formalism with recent spatial fringe aperture averaging estimates to design and fabricate new fringe-suppressed polarization optics for several Daniel K. Inouye Solar Telescope (DKIST) use cases. We successfully performed an optical contact bond on a 120-mm-diameter compound crystal retarder for calibration with wavelength-dependent fringe suppression factors of one to three orders of magnitude. Special rotational alignment procedures were developed to minimize spectral oscillations, which we show here to represent our calibration stability limit under retarder thermal perturbation. We developed a fabrication technique to deliver low beam deflection for our large aperture polycarbonate (PC) retarders. Modulators are upgraded in two DKIST instruments with minimal beam deflection and bandpass-optimized antireflection coatings for fringe suppression factors of hundreds. We confirm that PC retarders do fringe as expected when low deflection is achieved. We show that increased retardance spatial variation from PC does not degrade modulation efficiency.
 [DOI: 10.1117/1.JATIS.6.3.038001]

Keywords: instrumentation; polarization; Mueller matrix; Daniel K. Inouye Solar Telescope.

Paper 19132 received Dec. 26, 2019; accepted for publication Jun. 4, 2020; published online Jul. 9, 2020.

1 Introduction

The National Science Foundation's Daniel K. Inouye Solar Telescope (DKIST) on Haleakalā, Maui, Hawaii, is presently finishing construction with early operations beginning around 2020. The telescope has a 4.2-m-diameter off-axis $F/2$ primary mirror with a 4.0-m-diameter beam. Four separate spectropolarimeters are being installed in the Coudé Laboratory, each with multiple sensors of various imaging capabilities and wavelength ranges.[1–3] All instruments have spectral resolving powers above 30,000 and achieve over 300,000 in many cases. Optics allow for stepping of spectrograph slits across a field of view, scanning through wavelengths with Fabry–Perot imagers or using imaging fiber bundles with scanning mirrors to create imaging spectropolarimetric capability over visible and near infrared wavelengths covering a range of narrow to wide fields of view. Many science cases require strictly simultaneous observation of several spectral lines with multiple instruments. DKIST is specified to simultaneously operate up to eight polarimetric cameras at frame rates of at least 40 Hz to achieve the spatial–spectral–temporal polarimetric goals.

DKIST uses seven mirrors to collect and relay light to a rotating Coudé Lab to provide flexible capabilities.[1,4–8] Four polarimetric instruments presently spanning the 380- to 5000-nm

*Address all correspondence to David M. Harrington, E-mail: dharrington@nso.edu

wavelength range are in various phases of construction or installation on the summit in the Coudé Lab. The visible spectropolarimeter (ViSP) is a three-arm spectropolarimeter. The visible tunable filter (VTF) is a tunable Fabry–Perot type imaging spectropolarimeter. The diffraction-limited near-infrared spectropolarimeter (DL-NIRSP) is a fiber-bundle fed imaging spectropolarimeter. We also have two high-speed cameras within the visible broadband imager red and blue instruments (VBI-red and VBI-blue). A sequence of dichroic beam splitters (and optionally windows or mirrors) called the Facility Instrument Distribution Optics (FIDO) allows for changing instrument configurations on a timescale of less than half an hour. The FIDO optics allow simultaneous operation of three polarimetric instruments optimized for 380 to 1800 nm while using the facility adaptive optics system for correction.[7–10] Another instrument called the cryogenic near-infrared spectropolarimeter (Cryo-NIRSP) can receive all wavelengths up to 5000 nm, but without use of the adaptive optics system. We refer the reader to recent papers outlining the various capabilities of the first-light instruments.[1,3,5,7,8] Complex polarization modulation and calibration strategies are required for multi-instrument astronomical systems.[7,8,11–14] The planned 4-m on-axis European Solar Telescope will also require similar calibration considerations.[15–17] Many solar and night-time telescopes have performed polarization calibration of complex many mirror pathways.[18–40]

This paper is part of a series investigating polarization performance expectations for the DKIST instrument suite. In HS17,[41] we outlined the DKIST optical layout and properties of a simple enhanced silver mirror coating model. This coating recipe was used in Zemax to estimate the field of view and beam footprint variation of the combined system optics to ViSP and Cryo-NIRSP. We also showed the predicted Mueller matrix for the DKIST primary and secondary mirrors, mounted ahead of the calibration retarders. In H17,[42] we showed polarization calibrations of a night-time telescope with a ViSP using the daytime sky. In H18,[43] we applied Berreman calculus[44,45] to polarization fringes formed in multilayer crystals with predictions and data collected in the lab and at a solar telescope. We then extended this calculus in HS18a[43] to include fringe magnitude estimates of converging and diverging beams. Fringes were measured at various focal ratios at solar and night-time telescopes as well as in the laboratory. We also showed thermal models for the DKIST retarders along with thermal perturbation models for the polarization fringes in HS18a.[43] We have recently investigated spatial variation of retardance across multilayer retarders made of polished crystals, stretched polycarbonate (PC), and Ferroelectric liquid crystals (FLCs) in HS18b.[46] This variation was then included in the DKIST optical model to show polarization calibration errors as functions of field angle and wavelength. We used a definition of calibration efficiency[47] to show a single calibration retarder can simultaneously and efficiently calibrate all DKIST instruments from 380 to 1650 nm, representing our entire first-light adaptive optics (AO) corrected suite.

In H19,[48] we extend the coating efforts of HS17[41] to many mirror types from multiple vendors, highly enhanced metal coatings, hundred-layer dichroic coatings, and our system of beam splitters. Coating samples were measured for every mirror in the DKIST and relay optics as well as every optic presently coated within the instruments ViSP, Cryo-NIRSP, and DL-NIRSP. We also know the design formulas and have measured all the FIDO dichroics and antireflection coatings. We created a coating model using data for all optics in the DKIST and most of the first light instrument suite along with system-level predictions for polarization performance.

As we have refined our system model for DKIST polarimetry through the previous series of articles, we have recognized the significant influence that interference fringes have on the achievable polarization accuracy. It is well known that fringes negatively impact polarization accuracy, and various projects have worked toward optical fringe modeling[49–55] and/or postfacto removal methods[56–59] to help mitigate their impact. Other design strategies include designing retarders such that fringes are unresolved and average below detection limits[29,60] or using wedged windows for fringe reduction on nonrotating retarders.[28,40] Our work in H18[43] and HS18a[43] indicated that the original multilayer crystal retarders build for DKIST have spectrally dependent fringe characteristics that pose particular challenges to achieve high accuracy. In this paper, we present the design and fabrication of newly upgraded polarization optics based on PC and optically contact crystal designs that suppress polarization fringes by one to three orders of magnitude compared to the previously designed multilayer crystal optics.

A major challenge here is the fabrication of very large (120-mm diameter) retarders that simultaneously achieve wide wavelength range efficiency, low-interference fringe magnitudes, spatial retardance uniformity, transmitted beam deflection <10 arc sec, and thermal stability in spectral bandpasses <1 nm wide. We show here that crystal alignment errors create spectral retardance oscillations that become the major stability limit under thermal perturbation. We designed a large aperture PC retarder and collaborated with a vendor to develop special lamination procedures to achieve beam deflection roughly 60 times better than typical products. We also developed a large area optical contact retarder along with accurate crystal clocking orientation procedures to produce a calibration retarder with low thermal drifts operating in our 300-W optical beam.

Berreman[44] formulated a 4×4-matrix method extending thin-film calculations by Abeles and Heavens matrices.[55] This Berreman calculus can be used to describe wave interference in multiple birefringent layers, crystals, chiral coatings, and other complex optical configurations with many birefringent layers of arbitrary optical axis orientation (c.f., McCall, Hodgkinson, and Wu[45]). We apply the Berreman calculus for collimated beams with our beam focal ratio fringe scaling relation[43] to estimate fringe magnitudes from every component internal to each retarder in both the DKIST calibration optics and the three first-light instruments ViSP, DL-NIRSP, and Cryo-NIRSP. We also include fringe estimates for the VTF modulator, which will combine with DKIST calibration optics. VTF has especially strong coupling between calibration accuracy and the spectral retardance oscillations from calibration retarder alignment errors due to the temporal scan in wavelength. We also extensively use our Mueller matrix spectral measurement system called the National Solar Observatory Laboratory Spectropolarimeter (NLSP) to show spatial and spectral properties of the many DKIST polarization components.[43,46,48]

In this work, we follow standard notation for propagation of polarization through an optical system. The Stokes vector is denoted as $\mathbf{S} = [I, Q, U, V]^{\mathrm{T}}$. The Mueller matrix is the 4×4 matrix that transfers Stokes vectors.[61–63] Each element of the Mueller matrix is denoted as a transfer coefficient.[63,64] For instance, the coefficient [0,1] in the first row transfers Q to I and is denoted QI. The first row terms are denoted II, QI, UI, and VI. The first column of the Mueller matrix elements are II, IQ, IU, and IV.

2 Fringe Suppression in Polycarbonate Modulators

We designed a large aperture three-layer PC retarder modulator for the DKIST ViSP instrument covering the 380 to 950 nm wavelength range to suppress fringes and improve the optical quality of the instrument. We contracted Meadowlark Optics (MLO) to fabricate this optic following our design. We collaborated on improving the PC retardance model by procuring samples from MLO. We compared our own elliptical retardance measurements with new elliptical retardance capabilities created at MLO for this project. We then reoptimized the design. Details can be found in Appendix B.

We mitigate fringes by utilizing thick cover windows, broad-band anti-reflection (BBAR) coatings, and refractive index matching between optical components including the adhesives, windows, and PC. We were also required to achieve transmitted beam deflection of <10 arc sec, as opposed to the few arc minute best-effort type values common for this type of laminated retarder. We present details of the refractive index models and optical material choices in Appendix A. The cover windows are a BK7 equivalent Ohara S-BSL7 with a diameter of 120 mm $\pm$ 0.3 mm to match the diameter of the cell in the existing DKIST modulator rotation stages. The clear aperture is nominally 105 mm. Thickness was specified as 14 mm $\pm$ 0.5 mm before coating and polishing as this is close to the maximal thickness that can fit in the cell, maximizing fringe suppression. The nominal surface quality before coating was 40/20 scratch-dig to avoid defects detectable in the system flat field to errors below 0.01%. The individual BK7 windows had a beam deflection below 5 arc sec each. The final assembly had a deflection of 2.3 arc sec after lamination.

In Table 1, we show the optical model used in the collimated beam at normal incidence in our Berreman code for fringe computations.[43,46,65] The title polyPCM denotes a PC polychromatic modulator. We show the coatings as a single row on both air–glass interfaces. The coating is a 14-layer design with a 0.64-μm total thickness. The initial thin strippable layer (<20 nm) is

Table 1 ViSP polyPCM model layers.

Layer	T (μm)	Description
Coating	0.6	14 lyr BBAR
S-BSL 7	14179.0	BK7 window
Adhesive	13.5	Summers P92
PolyCarb1	73.5	158 deg at 0 deg
Adhesive	13.5	Summers P92
PolyCarb2	73.5	107 deg at 40 deg
Adhesive	13.5	Summers P92
PolyCarb3	73.5	158 deg at 146.5 deg
Adhesive	13.5	Summers P92
S-BSL 7	14184.0	BK7 window
Coating	0.6	14 lyr BBAR

lyr, Layer.

followed by 12 oscillating $SiO_2 - Ta_2O_5$ layers with a thicker outer MgF_2 layer. After coating, a Heidenhain linear thickness gauge showed a 14.179-mm thickness for the first window and 14.184-mm thickness for the second window, both measured outside the clear aperture. The PC layers were nominally 73.5-μm thick with a measured variance of only a few microns. We tested several bonded window pairs for the Summers P92 adhesive. We measured P92 adhesive thicknesses in the range of 12 to 15 μm with an average of 13.5 μm.

We first compute the fringed Mueller matrix of the pPCM model (Table 1) using our Berreman calculus scripts but without the outer BBAR coatings and for the case of a collimated beam. In Fig. 1(a), we show ER parameters fit to the Mueller matrix computed in transmission for an uncoated air–glass interface with elliptical fringes at magnitudes of over 10 deg. Figure 1(b) shows the IQ, IU, and IV elements of the Mueller matrix with diattenuation fringes at $\pm 10\%$. The application of antireflection coatings will significantly reduce the fringes. The fringe spectral period becomes quite small with thick cover windows, separating the fringe frequency from typical solar signals and reducing the detected fringe magnitude when the instrument does not spectrally resolve the fringe.

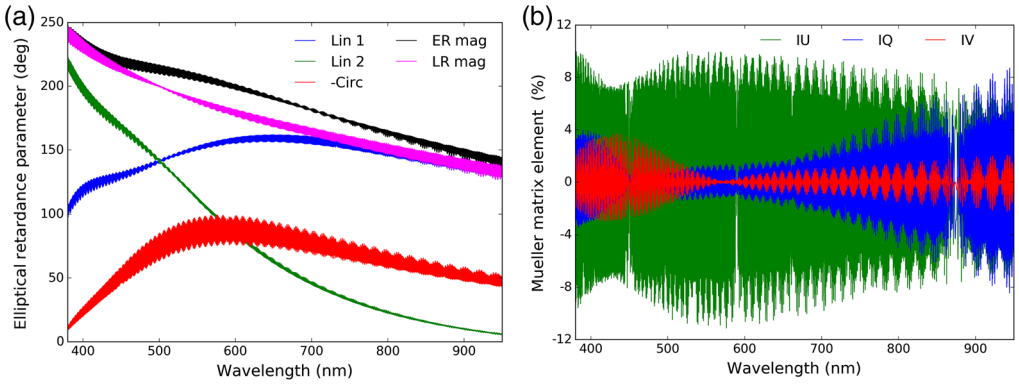

Fig. 1 Berreman calculations for fringes in (a) retardance and (b) diattenuation. The three elliptical retardance parameters (Lin1, Lin2, and Circ) are shown along with the full ER magnitude (ER Mag) and the linear retardance magnitude (LR Mag). The diattenuation elements of the Mueller matrix are shown as IQ, IU, and IV. Both graphics model uncoated cover windows and a collimated beam. We could only plot the data down-sampled to $R = 100$ K though the simulation was computed at $R = 10,000$ K. Some apparent gaps in the fringe data sets are sampling artifacts.

2.1 *ViSP Fringe Predictions: Spectral Sampling and F/32 Marginal Ray Optical Path Difference (OPD)*

The fringes were designed to be spectrally fast by making the BK7 cover windows thick. This should significantly reduce the fringe magnitude as spectral variation is within a factor of a few of the spectral profile full-width at half-maximum delivered by the optics. In Fig. 2, we show the spectral fringe period at left and the optical sampling per spectral profile full-width at half-maximum (FWHM) at right for spectral resolving powers of 100 K, 200 K, and 300 K. As an example, the fastest spectral period for the full stack of optics in the modulator is at 1.76 picometers (pm) for the 393-nm wavelength. An $R = 300$ K spectrograph (ViSP) would provide an optical FWHM of 1.31 pm, and thus sample the 1.76-pm spectral fringe with a 1.31-pm FWHM optical beam giving 1.34 optical samples per fringe period.

The optical path length difference between the chief and marginal rays provides the additional spectral fringe reduction through averaging spatially over the beam footprint as shown in H18a.[43] The Berreman calculus is limited to collimated beams of infinite spatial extent. As is common with thin-film calculations for filters, the Berreman calculations are first run over a range of incidence angles. These collimated beam calculations are interpolated spatially over an aperture-weighted range of angles to approximate behavior in noncollimated beams. We followed the simple scaling relation where spectral fringe magnitudes decrease as the inverse square of the marginal ray path with a half-wave offset as derived in our lab measurements of H18a.[43] We considered a thin window where we can neglect the incomplete overlap between the back-reflected beam and the incoming beam. In this situation, we recover a simple division of amplitude type interferometer for fringes of equal inclination also called Haidingers fringes. Detailed descriptions are in several optical textbooks including Born and Wolf Chapter 7[66] and Hariharan Chapter 2.[67] In particular, Born and Wolf, 6th edition, Chapter 7.5, Eq. (2) calls out the marginal ray path in the medium as $d/\cos\theta_g$, where the substrate thickness (d) is divided by the incidence angle refracted into the medium ($\cos\theta_g$) for the fringes localized at infinity. The optical path difference between the first surface reflected component of the marginal ray and the marginal ray component reflecting off the back surface (immersed) is $2dn\cos\theta_g$ after compensation for the path traveled in air by the first surface reflected component to form an outgoing parallel wavefront.

The ViSP modulator is located in the diverging $F/32$ beam about 260 mm of propagation past the spectrograph entrance slit. Each individual field angle imaged by the spectrograph

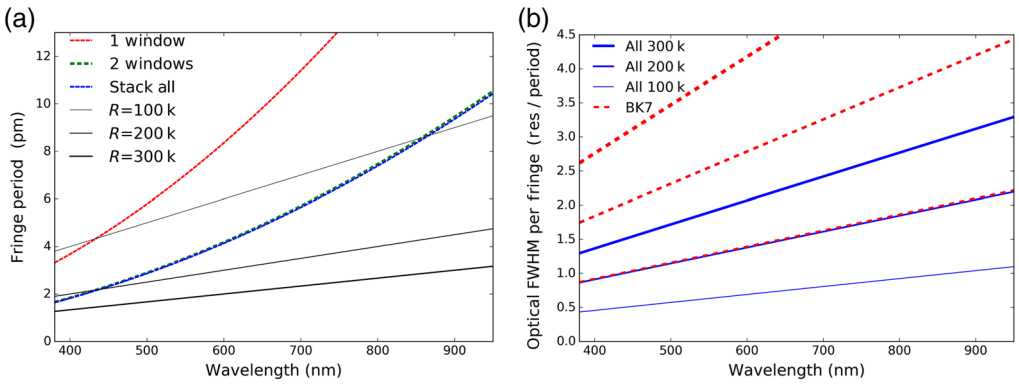

Fig. 2 (a) Fringe periods computed for the various optics in the stack as dashed colored lines. The optical FWHM for a spectrograph at resolving powers of 100 K, 200 K, and 300 K are shown as solid black lines of varying thickness. (b) How many optical FWHM units sample the spectral fringe for a spectrograph working at resolving powers of 100 K, 200 K, and 300 K. Blue shows the full stack of optics in the modulator. Red shows just a single 14.2-mm BK7 window. Thinner red lines denote lower resolving power and are not noted in the legend. Note the $R = 100$ K case for the single BK7 window as the thick dashed line goes off scale but peaks at a 21-pm spectral fringe period and 6.65 optical FWHM samples per 21 pm fringe period at $R = 300$ K for the thickest red dashed line at right.

Table 2 ViSP PolyCarbPCM fringe properties: sampling and OPD $F/32$.

Description	393 nm	486 nm	630 nm	854 nm
FWHM 300 K (pm)	1.31	1.62	2.10	2.85
FWHM 100 K (pm)	3.93	4.86	6.30	8.54
Waves thick full stack	223,626	179,703	137,964	101,409
Marg.–chief $F/32$	11.6	9.5	7.3	5.4
Fringe period full stack (pm)	1.76	2.70	4.57	8.42
Optical samples at 300 K	1.34	1.67	2.17	2.96
Optical samples at 100 K	0.45	0.56	0.72	0.99
Waves thick BK7 window	110,696	88,962	68,303	50,208
Marg.–chief $F/32$	5.8	4.7	3.6	2.7
Fringe period (pm)	3.55	5.46	9.22	17.01
Optical samples at 300 K	2.71	3.37	4.39	5.98
Optical samples at 100 K	0.90	1.12	1.46	1.99

illuminates an 8.1-mm-diameter circle on the modulator entrance. Table 2 shows a compilation of fringe periods, marginal ray optical path properties, and spectral sampling anticipated for the ViSP. We list the number of optical spectral profiles (in per FWHM units) sampling a fringe period with a spectrograph of resolving powers 100 K and 300 K in the top two rows. We then create two sections below showing optical properties for spectral sampling and focal ratio behavior. The BK7 section on the bottom corresponds to a single 14.2-mm-thick cover window. The middle section of Table 2 corresponds to the entire stack: two windows, three PC layers, and four epoxy layers. The difference between the longer marginal ray path and the shorter chief ray path after a double-pass through the substrate for a marginal ray at some incidence angle is easily computed as $(1-\cos\frac{\theta_{\text{air}}}{n})\,2dn/\lambda$, where n is the refractive index, λ is the wavelength, and θ_{air} is the incidence angle in air. We make the small angle (paraxial) approximation for Snells Law refracting from θ_{air} in air to $\theta_{\text{air}}/n=\theta_g$ in the glass substrate. The incidence angle for the marginal ray is easily computed as $\tan^{-1}(\frac{1}{2F})$ for a beam focal ratio F. The bottom section of Table 2 corresponds to a single BK7 cover window.

In each section of Table 2, we show the substrate optical thickness for the back-reflected chief ray in waves for the rows labeled waves thick, including the double pass through the optic. The optical path length difference through the substrate in waves between the marginal and chief rays is shown in the rows labeled Marg–Chief $F/32$ in double-pass. For the ViSP modulator at a focal ratio of 32, the marginal ray is at 0.895-deg incidence in air, subsequently refracted to 0.597 deg for $n=1.5$ material. We note that the small angle approximation is valid to one part in 10^5 for this $F/32$ beam. We then show the number of spectral profile FWHMs that optically sample the spectral fringe at spectral resolving powers of 300 K and 100 K. These rows approximate the optical sampling of a spectral fringe period, with the expectation that low sampling will correspond with significant spectral averaging of a fringe within an optical profile.

An example, at a 486-nm wavelength, the chief ray back-reflected through the full modulator optical stack sees 179,703 waves of optical path. The marginal ray for the $F/32$ beam sees an additional 9.5 waves of optical path length on back reflection through the same stack. A single BK7 window would be 88,962 waves for the back-reflected chief ray. The back-reflected marginal ray will emerge from the front of the optic with a spatial offset of 0.44 mm from the incoming marginal ray through a single window and 0.89 mm through the stack. The diverging $F/32$ beam footprint expands from 8.1-mm diameter to 9.9 mm, increasing in size by 20%.

These interference estimates ignore the finite beam size and represent an upper limit. The ViSP would deliver an optical profile of 1.62 pm FWHM at a spectral resolving power of 300 K. The single window fringe period is 5.46 pm and the fastest period from the full stack is 2.70 pm. The dispersion and spectral sampling of ViSP are quite complex, depending on grating orientations, camera configurations, and other optical parameters. But spectral sampling is roughly 1 pm per spectral pixel and thus ViSP could expect to see fringe periods at 2.7-pixel and 5.5-pixel periods. These fringes would be substantially smoothed by convolution with an optical profile of 1.6 pm FWMH, further reducing detected fringe magnitudes.

2.2 *ViSP Fringes Mitigated with Many Layer Coatings and Beam* F*/Number*

Here, we consider the combined benefits of this new PC retarder by comparing it against the six-quartz crystal super achromatic retarder (SAR) nominally built for this instrument as we have described previously.[43,46,65] We compare the broadband antireflection coatings on the PC retarder against the single-layer MgF_2 coating on the quartz retarder. Fringe amplitudes are approximated as $4R$, where R is the single-surface reflectivity for a highly transparent plane parallel window with fringe reduction due to the incident F-number per HS18a.[43] We also compare the internal adhesive index matched to the BK7 with the $n = 1.3$ oil used in between the six quartz crystals on the older optic. Figure 3(a) shows the predicted fringe magnitude for a collimated beam compared to an $F/32$ beam for a range of interfaces. Solid lines show fringe magnitudes for a collimated beam. Dashed lines show fringe magnitudes scaled by the r^{-2} spatial fringe average we approximated (see HS18a[43]). Figure 3(b) shows the fringe reduction factors in an $F/32$ beam for 28 mm of BK7 of the PC retarder and compares this with 12.8 mm of crystal quartz and 2.1 mm of crystal quartz for the six-crystal retarder. The optics are coated on both sides for these fringe calculations.

In Table 3, we compile values for some fringe magnitudes and $F/$number fringe reduction properties. We show the new PC modulator in the top section to compare with the six-crystal optic in the bottom section. The first column shows the interfaces between air or oil and the optical elements of BK7 or crystal quartz. Coatings are denoted with a lower case 'c.' The crystals have the single-layer isotropic MgF_2 antireflection coatings (CQc), whereas the BK7 has the many layer coatings. In the PC modulator, the internal BK7 interfaces are uncoated and

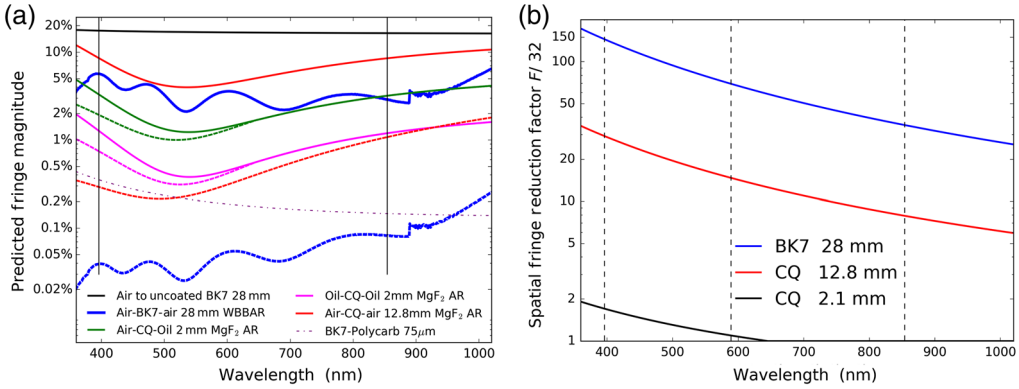

Fig. 3 (a) Fringe magnitudes predicted from coating reflectivity measurements for the both side coated optics in a collimated beam as solid lines. Dashed lines show fringe magnitudes for each optic reduced by the marginal ray path estimates of HS18a.[43] Comparing solid to dashed lines of the same color shows fringe magnitude reduction. The nominal runs had a bandpass averaged reflectivity around 0.72%. (b) The spectral fringe reduction factor derived with the r^{-2} scaling envelope for the spatial fringe average from HS18a.[43] Blue shows 28 mm of BK7, the full thickness of the PC modulator. Red shows 12.8 mm of crystal quartz, the nominal six-crystal modulator thickness. Black shows 2.1 mm of crystal quartz, the thickness of an individual crystal within the modulator. Vertical dashed black lines show common observing wavelengths of 396, 589, and 854 nm.

Table 3 Fringe magnitudes collimated versus $F/32$.

Optical interfaces	λ	Col	$F/32$	Fact.
Enter—optic—exit	nm	%	%	
		PolyPCM		
Air–28-mm BK7c–air	396	5.68	0.04	144
Air–28-mm BK7c–air	854	2.90	0.08	35
BK7–PolyCarb–BK7	396	0.35	0.35	—
BK7–PolyCarb–BK7	854	0.15	0.15	—
		Crystal quartz		
Air–12-mm CQc–Air	396	8.49	0.29	29
Air–12-mm CQc–Air	854	8.55	1.09	7.9
Air–2-mm CQc–oil	396	3.27	1.92	1.7
Air–2-mm CQc–oil	854	3.20	3.20	—
Oil–2-mm CQc–oil	396	1.26	0.74	1.7
Oil–2-mm CQc–oil	854	1.20	1.20	—

interface to PC through the adhesive. As an approximation for this table, we ignore the simultaneous solution of all coherent reflections following the Berreman calculus. We simply approximate each layer as if it was alone and free standing. For instance, oil–2-mm CQc–oil would be the fringe magnitude for the quartz crystal antireflection (AR) coated on both sides immersed in $n = 1.3$ oil.

The second column shows the wavelength for each row. The third column shows the fringe magnitude for the collimated beam (Col) for comparison with solid lines in Fig. 3(a). The fourth column shows the peak fringe magnitude predicted with the r^{-2} envelope scaling to $F/32$. The fifth column shows the fringe reduction factor for that particular wavelength and $F/$number for the particular optic producing individual fringes.

The black curve in Fig. 3(a) shows the fringe magnitudes of 16% to 18% for an uncoated BK7 window in air with a collimated beam. As measured in the lab, fringe magnitudes in transmission windows are well approximated by $4\sqrt{R_1}\sqrt{R_2}$ for the reflectivity of both surfaces R_1 and R_2. The blue curve takes reflectivity measurements from Infinite Optics Inc. (IOI) on BK7 samples at an 8-deg incidence angle and shows fringes from both coated BK7 windows at few percent magnitudes when in a collimated beam. The dashed blue line shows the additional impact of an $F/32$ beam and the 28-mm-thick windows reducing this fringe magnitude by factors of 20× to over 150× at the shorter wavelengths. Red shows the fringe magnitude corresponding to the air to crystal quartz to air interface where the quartz is coated with a single 97.2-nm-thick isotropic MgF_2 AR coating on both sides. This corresponds to a quarter wave at a 525-nm central wavelength and gives rise to the coating reflectivity minimum measured on the coating witness samples. The air-quartz-air interface represents the full 12.8-mm thickness of the entire six-crystal retarder stack. Green shows a single 2.1-mm-thick crystal quartz retarder but with an interface to the oil at a refractive index of roughly 1.3 used in the assembly of the six-crystal modulator. The first and last crystals are modeled as air to coated crystal to oil. Magenta in Fig. 3(a) shows this same AR-coated crystal quartz but now immersed in oil representing the interior crystals in the stack. The single dot-dashed magenta line shows the internal interface between PC and BK7. Because the individual adhesive layers are 13-μm thick and the PC is only 75-μm thick, there is no change in the $F/32$ beam.

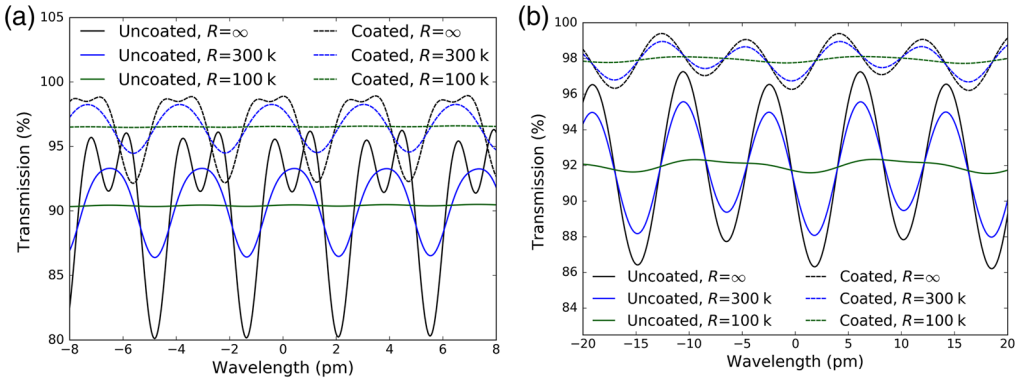

Fig. 4 Fringes in transmission for the ViSP PC retarder for (a) 393-nm wavelength and (b) 854-nm wavelength. Black shows infinite spectral resolving power sampled at $R = 10{,}000$ K. Blue shows convolution with a Gaussian profile to simulate an $R = 300$ K spectrograph. Green shows $R = 100$ K convolution. The dashed lines show the same resolving power calculations, but now with AR coatings applied to both air–glass interfaces of the BK7 cover windows. Transmission is increased and fringe magnitudes are reduced for the same resolving power.

2.3 *ViSP Berreman Fringe Modeling: Coatings and Degraded Resolving Power*

The limited spectral resolving power of ViSP will further reduce the measured fringe magnitudes for this new PC upgrade mounted within the ViSP instrument. This PC modulator was designed to make the fringes have very small spectral periods, reducing the detected fringe magnitude. We perform a spectral analysis where we convolve a Gaussian instrument profile with the Berreman models to simulate the reduced fringe magnitudes. This is similar to the simulations published in HS18a[43] from Appendix D on the Keck Telescope LRISp six-crystal modulator fringes. In Fig. 4, we show transmission fringes at wavelengths of 393 nm in (a) and 854 nm in (b). In each, we convolve with a Gaussian profile corresponding to a spectral resolving power of 300,000 and 100,000, respectively, to our model computed at spectral sampling of one part per 10 million. The black lines show infinite spectral resolving power transmission fringes. The blue lines show $R = 300$ K. The green lines show $R = 100$ K. Figure 4(a) shows the 393-nm wavelength. The single window fringe and full stack fringe at $R = 100$ K have roughly 1 and 2 fringe cycles per optical profile, respectively, leading to large suppression factors between black and green curves. For the $R = 300$ K mode, ViSP has 1.34 and 2.71 optical profiles per fringe period. This marginally resolves the faster fringe. The black and blue curve differences show the faster period fringe is substantially suppressed. Figure 4(b) shows the 854-nm wavelength. There is very substantial fringe reduction for $R = 100$ K, but with oscillations observable in the green curves. ViSP has 3 and 6 optical profiles per fringe period at $R = 300$ K for this graphic and only a small reduction between black and blue curves is seen.

2.4 *ViSP Polycarbonate Modulator: Thermal Stability Comparison with ViSP SAR*

Temperature sensitivity is a major concern for the stability of a retarder. We show here that clocking errors between multiple crystals of the old six-crystal quartz retarder are larger and more spectral and complex than for PC retarders. Layer clocking tolerances below 1 deg are often not achieved in common multicrystal retarders. PC retarder sheets drawn from the same batch as the ViSP modulator PC have been measured at MLO to characterize their temperature sensitivity. We compare this PC retarder to the previous six-quartz crystal retarder to compare the thermal stabilities of the different approaches

$$\mathrm{OP} = d(1 + \alpha\Delta T) \quad n(1 + \mathrm{TOC}\Delta T). \tag{1}$$

There are three contributing factors to retardance dependence on temperature. First is physical expansion through the coefficient of thermal expansion (CTE). Linear expansion coefficient, $\alpha = (1/\mathrm{L})\ \mathrm{d}L/\mathrm{d}T$, is a normalized expansion coefficient with units of (1/°C), which multiplies the optic physical thickness to compute the thermally perturbed thickness. Second is the change in refractive index with temperature through the thermo-optic coefficient ($\mathrm{d}n/\mathrm{d}T$, TOC). Third is the dependence of crystal birefringence on temperature $[\mathrm{d}(n1 - n2)/\mathrm{d}T]$. All three parameters cause the fringes and spectral retarder properties to change per Eq. (1).

MLO has measured retardance with temperature for a wide variety of polymers types. Typical polymers like PC and polyvinyl alcohol are positive birefringent materials. Typical values are in the range of 0.02% to 0.04% retardance change per °C. Other polymers like polystyrene are negative birefringent with negative retardance changes with temperatures at similar magnitudes. Polymer CTE is commonly an order of magnitude larger than typical glasses and the thermo-optic coefficient is similarly large. See the *Handbook of Plastic Optics*,[68] *Handbook of Thermo-Optic Coefficients*,[69] and others.[70–72] We used α of 13.5 in parts per million for our six-crystal quartz modeling efforts in HS18b.[43] We continue the results of HS18b (Sec. 5) in this paper to create thermal simulations comparing this new ViSP PC optic to the six-quartz crystals. We note that birefringent crystals have different CTE values in the ordinary and extraordinary directions and we adopt the same parameters as in HS18b.[43]

A ViSP PC modulator sheet was measured at MLO to have 232.0-nm phase retardance at the 402-nm wavelength and 291.7-nm phase at the 1009-nm wavelength. This corresponds to 0.577 wave and 0.289 wave retarders at short and long wavelengths, respectively. They measured a 4.9-nm retardance phase change at the 1009.3-nm wavelength and a 4.0-nm retardance phase change at the 402.4-nm wavelength in 45°C of heating from 25° to 70°C. Measurements were done every 5°C of heating. Both the retardance change in the phase and the relative retardance change in % are shown in Fig. 5(a). The black curves show the retardance relative birefringence change rising by roughly 1.7% after heating by 45°C. The blue curves use the righthand Y axis and show the retardance phase change. The relative birefringence and retardance changes with temperature are achromatic to more than three decimal places over this bandpass. The retardance changed by 1.7% at both wavelengths. A polynomial fit to many measurements of retardance versus temperature also showed the behavior was linear.

We can compare the thermal stability of this PC three-layer true zero-order retarder with that of a six-crystal SAR nominally designed by DKIST for ViSP. See Sec. 5 of HS18a[43] and HS18b[46] Tables 2, 4, 8, and Fig. 16. The thermal stability of the DKIST Coudé Laboratory at ±1°C was used to create a predicted retardance variation in the two modulators for comparison. Figure 5(b) shows a ±1°C perturbation on the nominal PC modulator design modeled as a 0.038% retardance scale factor in each layer. The retardance changes in the three-layer stack are wavelength dependent. The three-layer stack elliptical magnitude and individual components

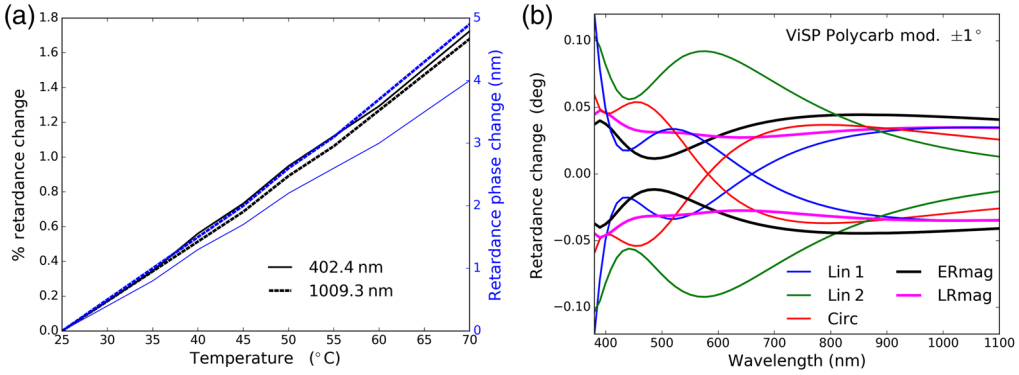

Fig. 5 (a) The measured PC retardance change with temperature at two wavelengths: 402.4 and 1009.3 nm. Black lines show the % retardance change using the left-hand Y axis. Blue lines show the retardance phase change in nm using the blue righthand Y axis. (b) A model of the ER change on the ViSP PC modulator from a ±1°C temperature perturbation when using a linear trend from the left-hand graphic. Black shows the elliptical retardance magnitude. Magenta shows the linear retardance magnitude. Blue, green, and red show the axis-angle ER parameters.

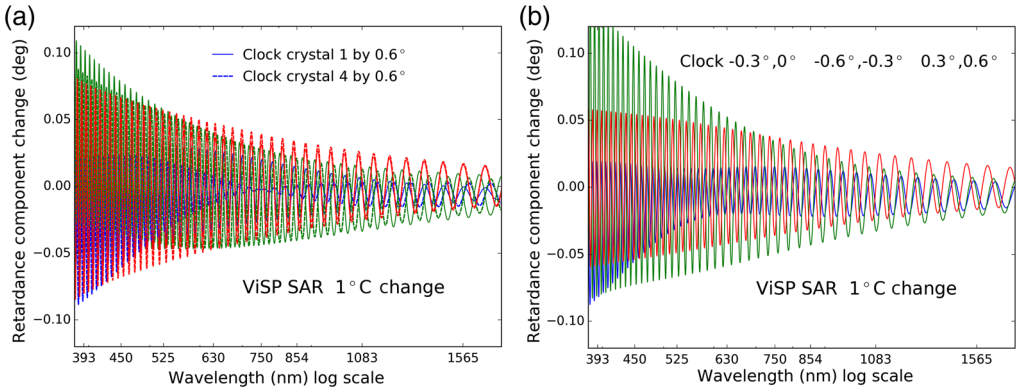

Fig. 6 Thermal change of the ER parameters for different scenarios of clocking error for a temperature change of 1°C. (a) A 0.6-deg clocking offset for crystal 1 as solid lines and crystal 4 as dashed lines. (b) A scenario where five of the six crystals are perturbed to produce clocking errors of magnitude 0.3 deg in each compound pair. The modeled temperature change within a few minutes of illumination is <1°C. Blue, green, and red show the three axis-angle ER parameters linear1, linear2, and circular, respectively.

change widely. Individual layer retardance magnitudes change by 0.1 deg at the shortest wavelengths and <0.05 deg at the longest wavelengths of Fig. 5.

The six-crystal super achromatic designs consist of three compound retarders. Two crystals of nearly identical thickness are oriented with fast axes crossed in what is called subtraction orientation. This largely compensates for thermal perturbations. The major instability with these super achromats is the imperfections in crystal alignment producing spectral oscillations in retardance that is much more thermally sensitive than the nominal design itself. As we have shown in HS18b,[46] the DKIST designs are very well compensated for bulk temperature changes when the individual compound crystals are perfectly clocked (aligned rotationally). However, thermal gradients with depth through the optic can cause issues. The clocking oscillations introduced by a 2-mm-thick crystal misaligned by even 0.3 deg can cause spectral oscillations of over 1-deg elliptical retardance with temporal changes larger than the PC and with very strong spectral dependence. The supposed thermal compensation of SAR designs is lost for narrow-band instruments for SARs fabricated with even relatively tight clocking alignment tolerances. Figure 6 shows an example of the thermal instability of the clocking oscillations for the six-crystal ViSP optic. We showed in HS18b[46] Figs. 4, 16, and 27 some of the clocking errors measured in the DKIST six-crystal retarders. We illustrate the impact of a 0.6-deg offset of two crystals in Fig. 6(a). We show a thermal simulation with an improved manufacturing tolerance error of ±0.3 deg on each crystal in Fig. 6(b). In both cases, we use a uniform temperature change of 1°C from each model to show the perturbation of elliptical retardance components. We note that these simulations are factors of 2 or 3 better in clocking alignment than typical fabrication contracts we have seen.

2.5 *ViSP Polycarbonate Spatial Maps: MLO ER versus NLSP Mueller Matrix*

MLO performed spatial maps of the elliptical retardance (ER) as part of acceptance testing. We compare these spatial retardance maps with our spatial and spectral data collection in our NSO laboratory spectropolarimeter NLSP described in HS18b[46] and H19.[48] This represents a direct comparison between results of our systems proving our Mueller matrix fitting technique produces accurate results. The MLO system is a scanning monochromator retardance only measurement system. Our NLSP is two-fiber fed Czery-Turner spectrographs measuring the full Mueller matrix. The MLO retardance mapping set up used a scanning monochrometer with a rectangular grid of points with a 3-mm-diameter beam stepped to cover a circular area with a 108-mm-diameter aperture collecting 1167 independent ER measurements. We follow the procedure outlined in Appendix B.4 to convert their ER measurements in a three-angle matrix convention to our axis-angle convention using a fit to the Mueller matrix. MLO performed maps at

two separate wavelengths anticipated to be popular ViSP observing wavelengths: 396 and 854 nm. We compare these MLO retardance maps at a single wavelength to our spatial mapping with the NLSP Mueller matrix spectra. We create spatial retardance maps from the NLSP Mueller matrices collected in three maps from September 2019. Two maps used a 5.0-mm-diameter mask attached to the lens tube holding the collimating lens on the collimated beam side. The third map used a 3.5-mm-diameter mask. The first map used a spatial sampling pattern with a 6-mm radial step and a final radius of 30 mm for 90 spatial samples. The second map utilized a Hoya LB-140 color balancing filter on the spectrograph side to assess data accuracy covering a 48-mm radius and 217 spatial samples. The third map used a higher density Hoya LB-200 filter, a reduced 3.5-mm beam diameter, and a higher spatial density map covering 30-mm max radius with a 3-mm step size and a 3-mm ring step. All maps used 60-deg angular sampling for the first annulus decreasing as x^{-1} with each subsequent ring.

We show the interpolations of the MLO ER parameters after conversion to the axis-angle convention in Fig. 7(a)–(c). We compare MLO maps to NLSP maps at the same wavelength on the bottom row. Note that the aperture and optic orientation are slightly different between MLO and NLSP. In Fig. 8, we show the MLO data set at the 854-nm wavelength. Similar agreement between MLO and NLSP results are seen at this wavelength as well. However, the spatial form of

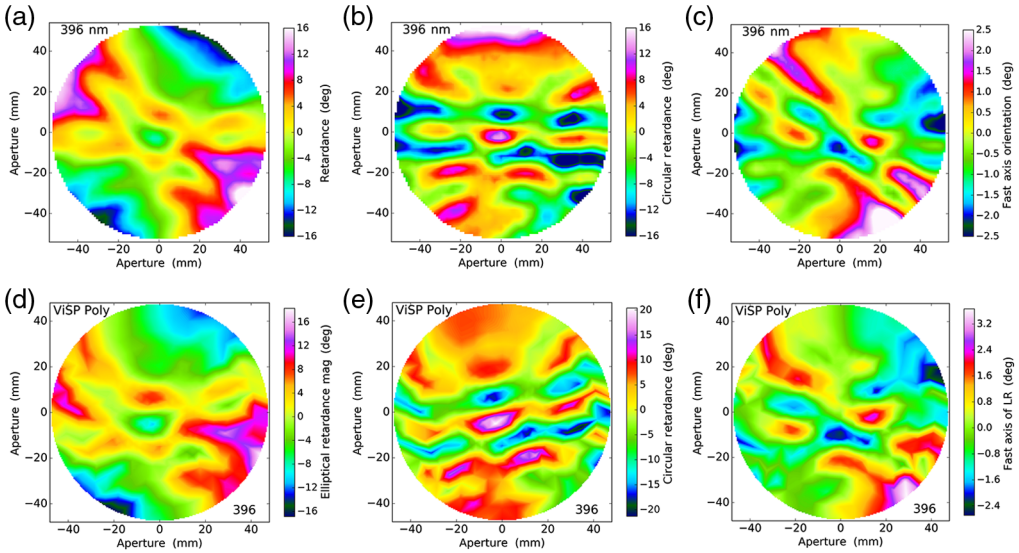

Fig. 7 Spatial variation of retardance across the ViSP PC three-layer retarder at 396-nm wavelength: (a)–(c) Meadowlark spatial maps and (d)–(f) NLSP mapping at the same wavelength. (a), (d) Spatial variation of ER magnitude; (b), (e) the spatial variation of circular retardance; and (c), (f) spatial variation of the fast axis of linear retardance. Note that the color scale, spatial sampling, total aperture, and optic orientation are slightly different between MLO and NLSP data sets.

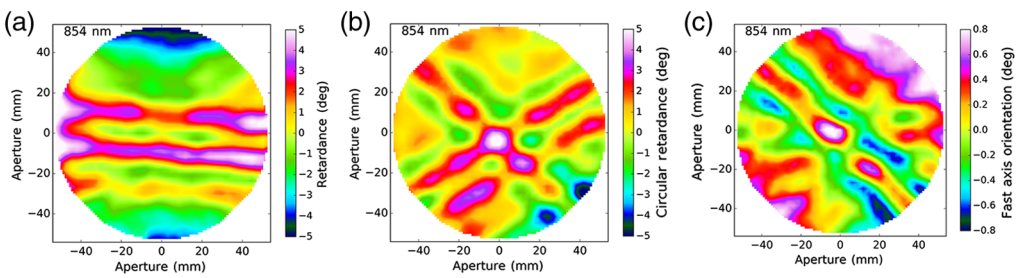

Fig. 8 Spatial variation of retardance across the ViSP PC three-layer retarder at 854-nm wavelength measured by MLO. (a) Spatial variation of ER magnitude, (b) the spatial variation of circular retardance, and (c) spatial variation of the fast axis of linear retardance. NLSP data agrees with MLO, similar to Fig. 7.

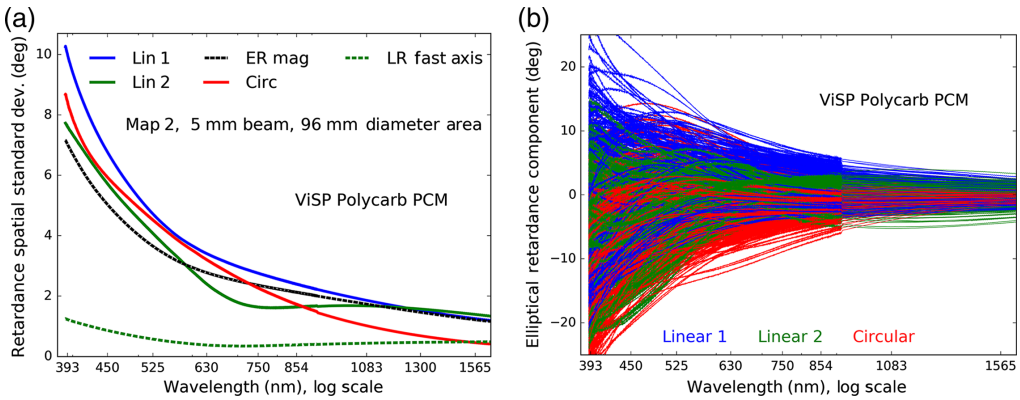

Fig. 9 (a) The elliptical retarder spatial variation statistics computed as the standard deviation across the aperture at each wavelength for each component. (b) The aperture variation of the three elliptical retarder components compared to aperture center. Note the large SNR change between visible (VIS and NIR) spectrographs in NLSP at 1020-nm wavelength with NIR data at much higher SNR.

the retardance variation has changed substantially with rotated ridges in retardance magnitude as well as fast axis.

Figure 9 shows spectra of the spatial variation of the ER fit parameters derived from all NLSP spectra. Both visible (VIS) and near-infrared (NIR) systems agree at the 1020 nm splice wavelength. Figure 9(a) shows the standard deviation of each retardance fit component at each wavelength across the 217 measurements of the spatial sampling pattern of the second map, covering a 96-mm aperture with 6-mm sample spacing. We computed the same statistics for the 60-mm aperture with a 3-mm step and see only mild differences in spatial properties. The typical spatial scale for aperture variation is only a few millimeters. There is a mild dependence on aperture size.

2.6 *ViSP Retardance Uniformity: Impact with Field Angle and Modulation Efficiency*

Though the PC modulator is several factors more spatially variable in retardance than the six-polished crystal retarders, modulation remains efficient over wide fields with decentered beams. Modulators do not need to be anywhere near as spatially uniform as calibrators when a field-dependent demodulation is performed. We perform the same analysis of a field-dependent modulation matrix for a discrete eight-state sequence as in HS18b[46] (Sec. 7).

In Fig. 10, we show ER magnitude for the beam footprints for an eight-state uniformly spaced (clocked) discrete modulation sequence. The ViSP modulator station is located after the spectrograph entrance slit in the diverging $F/32$ beam. The beam footprint in the first-light optical configuration covers roughly 80 mm of aperture with a mostly rectangular shape. The selected slit width and height set the illuminated region with an 8.1-mm-diameter footprint at each unique field angle (for each slit height position).

With these retardance spectra at each spatial location, we can build up the field variation of retardance components in each annulus. This shows how symmetric the first and second half-rotations will be for modulation as well as sets expectations for depolarization via aperture and temporal averaging. Figure 11 shows the peak-to-peak (P-P) retardance variation in an annulus swept by the 8.1-mm beam footprint as a function of decenter. The linear and elliptical magnitudes are shown as well as the linear fast axis and circular component. The 1-arc min slit height corresponds to a maximum decenter of ± 19.1 mm with the full 2-arc min slit at ± 38.3 mm.

We show the area-averaged retardance within each footprint at select field angles as the optic spins through a full revolution in Fig. 12. The blue curves show a 15 arc sec field angle (slit heights) covering a 0.25-arc min height field. The retardance variation with optic rotation steadily increases with slit height to the red curve at a 60 arc sec field angle covering a 2-arc min total field of view. The shorter 409-nm wavelength at left has a P-P variation over 14 deg,

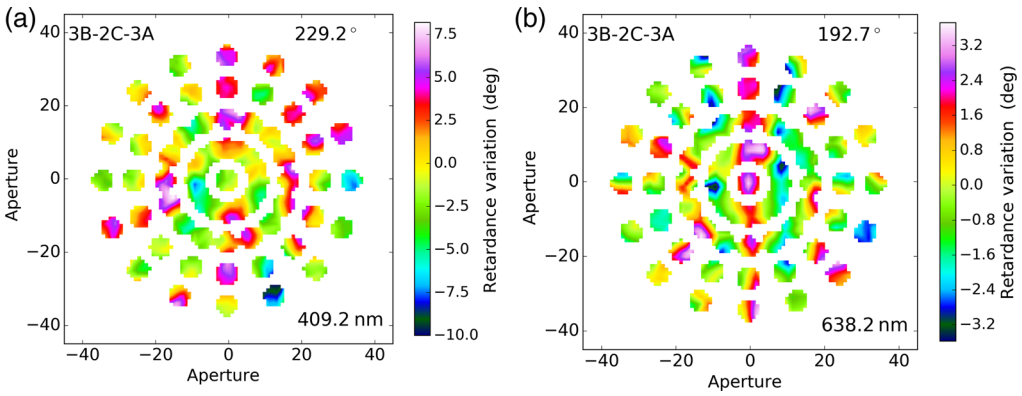

Fig. 10 Retardance extracted for each beam footprint on the ViSP PC retarder. Each individual field angle imaged through ViSP maps to an 8.1-mm diameter footprint on the optic. As the optic spins, the illuminated portion of the optic samples variable portions of the aperture. (a) 409.2-nm wavelength with a mean ER of 229.2 deg and (b) 638.2-nm wavelength with 193.2 deg mean ER. We show footprints for field angles of 0.5, 1.0, 1.5, and 2.0-arc min field diameters. We use angular steps of 22.5 deg starting at 0 deg during discrete modulation. A continuous modulation will sweep the beam through an arc between circles. We model this time-variable footprint later in this section.

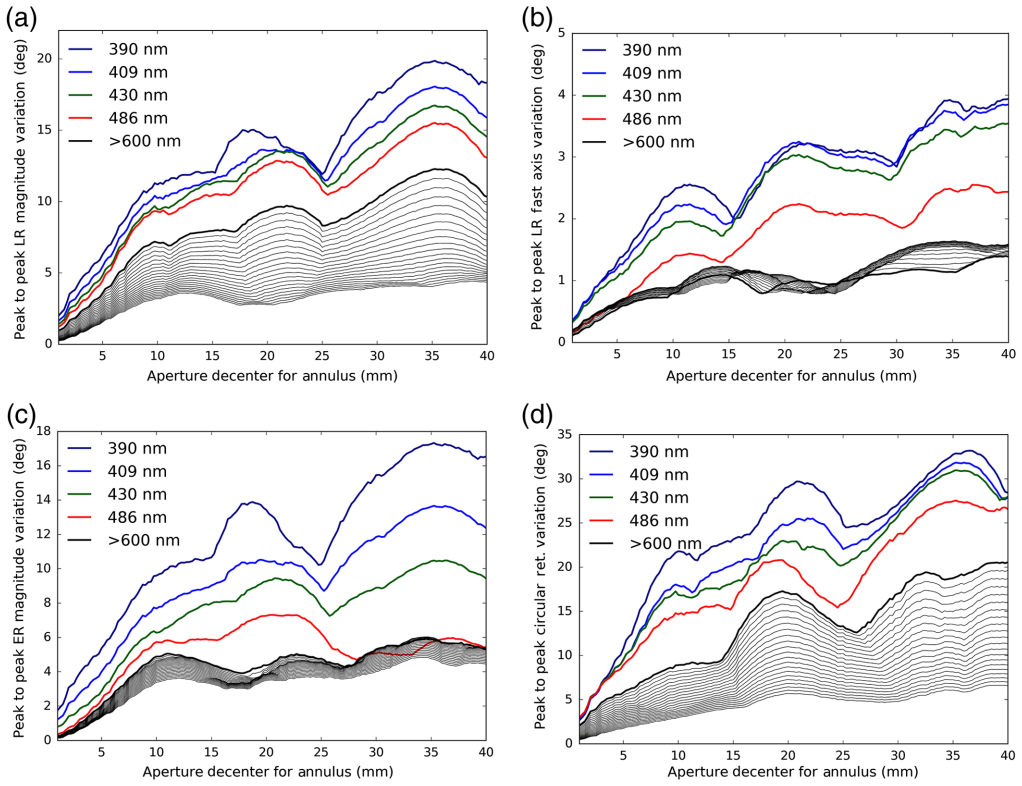

Fig. 11 P-P spatial variation of ER parameters in the annuli swept by the ViSP beam footprints during continuous modulation over a full 360-deg rotation at increasing field angle. We simulate the ViSP beam decenter increasing with field angle from 0 to 40 mm representing more than the full 2 arc min ViSP slit height. Different colors show the P-P variation at different wavelengths. Wavelengths shorter than 500 nm have 2 to 4 times as much retardance component variation than longer wavelengths. The graphs each have separate *Y* axis scales. (a) The magnitude of linear retardance at up to 20-deg variation, (b) the fast axis of linear retardance at up to 4-deg variation, (c) the magnitude of ER at up to 17-deg variation, and (d) circular retardance at up to 35-deg variation.

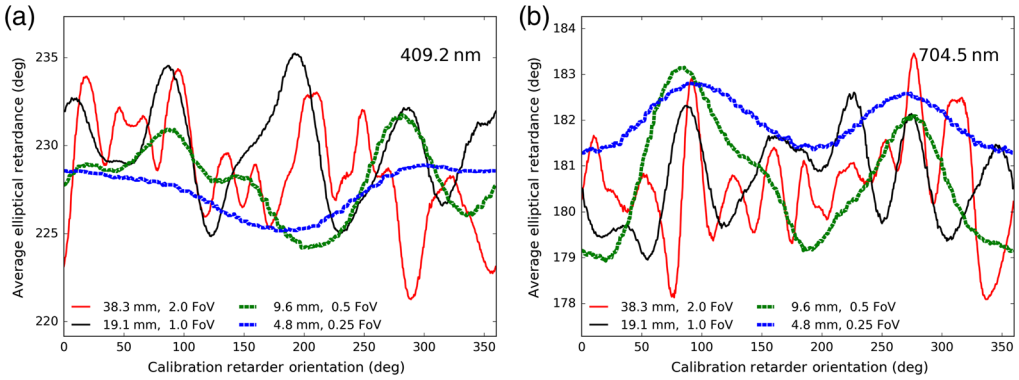

Fig. 12 Spatial variation of ER magnitude as the optic spins through 360 deg: (a) 409.2-nm wavelength and (b) 704.5-nm wavelength. Blue shows a 0.25 arc min field height at the 4.8-mm footprint decenter. Green shows a 0.5 arc min field height at the 9.6-mm decenter. Black shows a 1.0 arc min field height at the 19.1-mm footprint decenter. Red shows a 2.0 arc min field height with a 38.3-mm footprint decenter. Small field angles see substantially less difference between the first 180 deg and the second.

whereas the longer 704-nm wavelength at right shows a roughly 5-deg variation for the outer annulus traced at a 60-arc sec field angle.

We model the modulation efficiency with the standard least squares solution for minimum errors.[73] For continuous and discrete modulation, we use the ViSP beam footprints and the ER spatially averaged over time. For the continuous rotation case, we propagate flux through an ideal analyzer in 50 discrete steps for each 22.5-deg modulation state to approximate the nonuniform optic as it rotates in the beam for each modulation state. The flux in the discrete steps sampling at 0.5 deg are then averaged.

Figure 13 shows the modulation efficiency for the discreet modulation case in (a). The individual curves represent different beam decenters across the field of view (slit height position). Efficiencies only vary by several percent from the nominal design. Figure 13(b) shows the modulation matrix elements for all field angles at a worst-case example wavelength of 390 nm. The solid curves show the first half of the optic rotation, whereas the dashed lines show the second half. The dots represent the temporal average of the 22.5-deg motion during a continuously integrated modulation cycle as anticipated for ViSP. We take the 0.5-deg step sampled modulation elements and integrate during the 22.5-deg rotation modulation states. The depolarized efficiencies are computed as the time average of the flux through the modulator.

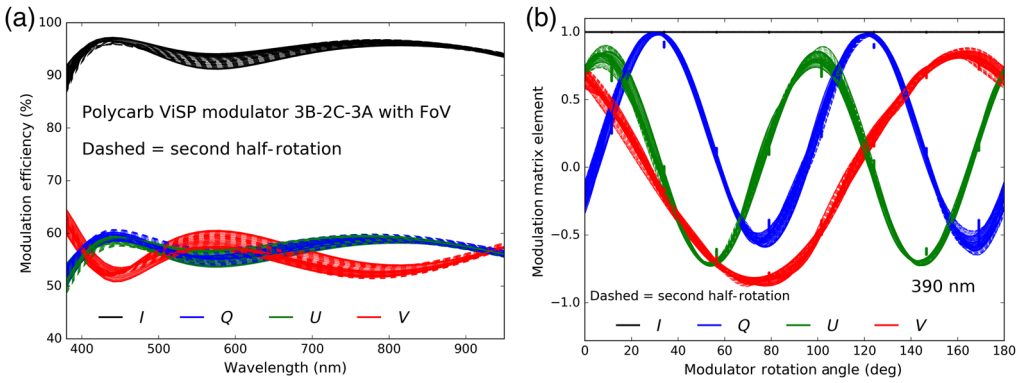

Fig. 13 (a) The modulation efficiency for decentered annuli at all field angles over all wavelengths is shown using discrete modulation. (b) An example of modulation matrix elements at 390-nm wavelength for all field angles during continuous rotation in 0.5-deg steps. The graphic overlays first-half and second-half rotation for the modeled optic. The dots show the exposure-averaged modulation matrix elements to simulate discreet modulation during a continuous rotation of the optic accounting for the loss of efficiency from the temporal average during each exposure.

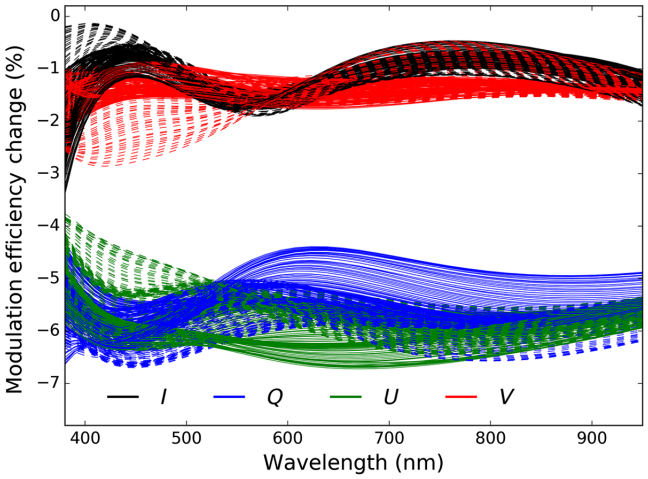

Fig. 14 The modulation efficiency change seen at different field angles from both spatial variation of retardance across the aperture and the depolarization caused by continuous rotation. This includes both the fast axis orientation change and the spatial nonuniformity with field angle. Solid lines show the first half-rotation, whereas dashed lines show the second half-rotation.

In Fig. 14, we show the modulation efficiency losses when continuously rotating the optic during an exposure compared to the discrete modulation case above. The losses include both the nominal fast axis of linear retardance rotation during an integration as well as the spatial variation caused by position-dependent beam footprints during rotation. The efficiency losses are still dominated by the fast axis rotation of 22.5 deg within an exposure. The 5% QU efficiency loss is fairly constant with wavelength compared to the field dependence of retardance parameters, which drops by a factor of 5× toward long wavelengths over this bandpass. The spatial variation predicted for this PC modulator only changes the efficiencies by a few percent. This compares to continuous rotation during an exposure, which drops the I and V efficiencies by 1% to 2% and the QU efficiencies by 5% to 7%.

3 Fringe Suppression in Calibration Retarders

The DKIST Gregorian Optical Station presently contains three calibration retarders used to calibrate the entire system of telescope mirrors and instruments.[48] These optics must function in the $F/13$ beam to high accuracy with high spatial uniformity over a 105-mm aperture under a 300-W load, under UV irradiation, while operating at mountain environmental temperatures. The nominal suite of calibration retarders detailed in HS18b[46] was all SARs made of three compound retarders in A–B–A style, each with six crystals total. We add to this list a newly designed and fabricated optically contacted compound retarder that is not achromatic and is net zero order after two crystals are used in subtraction. We pursued optical contact as a bonding technique to remove any refractive index mismatch issues with oils or bonding agents in addition to the long lifetime requirements in the presence of 300 W of optical power with substantial UV flux. We added very tight clocking requirements (0.3 deg), beam deflection, and spatial uniformity requirements to this optic. We create new focal ratio dependent fringe predictions to compare the super achromats to the optical contact retarder. We summarize the current DKIST calibration retarders here from the perspective of fringe magnitudes, calibration efficiency, and calibration accuracy limited by thermal instabilities.

In Table 4, we outline some of the details of each crystal retarder design. In the first column, we list the name of each optic. The name corresponded with the wavelength range covered by the design, though both the instruments and the calibration technique, have changed wavelength ranges in subsequent years. We note that the nominal DKIST requirement for these optics some years ago was for each calibrator to be a 90 deg $\pm$30 deg magnitude linear retarder also with an achromatic fast axis orientation within some wavelength bandpass. However, we can use these optics over a much wider wavelength range for calibration as we detail below. We also note that

Table 4 DKIST calibration retarder crystal material and retarder designs.

Name	Crys. (Mat).	Thk (mm)	Bias (waves)	Design magnitude (net waves retardance)	Design fast axis (deg)	Nominal bandpass (nm)
Opt. contact	SiO_2	4.2	60 ± 1	0.23	0	420 to 1100
ViSP SAR	SiO_2	2.1	30 ± 1	0.328–0.476–0.328	0–70.25–0	380 to 1100
Cryo SAR	MgF_2	2.2	40 ± 1	2.230–3.346–2.230	0–107.75–0	2500 to 5000
DL SAR	SiO_2	2.1	30 ± 1	0.683–1.000–0.683	0–65.00–0	900 to 2500

a wavelength dependent fast axis as well as circular retardance are already present in these optics and fit by the DKIST calibration software. A chromatic elliptical calibrator would be sufficient to calibrate, just as it is sufficient to modulate.

In the second, third, and fourth columns, we show the properties of the six individual crystals that make up the SAR. We note there is a detailed description of the metrology of these optics published in HS18b.[46] The individual crystal material and thickness are shown along with the net retardance of the individual crystals at the 633-nm wavelength, typically many 10s of waves retardance. The bias retardance for the bias plate is listed in waves with the subtraction plate polished to be within zero order of the bias plate. In the fifth column, we show the net difference polished into the pairs of crystals following the super-achromatic A–B–A Pancharatnam style. As an example, we showed in HS18b,[46] the Cryo-NIRSP SAR first crystal had 42.909 waves net retardance, whereas the second crystal had 40.683 waves net retardance. When assembled as a compound retarder with fast axes crossed (oriented 90 deg to each other) the net retardance of this "A" crystal pair was 2.2319, close to the 2.23 waves design magnitude for this particular pair. The sixth column shows the nominal fast axis orientation for each pair of crystals in A–B–A style.

The last column of Table 4 shows the nominal wavelength range where the optic was an achromatic linear calibrator, though calibration at other wavelengths is anticipated. The ViSP SAR was nominally designed for the 380- to 1100-nm bandpass and is made of ~2.1-mm-thick quartz crystals at 30 waves retardance each. The Cryo-NIRSP SAR meets the nominal DKIST retardance requirements in the 2500-to 5000-nm bandpass, but we also show here that it is useful for calibration at many wavelength ranges throughout the visible and NIR wavelength region. This optic is of particular interest, as the lack of infrared absorption means these optics heat far less than quartz and could possibly have reduced fringes and associated fringe thermal drifts per HS18a.[43]

The DL-NIRSP SAR was nominally designed for the 900- to 2500-nm bandpass also with 2.1-mm-thick quartz crystals. A descope of the infrared camera along with some instrument reoptimization shortened the wavelength range for first light to 500 to 1800 nm. The longest wavelength filter is at 1565 nm for the DKIST first-light configuration of DL-NIRSP. With this development, we show that we can use the ViSP SAR to calibrate the 380- to 1800-nm bandpass successfully though with mildly reduced efficiency at extreme wavelengths. We thus did not deploy the DL SAR optic and replaced it with the new optical contacted compound zero-order quartz retarder.

The optical contact retarder was built to show that a successful optical bond of two crystals at 120-mm diameter removes concerns of heating and UV degradation of oils, mitigates fringes with thicker crystals, and minimizes the internal reflections from interfaces between crystals. A further manufacturing challenge was maintaining a defect-free clear aperture at 105-mm diameter while also minimizing the spectral clocking oscillations shown above in Fig. 6, which get linearly worse with crystal thickness. MLO used two quartz crystals to create a single compound zero-order retarder having roughly a quarter-wave magnitude at the 633-nm wavelength. The DKIST project had readily available crystal blanks near 8-mm thickness purchased for our prior work. We chose to polish them to a substantially thicker net retardance with MLO attempting to achieve retardance spatial uniformity. As the spatial fringe behaves as r^{-2} in

the difference between marginal ray path to chief ray path, doubling the crystal thickness would reduce fringe magnitudes by roughly 4×. The internal optical contact interface mismatches extraordinary and ordinary beams and only reflects a very small amount of power. We anticipate further fringe suppression by combining these two crystals and again doubling the marginal ray path. We anticipate still further performance increase at shorter wavelengths as the fringe period gets correspondingly shorter, is under-resolved, and is well separated from typical solar spectral signals. After several attempts at polishing to achieve tight uniformity specifications, we stopped polishing at a 4.2-mm thickness. We outline the details of an unsuccessful attempt to use deterministic fluid jet polishing to achieve substantially lower spatial retardance variation in Appendix C. One crystal had been polished to a transmitted wavefront of $\lambda/52$ P-P corresponding to a 7.7-nm physical thickness variation. The retardance spatial uniformity was 40 times larger than predicted by the thickness nonuniformity alone. These points to internal material issues not easily measured or mitigated with typical wave front error and polishing techniques.

3.1 *Calibration Efficiency and Chromatic Retarders*

When choosing a calibration retarder, there are often specifications for keeping the retarder linear (not elliptical) and for chromatic variation of the linear retardance fast axis. Typically, a retarder is designed to create pure Stokes inputs to an optical system so a calibration process can be followed. We describe here some calibration use cases for the three DKIST retarders without creating any pure inputs and also while accounting for calibration retarder ellipticity. The time required to calibrate a system depends significantly on the duty cycle of the measurement.

When crystal optics are used in rotating stages along with translation stages, the time lost to moving optics can be significant. For modern solar observatories running simultaneous calibration, the software lag times when coordinating multiple cameras inside multiple instruments can also be substantial. For DKIST, we can run at least nine polarimetric cameras simultaneously spread between at least three separate instruments (e.g., ViSP, VTF, and DL-NIRSP). The instrument performance calculators suggest integration times of seconds to achieve signal-to-noise ratios (SNRs) of hundreds.

The software lags are as yet unknown, but are anticipated to be of the same order or worse. This gives a possible duty cycle somewhere <70% and as low as 20%. Temporal instabilities driven by thermal and atmospheric changes imply calibration time should be minimized. Duty cycle is improved substantially using a calibration sequence with a higher SNR per photometric measurement and with fewer states.

As a first step, we must choose a specific sequence of calibration optic orientations to generate a diverse set of Stokes vectors. For operational efficiency, DKIST must calibrate as many instruments as possible in a simultaneous configuration. There is a similar analogy between modulation efficiency[73] and calibration efficiency. In Ref. 47, some simple optimization procedures are summarized on the polarization calibration of the Swedish Solar Telescope.[47] In Sec. 2.5.2 of Ref. 47, the orthogonality of the Stokes vectors created by the calibration unit is assessed in matrix form with one row per input state

$$\mathbf{M}_{\text{Stokes}} = \begin{pmatrix} I_1 & Q_1 & U_1 & V_1 \\ I_2 & Q_2 & U_2 & V_2 \\ \cdots & \cdots & \cdots & \cdots \\ I_n & Q_n & U_n & V_n \end{pmatrix}. \tag{2}$$

Equation (2) shows the Stokes vector matrix ($\mathbf{M}_{\text{Stokes}}$) used to derive the condition number and the relative calibration efficiency of the exposure sequence. The pseudoinverse of $\mathbf{M}_{\text{Stokes}}$ is created as $E_{i,j} = (\mathbf{M}_{\text{Stokes}}^{\text{T}}\mathbf{M}_{\text{Stokes}})^{-1}\mathbf{M}_{\text{Stokes}}^{\text{T}}$. The efficiencies are computed from the pseudoinverse as the usual sum of squared elements $e = (n\sum_1^n E^2)^{-0.5}$, where n is the number of input states. This pseudoinverse E can also be assessed by its condition number. This is the same approach as for finding optimum demodulation matrices[29,73,74] Both approaches assume uniform noise in each exposure, which is not true for calibration. But we can still use this definition and the condition number as a way of assessing input state diversity. A matrix with a low condition

Table 5 Sequence.

LP	Ret
Out	Out
0	Out
60	Out
120	Out
0	0
0	60
0	120
45	30
45	90
45	150
45	**0**
Out	Out

number is said to be well conditioned, while a problem with a high condition number is said to be ill conditioned and ill-conditioned fits have very different noise properties in the resulting fit values. For DKIST calibration, we want to ensure the SNRs of the calibrated Stokes vectors are equal within a factor of a few, and roughly proportional to the SNR of the instrument's photometric measurements, hence needing a condition number below a few. We make a simple example for the three DKIST calibration retarders here by optimizing an existing sequence we use in our lab spectropolarimeter. We consider this sequence noting that we can use 12 nominal orientations that would each create four individual $\pm QUV$ inputs when using a quarter-wave linear retarder as is common in traditional calibration.

We show in Table 5 the orientations of the calibration linear polarizer (LP) and calibration retarder (Ret) in the two columns. We note that in practice, no optic is perfectly achromatic or aligned and we do not need to assume that perfectly pure individual Stokes parameters are created for any calibration state. We search the calibration efficiency space using the ViSP SAR optic properties to find balanced calibration efficiency across DKIST wavelengths 380 to 1600 nm, as published in HS18b.[46] For this example, we consider adding one additional exposure with two free variables where the retarder and polarizer can each be used at any orientation between 0 deg and 180 deg. The last bold row shows the optimized sequence in Table 5. We also list for completeness the calibration measurements with both the polarizer and retarder out of the beam. This is commonly called a clear measurement, but it does provide modulated flux from diattenuation of the DKIST primary and secondary mirrors along with photometric information on the transmission functions of the calibration optics. With the calibration sequence in Table 5, we can then derive the calibration efficiency for each DKIST calibration optic. We show the $IQUV$ efficiency for the two quartz retarders in Fig. 15 with each curve representing a change in the nominal optic starting orientation for the sequence in Table 5. Each graphic has a different Y axis scale. The ViSP SAR at left always has efficiencies above 0.2 in the full AO-assisted instrument suite bandpass 380 to 1600 nm. The optical contact retarder is only above 0.2 efficiency in the range 450 to 1100 nm, but calibration over a wider bandpass should be possible with sufficient redundancy and input optimization. The Cryo-NIRSP (CN) SAR shown in Fig. 16(b) will certainly fail to calibrate the system at a few visible wavelengths, but could be quite useful at many discrete wavelengths in addition to its nominal high-efficiency range of 2000 to 5000 nm. We showed in Fig. 35 of HS18b[46] that this retarder can calibrate the first light VTF wavelengths as well as many ViSP configurations.

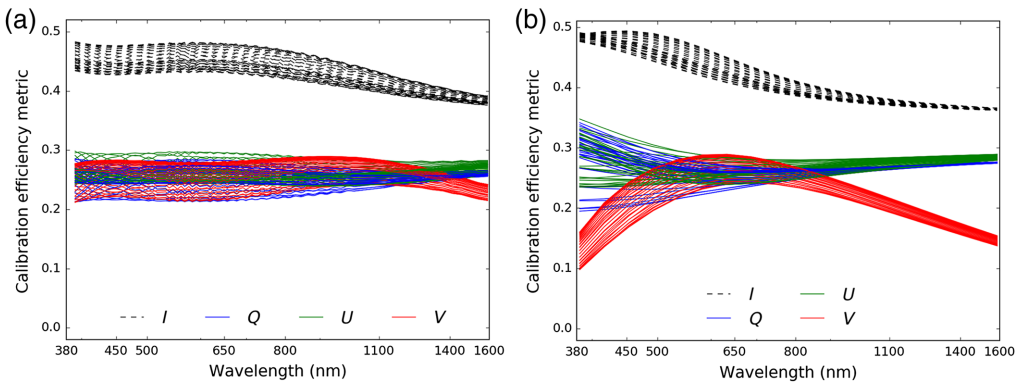

Fig. 15 The efficiency of the two quartz DKIST calibration retarders used with a 10-state sequence and a variable starting optic orientation: (a) the ViSP SAR and (b) the new optical contact retarder.

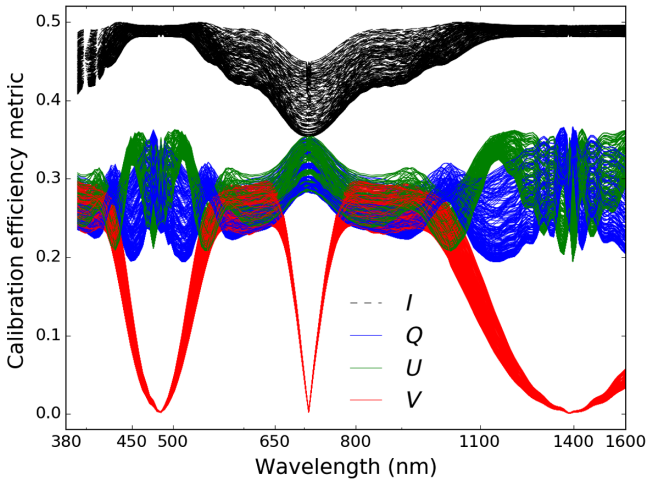

Fig. 16 The efficiency of the Cryo-NIRSP MgF_2 calibration retarder used with a 10-state sequence and a variable starting optic orientation. This optic is designed for optimal performance in the range of 2000 to 5000 nm, but can function very well at shorter wavelengths.

3.2 *Optically Contacted Quartz Compound Retarder for* F*/13 Calibration*

We compile the metrology performed at MLO for use in the fringe and thermal models. Both crystals are roughly 4.2 mm thick. The design is for a net 0.23 waves retardance at a 630-nm wavelength in compound zero-order configuration. This ensures we have a net retardance above 28 deg and below 155 deg for calibration of the nominal AO-assisted DKIST first light instrument suite. One crystal (the subtraction plate) is polished 16-μm thicker than the other (bias plate) to achieve this net retardance in subtraction with the fast axes for each crystal optically contacted at a 90-deg rotational orientation. The optically contacted quartz calibration retarder configuration is shown in Table 6. The two crystals were measured with the Heidenhain thickness gauge, but were not in optical contact with the reference plate. Typical values for the air gap on large optics are roughly 10 μm by differencing contacted from noncontacted measurements. The MLO measurements for each of the two crystals gave thicknesses of 4.234 and 4.247 mm, respectively. These thicknesses are used in the fringe modeling. We also have Varian Cary spectrophotometer scans with the crystals between crossed polarizers on each individual plate as detailed in Appendix C. The thickness difference should be about 15.97 μm between crystals to achieve the net retardance measured between plates oriented in subtraction. A 2-μm difference between air gap thickness in the Heidenhain gauge set up stacked with measurement uncertainty accounts for this discrepancy with the net retardance being a highly accurate gauge of differential crystal thickness.

Table 6 Optical contact SiO_2.

Layer	T (μm)	Note
Coating	0.7	WBBARcq
SiO_2 1	4234.0	0 deg
SiO_2 2	4250.0	90.3 deg
Coating	0.7	WBBARcq

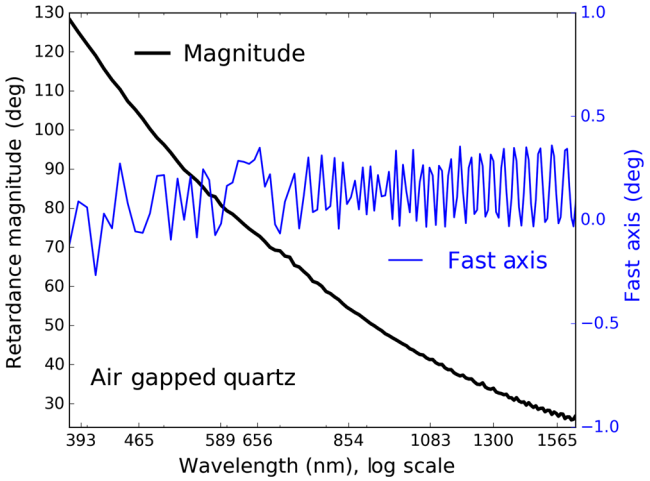

Fig. 17 The spectral variation in retardance properties for an air-gapped set up with the individual 4.2-mm-thick quartz crystals with the MLO system. The black curve and left-hand y axis show the retardance magnitude. The blue curve and righthand blue y axis show linear retardance fast axis orientation. The system clearly resolves spectral oscillations of fast axis variation at amplitudes around 0.4 deg P-P.

Figure 17 shows the spectral measurement of retardance for an air-gapped configuration of the two quartz crystals. The black curve using the left-hand Y axis shows the retardance magnitude near 130 deg at the 380-nm wavelength falling to below 30 deg at the 1565-nm wavelength. The blue curve shows the fast axis of linear retardance with the crystal clocking misalignment spectral oscillations resolved at longer wavelengths.

For purposes of our modeling, we use thicknesses of 4234 and 4250 μm for each crystal for a total of 8484 μm. The coating we denote WBBARcq for the 380- to 1800-nm wavelength design range. It consists of a <20-nm-thick strippable layer followed by 14 oscillating layers of SiO_2 and Ta_2O_5 ending with a thicker MgF_2 outer layer for 0.74 μm total coating thickness and 16 total layers. After successful AR coating and optical contacting, the spatial maps were repeated, but now with an ER measuring technique. As outlined in Appendix B.4, we convert the MLO rotation matrix decomposition formalism to our preferred axis-angle formalism.

We show the ER magnitude and circular retardance component in Fig. 18. The magnitude graphic at left very closely resembles the air-gapped set up and simulations shown in Appendix C. The measured circular retardance spatial variation at ± 0.1 deg magnitude is on top of a mean of 0.02 deg, which does show some significant spatial variation corresponding to polishing nonuniformities. The fast axis variation was noise limited to roughly ± 0.02 deg P-P. We note that we performed spatial mapping of Mueller matrix spectra with NLSP as outlined in Appendix C. The spatial pattern of retardance magnitude is effectively constant following Fig. 18(a) but with a magnitude that decreases as λ^{-1}. This is expected for a simple compound retarder with spatial thickness variations.

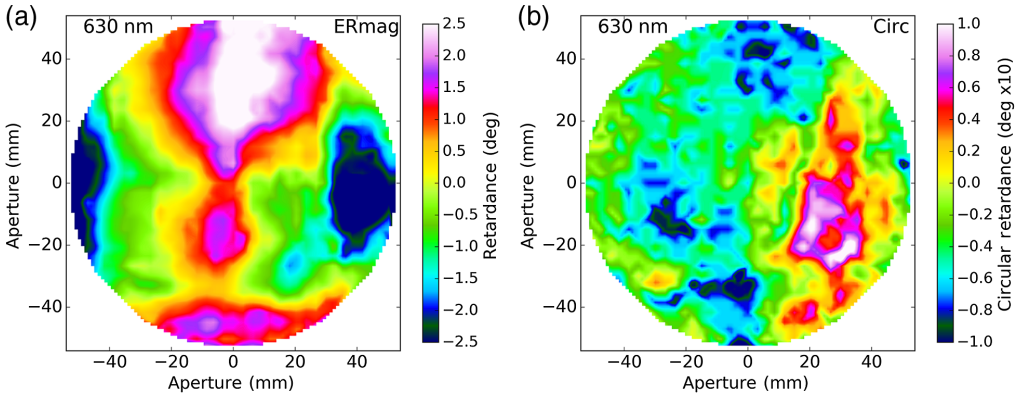

Fig. 18 Spatial variation of retardance properties across the optically contacted quartz compound retarder at 630-nm wavelength measured by MLO. (a) Spatial variation of ER magnitude and (b) the spatial variation of circular retardance on a 10× magnified color scale. Spatial sampling covered a 108-mm aperture in a rectangular pattern with 3-mm spacing. Note that our NLSP spatial mapping agrees with these MLO results though we use very different measurement techniques. Our spatial maps at all wavelengths look similar to these MLO maps at one wavelength.

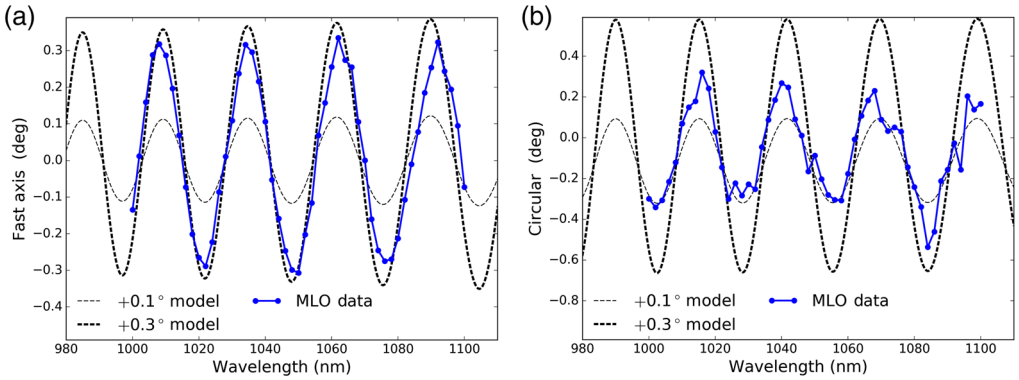

Fig. 19 (a) The fast axis spectral variation for the final optically contacted part and (b) the circular retardance. The black curves represent models with a clocking error of magnitudes 0.1 deg for thin dashed lines and 0.3 deg for the thicker dashed lines. The MLO spectral system clearly resolves spectral oscillations in between the two models.

After optical contact, we verified the ER spectra with a narrow spectral region and resolving power of 1 nm to verify the successful reduction of clocking oscillations with the tight alignment tolerances. We show in Fig. 19 the fast axis of linear retardance and the circular retardance component in a spectral bandpass around 1000 nm wavelength. Each point represents a separate measurement in the MLO set up with the monochromator set to a 2-nm spectral step size. We resolve the clocking oscillations consistent with a crystal misalignment of roughly 0.3 deg. The black dashed lines show our crystal model with each crystal 4.2-mm thick. The blue line and points show the MLO data. This 0.3-deg alignment reduces spectral errors by a factor of 3× over the typical 1-deg specification.

3.2.1 *Quartz optical contact: modeling clocking errors and thermal performance*

The thermally induced drifts of the clocking oscillations represent the major temporal stability limit of these larger compound retarders. We combine manufacturing errors in rotational alignment of the two crystals at specification limits of ±1 deg relative clocking with a thermal perturbation analysis. We model thermal gradients with depth by approximating the top crystal as at a different temperature than the bottom plate following our thermal model predictions.

Table 7 SiO_2 material properties.

Prop	*E* axis	*O* axis
CTE	-5.5×10^{-6} C^{-1}	-6.5×10^{-6} C^{-1}
TOC	7.1×10^{-6} C^{-1}	13.6×10^{-6} C^{-1}
Conduct. (W/mC)	10.7	6.2
Mod El (GPa)	97.2	76.5
Pois R	0.56	0.22

In Table 7, we show the materials properties assumed for the crystal quartz thermal analysis for the extraordinary axis (E) and the ordinary axis (O). The CTE is shown as the first row showing the fractional change in physical thickness with temperature (dL/dT). The TOC is shown as the second row representing the change of refractive index with temperature (dn/dT). For mechanical and thermal modeling, we also included the directionally dependent conductivity and modulus of elasticity shown in the third and fourth rows. The fifth row shows Poisson's ratio as the ratio between transverse strain and axial strain. The specific heat of crystal quartz was assumed to be 710 J/kgC with a density of 2649 kg/m^3.

We use temperature offsets of ± 0.05°C and ± 0.025°C for each crystal to estimate temperature gradients with depth in the optic. We also model environmental temperature changes by letting the bulk temperature of the crystals change by ± 20°C from an ambient of 20°C. Figure 20 compares the thermal perturbations for perfect clocking alignment in (a) with the magnitude of the spectral clocking oscillations for a 1-deg rotational misalignment in (b). The clocking oscillations are roughly 50× larger in magnitude than the perfectly aligned but thermally perturbed case for this typical 1-deg clocking alignment. The thermal perturbations of the clocking oscillations are at the same 50× larger magnitude. This oscillation is the dominant temporal stability limit. We show in Appendix C. 3 some detailed mechanical and thermal modeling along with 300-W illumination. We also show thermal testing of a six-quartz crystal test retarder in Appendix A.1.

Figure 21 shows the thermal drift behavior of ER parameters when a −20°C bulk temperature change is applied to the compound zero-order retarder with no depth gradient. Figure 21(a) shows the spectral differences when the optic changes temperature by 20°C representing

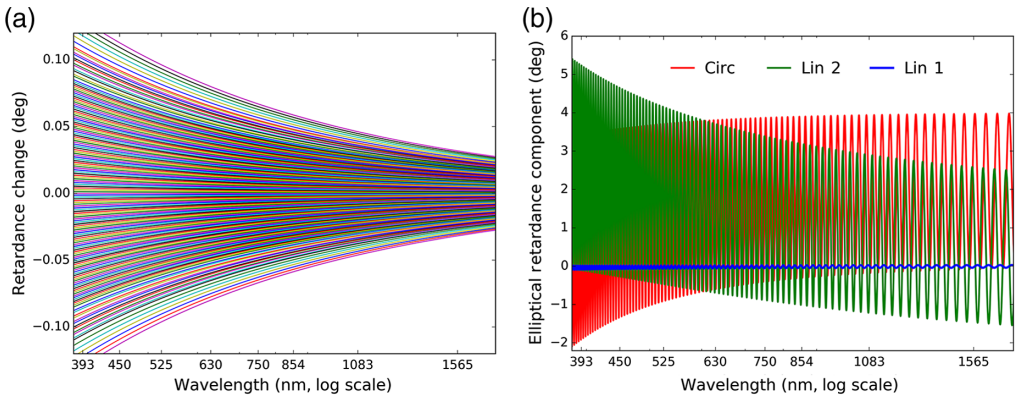

Fig. 20 (a) Thermal perturbation of both crystals with perfect rotational alignment for ± 20°C of ambient temperature change in steps of 2°C and ± 0.05°C of differential crystal temperatures for 20 ambient temperature models at two differential temperature settings. Each color shows a different model. Peak retardance changes correspond to maximum ambient change and differential temperature. (b) The three ER components when the crystals are bonded with a 1-deg clocking offset. We use a 20°C ambient temperature with no difference between crystal temperatures. We see a 50× larger perturbation in (b) than the perfect rotational alignment in (a).

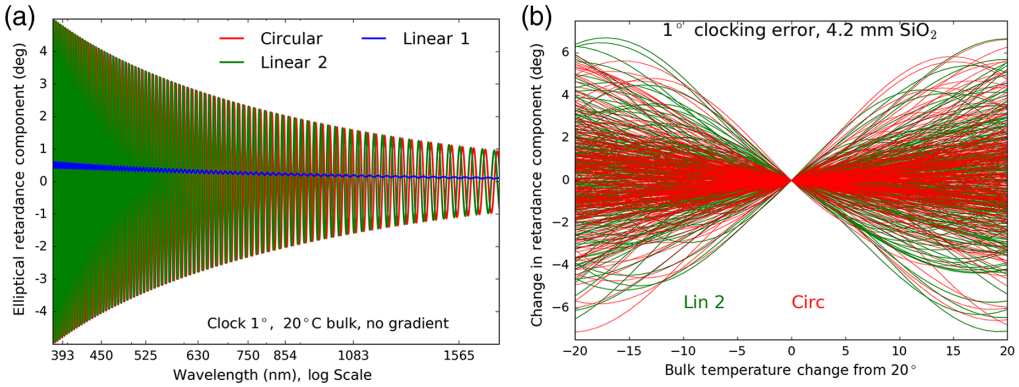

Fig. 21 Optical contacted quartz compound retarder elliptical component change with a −20°C bulk temperature change. (a) ER spectral changes for a 1-deg clocking offset on crystal 2. (b) Thermal change of the ER parameters with temperature rise with this same 1-deg clocking offset for 70 wavelengths uniformly sampled over the 380- to 1650-nm bandpass. The many overlapping curves show an envelope that can be maximal when the particular wavelength used by a DKIST instrument is at a clocking oscillation peak. Other wavelengths can show minimal change with temperature when the particular wavelength is near a clocking oscillation null. Thermal changes in the second linear retardance component are shown in green, whereas the circular retardance component changes are shown in red.

a change from a cold morning to a warm afternoon for the summit telescope environment. The clocking oscillations dominate the spectra.

Figure 21(b) shows thermal change of the ER parameters with temperature rise for this same typical 1-deg clocking offset specification. We show 70 wavelengths uniformly sampled over the 380- to 1650-nm bandpass with each as a separate curve. As the temperature rises, thermal changes cause a strongly variable retardance change at each wavelength depending on the clocking oscillation magnitude. We show the second linear retardance component in green, whereas the circular retardance component changes are shown in red. The first linear component shown as blue in Fig. 21(a) does not change substantially in this model. This analysis shows that the nominal thermal compensation of a compound retarder could have been below 0.1 deg for a theoretically perfect optic, but real manufacturing tolerances produce oscillations at magnitudes 50 times larger than this with temperature changes of only a few degrees causing spectral drifts at magnitudes above 1 deg.

3.3 *SiO_2 Super-Achromat for Calibration (ViSP SAR)*

The DKIST super achromatic calibration retarder that covers visible and NIR wavelengths was named the ViSP SAR even though it can function for simultaneous calibration of ViSP, VTF, and DL-NIRSP instruments. In Table 8, we outline the individual layers in the Berreman fringe model for this retarder. The first column denotes the layer and material. We note that AR is the AR coating that denotes a single isotropic MgF_2 layer at a 97-nm physical thickness corresponding to a quarter wave at a 525-nm central wavelength. The quartz crystals are combined into compound zero-order retarders in pairs at orientations of 0 deg–90 deg or 70 deg–160 deg. The refractive index 1.3 oil is nominally assigned a 10-μm physical thickness for each layer. As above in Fig. 6, the crystal clocking errors represent the major temporal instability in this calibration retarder as the spectral oscillations drift with temperature throughout the day.

3.4 *Quartz Retarder Fringes Mitigated At* F*/13: ViSP SAR versus Optical Contact*

In Fig. 22, we compare fringes in the two crystal quartz-based calibration retarders. Solid lines show a collimated beam, whereas dashed lines show the impact of the $F/13$ spatial fringe scale factor. Figure 22(a) shows the six-crystal ViSP SAR with fringes from 2.1- and 12.8-mm

Table 8 ViSP SAR.

Lyr	T (μm)	θ
AR	0.1	—
Quartz1	2122.1	0.0 deg
AR	0.1	—
Oil	10.0	—
AR	0.1	—
Quartz2	2099.1	90.0 deg
AR	0.1	—
Oil	10.0	—
AR	0.1	—
Quartz3	2132.4	70.3 deg
AR	0.1	—
Oil	10.0	—
AR	0.1	—
Quartz4	2099.1	160.3 deg
AR	0.1	—
Oil	10.0	—
AR	0.1	—
Quartz5	2122.1	0 deg
AR	0.1	—
Oil	10.0	—
AR	0.1	—
Quartz6	2099.1	90 deg
AR	0.1	—

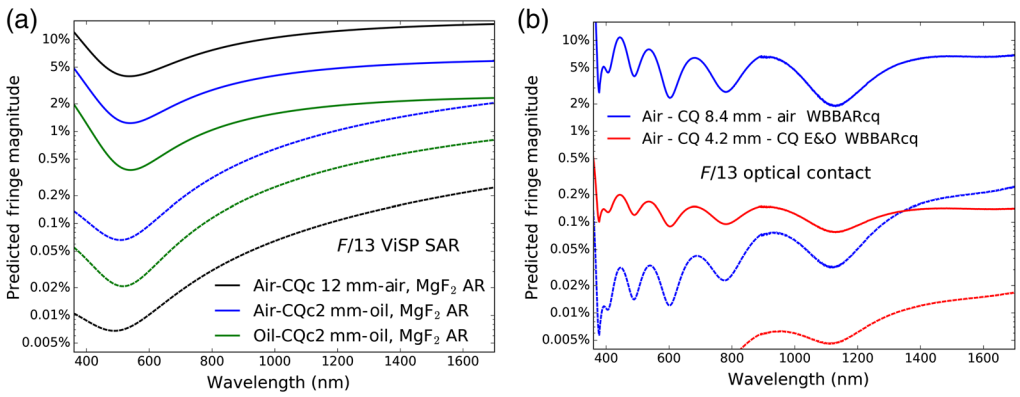

Fig. 22 Fringes for each optical interface. (a) The ViSP SAR and (b) the optical contact retarder. Fringe magnitudes in both optics are shown as solid lines in a collimated beam. Dashed lines include marginal ray path r^{-2} scaling in the $F/13$ beam. In (a), the ViSP SAR has three main interfaces: from air through coated crystals to air, from air through coated crystal to oil, and from oil through coated crystal to oil. (b) The air through coated crystal to air fringe for the optical contact retarder. The dashed line shows the internal fringe created from the index mismatch between ordinary and extraordinary beams.

Table 9 SiO_2 fringe magnitude collimated versus $F/13$.

Optical interfaces	λ	Col	$F/13$	Fact.
Enter–optic–exit	nm	%	%	
Air–13-mm SiO_2–air	396	8.49	0.01	954
Air–13-mm SiO_2–air	854	8.55	0.04	219
Air–13-mm SiO_2–air	1565	14.36	0.21	70
Air–2-mm SiO_2–oil	396	3.27	0.11	30
Air–2-mm SiO_2–oil	854	3.20	0.39	8.1
Air–2-mm SiO_2–oil	1565	5.69	1.77	3.2
Oil–2-mm SiO_2–oil	396	1.26	0.04	30
Oil–2-mm SiO_2–oil	854	1.20	0.15	8.1
Oil–2-mm SiO_2–oil	1565	2.25	0.70	3.2
Air–8-mm SiO_2–air	396	4.93	0.01	426
Air–8-mm SiO_2–air	854	5.31	0.05	100
Air–8-mm SiO_2–air	1565	6.65	0.20	33
Air–4-mm SiO_2–air	396	0.14	0.001	111
Air–4-mm SiO_2–air	854	0.13	0.005	27
Air–4-mm SiO_2–air	1565	0.14	0.015	9.6

thicknesses with the inner 2.1-mm crystals interfacing with both air and oil. Figure 22(b) shows the optically contacted quartz retarder. Blue shows the air interfaces, whereas red shows the internal extraordinary to ordinary interface mismatch interfering with the opposite air interface. Note that the dashed red curve is below 4×10^{-5} for short wavelengths and is off scale.

In Table 9, we compile some values to correlate with Fig. 22 for wavelengths of 396, 854, and 1565 nm. The first column shows the interfaces between air or oil and the optical elements in the six SiO_2 crystal modulator with coated surfaces. As an approximation for this table, we ignore the simultaneous solution of all coherent reflections following the Berreman calculus and simply approximate each layer as if it was alone and free standing. The second column shows the wavelength for each row. The third column shows the fringe magnitude for the collimated beam (Col) for comparison with solid lines in Fig. 22(a). The fourth column shows the peak fringe magnitude predicted with the r^{-2} envelope scaling to $F/13$. The fifth column shows the fringe reduction factor for that particular wavelength and the $F/$number for the particular optic producing individual fringes. We note that the top section of Table 9 is for the ViSP SAR, whereas the bottom section is for the optical contact retarder. We also list for completeness the small reflection caused by the mismatch between ordinary and extraordinary refractive indices for the optical contact interface.

The maximum fringe in the $F/13$ beam for the ViSP SAR is anticipated to occur from the air-to-oil interfaced first and last crystals. This corresponds to the dashed blue curve in Fig. 22(a). The spatial fringe average reduces spectral fringes from the 2.1-mm crystals by a factor of 30× at the 396-nm wavelength, but only by 3.2× at the 1565-nm wavelength. The wavelength dependence of the coatings and also mismatch with the oil gives a fringe magnitude prediction of 0.11% at a 396-nm wavelength up to 1.77% at a 1565-nm wavelength after accounting for the r^{-2} reduction factor. These fringe magnitudes are an order of magnitude larger than the optical contact retarder over the bandpass.

The refractive index mismatch is modeled to be 0.265 dropping to 0.24, which gives rise to internal reflections of roughly 0.8%. Had a suitable $n = 1.5$ oil been identified with an index mismatch below 0.05, this internal reflection could have been reduced by factors of at least 30×, reducing the internal fringes by factors of 5 or more. We note that the original choice of oil was driven in part by specifications on the lack of infrared spectral absorption bands and UV damage tolerance, as well as interfaces with cover windows of CaF_2 and fused silica that have since been removed from the six-crystal retarders.[43,65] A preliminary search done by DKIST team 2010 did not yield a suitable $n = 1.5$ oil. The fringes in this achromat would then be near levels achieved by the optical contact retarder. We also note that this upgrade included testing of many layer broadband AR coatings on very high aspect ratio crystal quartz retarders. Significant issues with depth dependence of temperature, wedge angle, and environmental response also complicated the initial trade studies. Given the expense of each polished and measured crystal, the construction project did not pursue these development efforts for the original set of six-crystal super achromats.

3.5 *MgF_2 Super-Achromatic Retarder for F/13 Calibration (Cryo-NIRSP SAR)*

The MgF_2 retarder typically denoted as the Cryo-NIRSP SAR has been extensively described in HS18b.[43] This optic can easily be used for calibration at visible wavelengths in the ranges 380 to 450 nm, 520 to 690 nm, and 730 to 1100 nm along with the nominal design bandpass of 2500 to 5000 nm. We show the Berreman fringe model for this optic in Table 10. There are six uncoated MgF_2 crystals with the $n \sim 1.3$ oil nominally at 100-μm physical thickness. The super achromat design consists of three compound retarders in A–B–A orientations. The first and last A compound retarders are nominally aligned. As with the ViSP SAR, the oil-to-crystal refractive index mismatch causes the air-to-oil facing crystals to create the largest fringes. The mismatch is much better between the $n = 1.3$ oil and the $n = 1.38$ MgF_2 crystals giving a 0.12% reflection at the internal interface. This combines with the 2.7% air-to-crystal interface to create a 2.3% magnitude fringe. We show the fringe magnitude behavior for the Cryo-NIRSP SAR comparing $F/13$ and collimated in Fig. 23. We use the same X and Y scales as in Fig. 22. The solid line near 11% magnitude represents the collimated beam fringe between the two air interfaces on the exterior of an uncoated MgF_2 crystal. The solid green line near 2.7% magnitude is the fringe caused by a crystal with oil on one interface and air on the other. The solid magenta line below 0.5% is the fringe from an uncoated crystal immersed in the $n = 1.3$ oil.

Table 10 CN SAR design.

Lyr	T (μm)	θ
MgF_2	2273.1	0 deg
Oil	10.0	—
MgF_2	2153.1	90 deg
Oil	10.0	—
MgF_2	2333.2	107.8 deg
Oil	10.0	—
MgF_2	2153.1	197.8 deg
Oil	10.0	—
MgF_2	2273.1	0 deg
Oil	10.0	—
MgF_2	2153.1	90 deg

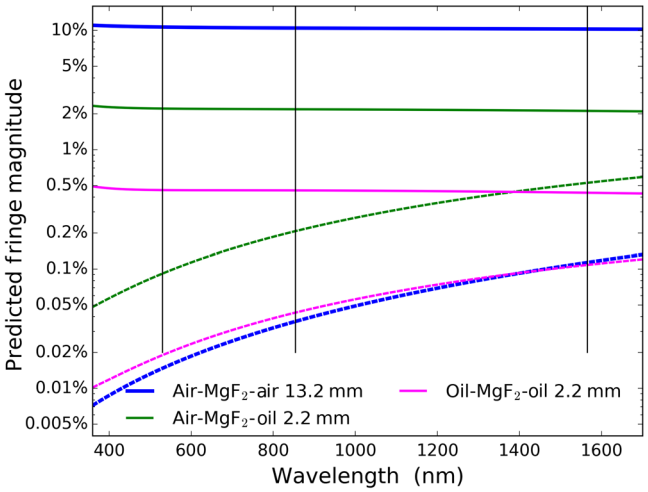

Fig. 23 Fringe magnitudes for the Cryo-NIRSP SAR at $F/13$. Collimated is shown as solid lines with the marginal ray path r^{-2} scaling as dashed lines. Blue shows uncoated 13.2-mm crystal MgF_2. Green shows 2.2 mm of crystal MgF_2 with one side exposed to air, the other to oil. Magenta shows a 2.2-mm crystal MgF_2 immersed completely in oil.

The dashed lines in Fig. 23 show the impact of the $F/13$ beam. The dashed blue line is reduced most, from 11% down to a range between 0.01% at the shorter wavelength end rising to 0.5% at the 1700-nm wavelength. The magenta and green curves represent a single crystal and are each reduced by the same factor. The air–crystal–oil interfaces at the entrance and exit of the stack are anticipated to be the dominant fringes at magnitudes below 0.05% at short wavelengths, but near 0.2% for 854 nm, a VTF instrument observing wavelength. In the infrared bandpass beyond the 2500-nm wavelength, this particular fringe component is within a factor of 2 of the collimated magnitude prediction. We show in Appendix F that the clocking oscillations for this optic are similar in magnitude between the SiO_2 retarders and the MgF_2 retarders. The MgF_2 retarders do not anticipate substantial heating from absorption of IR flux; however, all optics respond to the ambient temperature change through the day (HS18a[43]).

Table 11 shows a compilation of fringe periods, chief and marginal ray optical path properties, and spectral sampling anticipated for the Cryo-NIRSP SAR when used to calibrate various

Table 11 Cryo-NIRSP SAR fringe properties $F/13$.

Description	396 nm	854 nm	1430 nm
FWHM 100 K (pm)	3.96	8.54	14.3
FWHM 300 K (pm)	1.32	2.85	4.8
Waves thick 13.2 mm MgF_2	92,779	42,776	25,491
Marg.–chief $F/13$	35.2	16.4	9.9
Fringe period for 13.2 mm (pm)	4.3	19.9	56.1
Optical samples at 100 K	1.1	2.3	3.9
Optical samples at 300 K	3.2	7.0	11.8
Waves thick 2.2 mm MgF_2	15,473	7134	4251
Marg.–chief $F/13$	5.9	2.7	1.6
Fringe period for 2.2 mm (pm)	25.5	119.6	336.1
Optical samples at 100 K	6.4	14.0	23.5
Optical samples at 300 K	19.3	42.0	70.5

visible wavelength instruments. We list the number of optical spectral profiles (in per FWHM units) sampling a fringe period with a spectrograph of resolving power 100 K, 200 K, and 300 K. For reference, the VTF is nominally at $R = 100$ K, DL-NIRSP up to 125 K, ViSP up to 300 K, and Cryo-NIRSP up to 100 K. All DKIST instruments will likely use this optic at some wavelengths. We create two sections in Table 11 showing optical properties for spectral sampling and focal ratio behavior given the full stack of six crystals or an individual 2.2-mm-thick crystal. The chief ray path in waves is shown as waves thick in double pass through the crystal as the first line in each section. The difference between the longer marginal ray path and the shorter chief ray path in the crystal for a marginal ray at some incidence angle is computed as $(1 - \cos\ \frac{\theta_{\text{air}}}{n})\ 2dn/\lambda$, where n is the refractive index, λ is the wavelength, and θ_{air} is the incidence angle in air.

We make the small angle approximation for Snell's Law refracting from θ_{air} in air to $\theta_{\text{air}}/n = \theta_g$ in the crystal substrate. At $F/13$, the marginal ray travels at 2.20 deg in air and near 1.60 deg in the $n = 1.38$ crystal with some slight change between E and O beams. The incoming marginal ray will be spatially separated from the back-reflected marginal ray component by 1.0 mm as it travels obliquely through the crystal. The 26.6-mm-diameter beam footprint for the incident beam contracts by 2.0 mm for an 8% contraction. In each of the two sections of Table 11, we show the optical path variation in waves between the longer marginal ray and shorter chief ray. This is shown in the rows labeled Marg.–Chief $F/13$. We do not explicitly list the interference optical path difference between the incoming ray and the back-reflected component of that ray, which scales as $\cos\ \frac{\theta_{\text{air}}}{n}$. We then show the number of spectral profile FWHMs that optically sample the spectral fringe at spectral resolving powers of 300 K and 100 K. These rows approximate the optical sampling of a spectral fringe period, with the expectation that low sampling will correspond with significant spectral averaging of a fringe within an optical profile.

In Table 12, we illustrate some fringe mitigation properties in the $F/13$ beam for wavelengths of 396, 854, and 1430 nm. The first column shows the interfaces between air or oil and the optical elements in the six MgF_2 crystal modulator with uncoated surfaces. As an approximation for this table, we ignore the simultaneous solution of all coherent reflections following the Berreman calculus and simply approximate each layer as if it was alone and free standing. For instance, oil–2-mm MgF_2–oil would be the fringe magnitude for an uncoated MgF_2 crystal at 2.2-mm thickness immersed in $n = 1.3$ oil. The second column shows the wavelength for each row. The third column shows the fringe magnitude for the collimated beam (Col) for comparison with solid lines in Fig. 23(a). The fourth column shows the peak fringe magnitude predicted with the r^{-2} envelope scaling to $F/13$. The fifth column shows the fringe reduction factor for that particular wavelength and the $F/$number for the particular optic producing individual fringes.

Table 12 Fringe magnitude collimated versus $F/13$.

Optical interfaces	λ	Col	$F/13$	Fact.
Enter–optic–exit	nm	%	%	
Air–13-mm MgF_2–air	396	10.9	0.01	1272
Air–13-mm MgF_2–air	854	10.5	0.04	287
Air–13-mm MgF_2–air	1430	10.3	0.10	107
Air–2-mm MgF_2–oil	396	2.28	0.06	40.5
Air–2-mm MgF_2–oil	854	2.18	0.21	10.5
Air–2-mm MgF_2–oil	1430	2.13	0.46	4.6
Oil–2-mm MgF_2–oil	396	0.48	0.01	40.5
Oil–2-mm MgF_2–oil	854	0.46	0.04	10.5
Oil–2-mm MgF_2–oil	1430	044	0.10	4.6

4 Conclusions

The design and implementation of a fringe mitigation strategy for a suite of solar spectropolarimeters have been demonstrated. Optical contacted calibration retarders and PC instrument modulators with low beam deflection were fabricated and thoroughly tested. We showed the design, fringe properties, and fringe mitigation with the beam focal ratio in Sec. 2. The primary fringe anticipated from the original six-crystal ViSP modulator is caused by the air-to-oil interface in a single 2-mm-thick crystal and is at magnitudes of roughly 1% to 2%. We noted that this type of fringe was detected in lab testing for a six-crystal optic in Appendix A.1. The primary fringe from the upgrade PC optic is suppressed to levels below 0.1% for all of the ViSP bandpass. Section 2.2 compared fringe magnitudes and fringe reduction factors for this $F/32$ ViSP beam. We also showed additional fringe magnitude reduction from the decreased fringe period in Sec. 2.3. This is additional fringe suppression anticipated at shorter wavelengths. We showed the PC modulator is thermally stable to levels better than the six-crystal optic in Sec. 2.4. Spectral oscillations caused by clocking misalignments between crystals were shown as the major limitation of these super-achromatic designs at levels above the PC modulators for even tight manufacturing tolerances. The spatial variation of a modulator does not need to be anywhere near as small as that for a calibrator. In Sec. 2.5, we showed spatial and spectral variation properties of the ViSP PC over a 96-mm aperture. We then showed in Sec. 2.6 that the modulation efficiency loss from spatial variations many times larger than the previous six-crystal retarder did not substantially degrade modulation efficiency. The spatial variation efficiency losses were less than the efficiency loss between continuous and discrete modulation cases. The wavelength dependence of the efficiency loss was small. This relaxation of the uniformity specification for modulators should allow future consideration of alternate, possibly less uniform retarder options.

We outlined the three calibration retarders presently planned for the DKIST Gregorian Calibration Station in the $F/13$ beam. Section 3 showed the expected calibration efficiency for all three retarders given a short calibration sequence. An optical contact compound retarder was successfully fabricated and outlined in Sec. 3.2. We showed a new procedure that achieved better than 0.3-deg clocking misalignment between crystals. The thermal performance of this optic was shown in Sec. 3.2.1 with the thermal drifts of the clocking oscillations reduced, but they are ultimately still the temporal stability limit for this type of optic. We compare this new optical contact calibration retarder to the nominal six-crystal DKIST optic in Sec. 3.3. We then compared the new optical contact calibrator with the six-crystal calibrator from the perspective of fringe mitigation for each fringe component in Sec. 3.4. The $F/13$ beam does significantly reduce fringes, but the fringe from the air facing crystal in the ViSP SAR still is anticipated to fringe at magnitudes between 0.1% and 2% across visible and NIR wavelengths. The optical contact retarder eliminates the oil and has wider bandpass multilayer coatings suppressing fringes to the range of 0.02% to 0.2% across the same bandpass. The shorter period fringes from the thicker optical contact crystals should also assist in fringe mitigation. We end with a comparison of fringes to the six MgF_2 crystal calibrators that is not optimized for visible wavelengths, but should successfully calibrate many visible and NIR wavelengths. In Sec. 3.5, we show the dominant fringe is also from the air facing crystal at levels of 0.05% to 0.5% in the DKIST AO-assisted first light instrument suite bandpass.

We compiled an extensive Appendix for thorough documentation of the DKIST design and deployment of several optics serving the four first-light spectropolarimeters. In Appendix A, we showed equations and reflection losses for the various optical materials used in the UV, visible, and IR instruments. We also demonstrated laboratory detection of fringes in low-deflection PC modulators and a six-crystal quartz test retarder in Appendix A.1. PC retarders do indeed fringe when the beam deflection is small enough that the wedge does not mitigate the fringes between window interfaces. In Appendix B, we find that even individual PC retarder layers have some mild circular retardance and wavelength-dependent fast axis orientation. We update the PC retarder design for better UV bandpass predictions. We also show the design range for an example visible wavelength modulator and how we performed multiple steps of efficiency optimization with metrology of many individual test layers. Large spatial area maps of PC sheet retarders were shown with spatial variation properties of many layer retarder designs.

The spatial uniformity of crystal retarders is limited by intrinsic birefringence of the crystals. In Appendix C, we showed that successful polish of an individual crystal to better than 1/50th wave was unsuccessful at removing spatial variation of retardance, a factor of 20× less than the thickness variation would predict. Compound retarders furthermore exacerbate the spatial nonuniformity as the ridge of high retardance across the aperture following the fast axis is maximized in compound retarder subtraction orientation. We showed that the optical contact bond is very robust and actually improved over hundreds of thermal cycles in Appendix C.3.

The spatial variation of PC produces very significant part-to-part manufacturing variation. In Appendix D, we showed the fabrication of four nominally identical five-layer linear retarders that had quite different spatial and spectral variations. The DL-NIRSP instrument modulator upgrade was one part with an achieved beam deflection of 4.7 arc sec. We also show a spatial–spectral data cube analysis on a 2.5 arc sec beam deflection retarder used in an upcoming DKIST calibration system. We compare spatial retardance maps for three separate builds in Appendix D.3 and show that the wavelength dependence is not at all smooth or repeatable between builds. We demonstrate the retardance change with incidence angle in Appendix D.4 and show that spatial variation causes more depolarization than the incidence angle variation within a converging beam. We show spatial variation, spectral retardance properties, fringe magnitudes, and fringe period predictions for the upgraded PC five-layer modulator in DL-NIRSP in Appendix E. We show fringe magnitude and period predictions, thermal clocking oscillation predictions, and a comparison of spatial and spectral properties of the six-crystal MgF_2 modulator for Cryo-NIRSP in Appendix F. We end with the fringe mitigation strategy deployed for the VTF modulator using wedged windows and an achromatic design using FLCs and PC zero-order retarders in Appendix H. Wedged windows do assist in fringe mitigation, however, reflections at internal plane-parallel interfaces need to be carefully considered for refractive index mismatch.

5 Appendix A. Refractive Indices and Measuring Internal Fringes

Creating an accurate fringe model requires the refractive index and thickness for every layer in the stack, including coatings. We predict fringe behavior for various interfaces within the various DKIST optic designs. The air-to-window interface has reflections reduced by custom-designed coatings with a nominal single-surface reflectivity below 1% peak and an 0.8% bandpass average. Fringes approximately scale as $4R$ for small magnitude fringes, where R is the single surface reflectivity. We also minimize additional fringe magnitudes by matching refractive indices for the internal cement and PC layers as well as possible. Additional fringe magnitude reduction comes from choosing index-matched thick cover windows, accomplishing two tasks. The first is increasing the aperture average of spatial fringes in the converging beam (fringes of equal inclination, see HS18a[43]). Second is the significantly smaller spectral fringe periods increasing the spectral averaging over the fringes within the optical profile (e.g., our Keck LRISp set from HS18a[43] also SPEX type instruments[75–78]). We chose BK7 glass for polarization fringe mitigation as cover windows outside the stack of PC layers. Figure 24 shows the refractive index used for each layer in our polarization fringe models. For the PC, we adopt the Sultanova et al.[71] model

$$n^2 - 1 = \frac{1.4182\lambda^2}{\lambda^2 - 0.021304}. \tag{3}$$

Reference 71 is also provided in tabular form and with a fit of the experimental data with the Sellmeier dispersion formula from Mikhail Polyanskiy as shown in Eq. (3). PC is the highest as the thick black curve around 1.59 using the refractiveindex.info data base. A public BK7 equation is shown in blue with the Ohara S-BSL7 data sheet formula for our actual windows in dark blue.

We also show a vendor model of a common UV-cured optical cement from Summers called UV92 as the light green curve at index 1.52. The cement we used was Summers P92, which does not come with a dispersion equation, but simply a statement that the adhesive cures at index 1.50. We approximate a P92 model as the UV92 formula shifted down by 0.03. We highlight that these

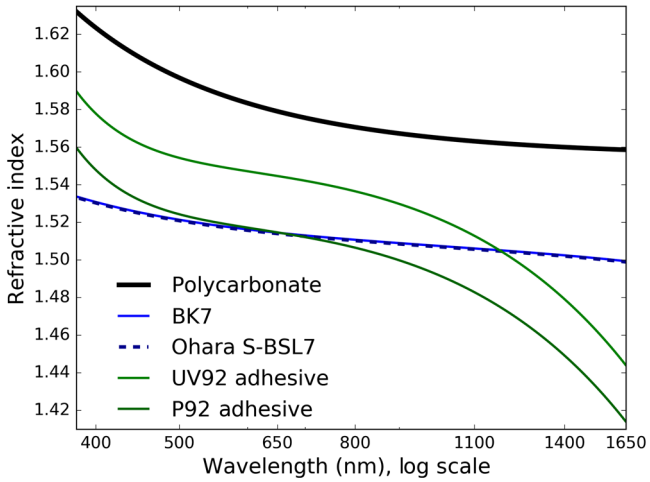

Fig. 24 Refractive index models are shown for a range of refractive index equations used in our PC optic fringe models. Black shows the PC. Red shows the P92 adhesive used by our optic modeled as the green UV92 vendor equation decreased by a constant 0.03. Dashed dark blue shows the Ohara S-BSL7 glass equation for the actual cover windows.

formulas are likely much more uncertain than other materials. They do not seem to be supported by data over a very wide wavelength range. The refractive index mismatch would have been in the range 0.12 to 0.16 for fused silica windows as used for many commonly available polycarbonate products. With Bk7, the index mismatch is in the range 0.06 to 0.10. This index match drops the single surface Fresnel loss from the range 0.16% to 0.26% for fused silica to the range 0.04% to 0.10% for BK7. This suppresses internal surface fringes by roughly one order of magnitude. The oil along with single layer isotropic MgF_2 AR coatings mitigate fringes in the six-crystal SAR designs. Figure 25 shows the reflection magnitudes computed from refractive index equations for the extraordinary and ordinary beams for crystal quartz (SiO_2) and crystal magnesium fluoride (MgF_2) retarders along with the oil.

Both quartz and MgF_2 are positive uniaxial crystals where the extraordinary beam index is higher than the ordinary beam index. We show the single surface reflection for the extraordinary beams of crystal materials interfaced to both air and oil. The dashed blue lines show an AR coating of 94 nm of isotropic MgF_2 applied to a quartz crystal. This corresponds to a quarter

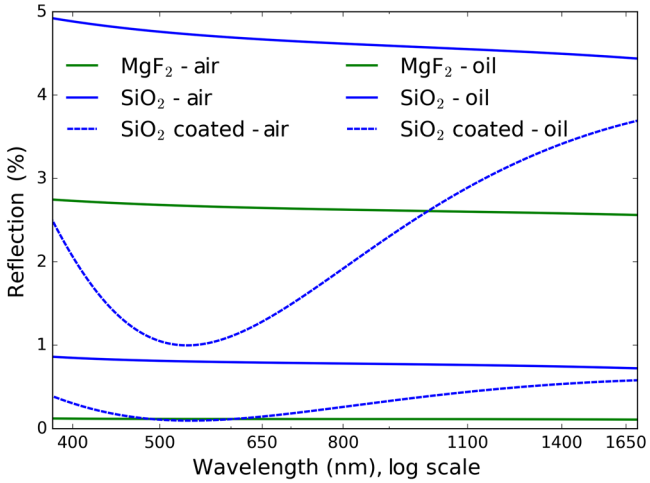

Fig. 25 Single surface reflection losses. Blue shows crystal SiO_2 to air. The middle dashed blue curve is the ViSP modulator coated SiO_2 crystal interfaced to air. The lower dashed curve is a ViSP modulator coated SiO_2 crystal interfaced to the $n = 1.3$ oil. Green curves show the MgF_2 crystals. As there are no coatings on our MgF_2 crystals, we only show the interface to air near 2.8% reflection and the interface to our $n = 1.3$ oil near 0.1% reflection.

wave of optical path at a coating central wavelength of 525 nm. Note the ordinary and extraordinary beam reflection coefficients are roughly 0.2% different from the curves in Fig. 25.

5.1 *Quartz Six-Crystal Test Retarder: Full Size Coated and Oiled Optic*

We fabricated a lab test optic using six of our spare crystal quartz retarders. This optic allowed us to do many thermal and environmental tests with direct contact to the optical surfaces without risking any of the actual calibration or modulation retarders. We were also able to do many rounds of lab testing to confirm fringe behavior with a variety of measurement systems. We describe the fringe model in this section and then show collimated beam testing below confirming measured fringe properties. The six crystals were polished and coated along with the many separate runs used for the various DKIST six-crystal achromats. The coating central wavelength varies per crystal erratically and the net retardance of the six-crystal stack is not achromatic. The A–B–A design is nominally 0 deg, 58 deg, and 0 deg with the individual spare crystals chosen to keep the net retardance behavior relatively smooth and below three waves net retardance magnitude. In Table 13, we list the thickness and description of the various layers. The AR coatings

Table 13 Quartz test retarder.

Layer	T (μm)	Note
MgF_2	0.09	CWL 525 nm
Quartz 1	2173.00	0 deg
MgF_2	0.27	CWL 1500 nm
Oil	10.00	$n \sim 1.3$
MgF_2	0.23	CWL 1300 nm
Quartz 2	2147.00	90 deg
MgF_2	0.27	CWL 1500 nm
Oil	10.00	$n \sim 1.3$
MgF_2	0.27	CWL 1500 nm
Quartz 6	2472.00	58 deg
MgF_2	0.45	CWL 2500 nm
Oil	10.00	$n \sim 1.3$
MgF_2	0.27	CWL 1500 nm
Quartz 5	2197.00	148 deg
MgF_2	0.45	CWL 2500 nm
Oil	10.00	$n \sim 1.3$
MgF_2	0.23	CWL 1300 nm
Quartz 3	2170.00	0 deg
MgF_2	0.45	CWL 2500 nm
Oil	10.00	$n \sim 1.3$
MgF_2	0.23	CWL 1300 nm
Quartz 4	2142.00	90 deg
MgF_2	0.45	CWL 2500 nm

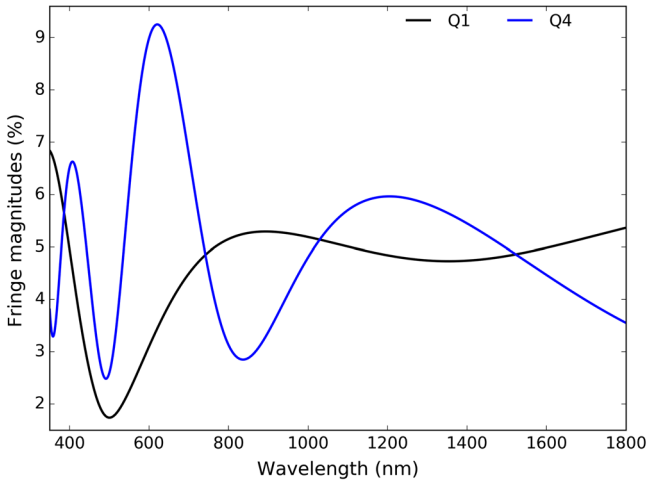

Fig. 26 Predicted fringe magnitudes for the air through coated crystal to oil interfaces for the coatings on both air-facing crystals. Each air-facing crystal has a different coating on each side, per Table 13.

are isotropic MgF_2 specified as a quarter-wave thickness at a nominal central wavelength (CWL), for Table 13. Depending on the optic, this central wavelength could be 525, 1300, 1500, or 2500 nm giving rise to physical thicknesses of the MgF_2 layer in the range of 94 to 450 nm. The transmitted wavefront had 3.4 waves of power and 1.4 waves of irregularity at the 633-nm wavelength, similar to our other six-crystal optics. We used this optic for thermal testing in the lab and also anticipate on-summit thermal testing prior to deployment of the actual DKIST calibration retarders. At the University of Hawaii Institute for Astronomy Maui labs, we were able to utilize their 0.6-m-diameter $F/5$ solar light collection mirror to feed an estimated 280 W through this optic.

We monitored the surface temperature with a forward-looking infrared (FLIR) camera over the course of a few hours to ensure the nominal temperature rise matched our thermal finite-element models from HS18a.[43] We also did not see any oil leaks at the seals or detect degradation in transmission after illumination. This optic was also used on DKIST as the preliminary thermal test retarder for assessing the impact of the 300-W beam with directly attached thermocouples verifying thermal timescales and stable operation in the beam.

We predict fringe magnitudes in Fig. 26. Spare crystal number 1 is the first air-facing crystal with an AR coating central wavelength of 525 nm on the air facing side and 1500 nm on the oil facing side. The black curve in Fig. 26 labeled Q1 shows the predicted fringe magnitude from an air-to-oil model corresponding to a drop of fringe magnitude from 7% at short wavelengths to below 2% around 525 nm rising to 5% for longer wavelengths.

Spare crystal number 4 is the other air-facing crystal with AR coating central wavelengths of 2500 nm on the air facing side and 1300 nm on the oil facing side. The blue curve of Fig. 26 shows these substantially thicker coatings give rise to spectral oscillations of fringe magnitudes in the range of 3% to 9% over the bandpass. We anticipate fringes to be produced at periods corresponding to the 2-mm crystal thickness and magnitudes in the few percent to several percent range.

5.2 *Collimated Beam Fringe Testing at IfA Maui: Retarders and Windows*

We show here fringe testing in a collimated beam for single- and multicrystal retarders as well as polycarbonate retarders. We confirm that PC retarders do indeed fringe as expected in the limit of collimated beams and small beam footprints. We show samples tested in Table 14. The six-crystal quartz test retarder has a 13.3-mm total thickness, but we expect to see fringes from the 2.1- and 2.4-mm-thick individual crystals. The PC modulator for DL-NIRSP has 3.3-mm thick cover windows and we expect to see those fringes at low magnitude as well as harmonics of that period from the two windows in the optic.

Table 14 Fringe samples.

Name	T (μm)
Quartz test.	13,300
BK7	3269
Quartz	776
DL mod.	10,260

The University of Hawaii Institute for Astronomy (IfA) Maui provided a high-resolving power spectrograph we used to measure polarized fringes. The set up consists of an equatorial tracking mount along with a 1-in. diameter lens coupling solar light to a 200-μm core diameter fiber feed. This fiber exit is collimated by a Thor Labs off-axis parabola set up on a lab optical bench. This collimated beam with a 14-mm diameter was then propagated through various test optics to assess fringes. A lens then focuses the beam onto another fiber imaging array. The IfA Maui lab spectrograph is a simple, near-Littrow spectrograph that uses a coherent fiber bundle that reformats a few mm square array into a vertical slit that feeds the spectrograph. CCD and InGaAs detectors can be used at the spectrograph focal plane. The spectrograph grating used during our testing has 316 lines per mm with a 63-deg blaze angle. The light diverging from the slit is collimated, reflected off an echelle grating at high order, passed back through the collimating lens, and focused. Our February 2019 set up used a 1.85-pm set up sampling 7920 spectral pixels covering a 14.65-nm spectral bandpass starting at 843.0 nm and ending at 857.65 nm. The sampling is at roughly one part per 460,000 with a resolving power well over 100,000. We also used an alternate wavelength set up around 792-nm central wavelength.

We show fringes detected in the six-crystal quartz test retarder using our 790-nm wavelength set up in Fig. 27. We used two separate optical set ups, one with a wire grid LP providing vertical polarization input to the crystal as seen in the black curve. We also removed the polarizer to detect fringes shown as the blue curve in what we assume is partially polarized light with an elliptical degree of polarization less than a few percent, similar to what we have measured in our NLSP fiber-coupled lamp outputs. We see the anticipated envelope structure for the beating between extraordinary and ordinary beam fringes, very similar to our single crystal fringe data and modeling in Fig. 8 of H17.[65] The power spectrum is shown in Fig. 27(b). The vertical dashed lines show fringe periods from the two air facing crystals with slightly different

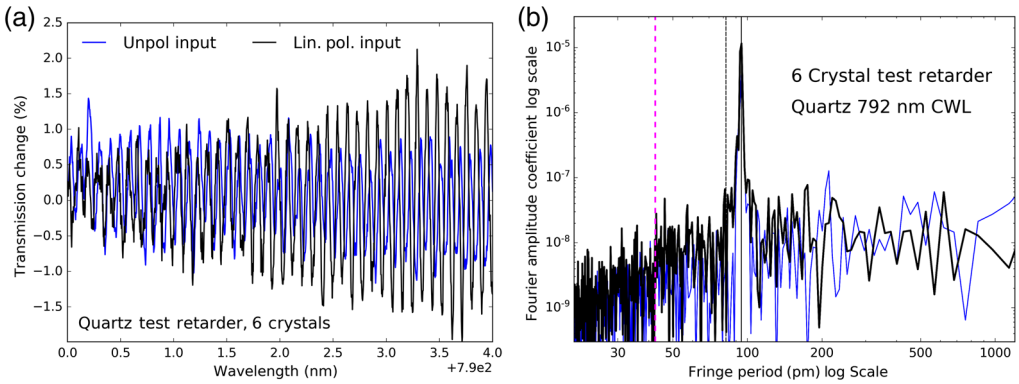

Fig. 27 (a) The measured transmission fringes for the nominally unpolarized light from the fiber in blue and the pure linearly polarized light input to the crystal stack as black. (b) The power spectrum. The single 2.47-mm crystal quartz retarder has 82.0 and 82.5 pm fringe periods at this wavelength of 792 nm. The other five crystals are close to 2.14-mm thickness corresponding to 94.6 and 95.2 pm fringe periods. The 2.47- and 2.14-mm crystal fringe periods are shown by the black vertical lines. The vertical blue dashed line shows a fringe period where we have at least five optical FWHM samples per fringe period. We expect clear detection of fringe periods to the right of this line.

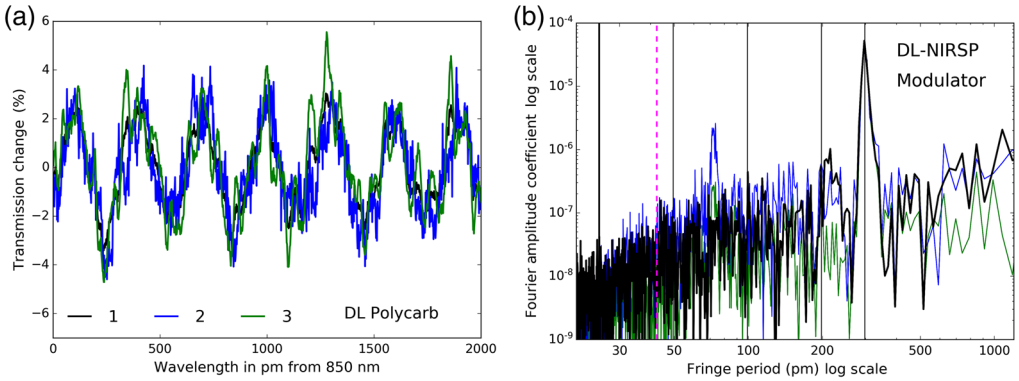

Fig. 28 (a) Transmission spectrum for the PC DL-NIRSP modulator with the 850-nm February 2019 set up. (b) Transmission power spectrum for the PC DL-NIRSP modulator. We do clearly detect fringes at the predicted fringe period. The vertical blue dashed line shows a fringe period where we have at least five optical FWHM samples per fringe period. We expect clear detection of fringe periods to the right of this line.

thicknesses. We see a very clear signal from the thinner crystal right at the primary fringe period well over 100× above the nominal background noise level. We fail to detect a fringe at harmonic frequencies or near the 16-pm fringe period corresponding to the full 12-mm stack thickness.

We have a single BK7 window from Meadowlark with a measured thickness of 3.269 mm measured with the Heidenhain gauge polished to few arc sec flatness. A quartz crystal retarder measured at 0.776-mm thickness and described in H17[65] was also used with known spectral fringe oscillations. We measured fringes in the IfA Maui set up in February 2019 over the course of a few hours. The BK7 window and crystal quartz retarder had fringes at magnitudes of roughly 7% to 18%, respectively. We performed multiple repeated removal and realignment of the optic in the set up to show stability of results. Note that we measured similar fringes, but with significantly worse SNR with the alternate camera in the June 2019 set up. The power spectrum was computed for the several spectra in our data set. Power two to four orders of magnitude larger than the noise floor were detected at the expected fringe period with minimal other peaks for both samples.

PC retarders do produce fringes both from internal interfaces in windows and also from the entire stack provided low beam deflection is achieved. We show the detailed optical and spectral properties of this upgrade PC retarder in later Appendix Secs. 9 and 10. For now, we summarize that this optic is 4.83-mm thick-BK7 cover windows with five layers of PC at a 75-μm thickness and an index-matching adhesive at a 13-μm layer thickness. We achieved a measured beam deflection of 4.5 arc sec at the 630-nm wavelength. We measured fringes in this upgrade PC modulator for DL-NIRSP in the 850-nm wavelength set up. In Fig. 28, we show the transmission fringes in (a) and the fringe power spectrum in (b). We showed above in Fig. 24 that there is a roughly 0.05% reflection from the refractive index mismatch at the BK7-adhesive to PC interface at this particular wavelength. These windows are AR coated and have a single-surface reflection around 1.3% at an 850-nm wavelength. The nominal fringe magnitude from the single window approximation is roughly 1% magnitude computed as $4\sqrt{R_1}\sqrt{R_2}$. If we estimate the fringe between both air-facing coated windows, we get a 5.2% fringe magnitude (computed as $4R$). We detect fringes in Fig. 28 at 5% magnitude. The Berreman prediction for the fastest fringe is at roughly a 25-pm period for the full thickness of the part. A single BK7 window at 4.83-mm thickness gives a fringe at a 49.5-pm period. The peak detected fringe period in Fig. 28(b) is at a multiple of 3× the period for a single window at a 297-pm period. A small peak at one third the dominant period is seen in only one of the three test power spectra. This is a clear detection of fast fringes in a PC optic.

6 Appendix B. Polycarbonate Retarder Design Optimization

We show here improvements to the PC retardance modeling with updated wavelength dependencies, variation with stretching, and new measurements of ER parameters. There are three

layers in this PC retarder design. We adjust the nominal clocking angles for the layers following the measurements of individual layer samples from stretching and mapping. The nominal design is 0 deg, 42 deg, and 147 deg clocking on layers with magnitudes of 158 deg, 108 deg, and 158 deg linear retardance at the 640-nm wavelength.

6.1 *Updating the Polycarbonate Model of Layer Retardance and Refractive Index*

We update the polynomial model used by MLO to more accurately capture behavior for wavelengths short of 420 nm. We procured 25-mm round samples of single PC sheets. MLO created the zero-order retarder samples by cementing the PC between two uncoated BK7 windows at 3.175-mm thickness each. A sample of the 108-deg magnitude PC was cut from sheet 2C, and the 158-deg sample was cut from sheet 3B. MLO measured retardance as a function of wavelength with their equipment and we also measured the same samples with NLSP. We know spatial variation is present and the centering of these samples in the beam along with the test beam diameter creates actual measurement differences. In Fig. 29, we see agreement between the MLO retardance spectra and the retardance magnitude spectrum derived from the NLSP Mueller matrix measurements. We remove the λ^{-1} trend by showing retardance in nm of phase to highlight measurement differences. MLO adapted their equipment to measure ER parameters for our project. We also show a measurement of these two samples with the new MLO technique as the dot-dashed red lines. We get good agreement with prior measurements. We use a polynomial fit to the phase retardance spectra to have a spectrally smooth model easily scalable to other wavelengths. The design ratio between retardance magnitudes was 108/158 or a factor of 68.35%. These individual samples (taken from the edge of the stretched sheet aperture) measure 104.8 deg and 162.1 deg, respectively, at a 630-nm wavelength. At a 640-nm wavelength, we get 103.05 deg and 159.36 deg for comparison with MLO data with a ratio of 64.72%.

In Fig. 30, we show scaling properties of the polynomial fits to phase retardance versus wavelength. Figure 30(a) shows the ratio of sixth-order polynomial fits after scaling for the 68.35% constant difference between layer designs divided by a direct fit to the data set itself. The fits scale by this factor with $\pm 0.2\%$ P-P. We conclude that the single polynomial fit is sufficient to

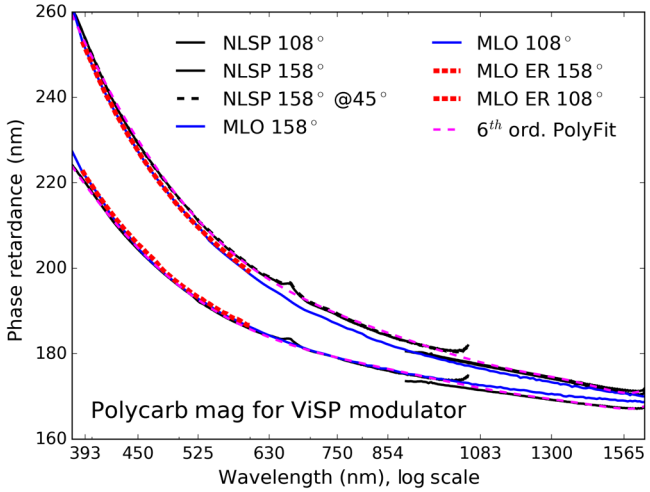

Fig. 29 Retardance magnitude derived from NLSP Mueller matrix measurements in nm of phase difference. MLO used two separate techniques with linear retardance only shown in blue. The new MLO ER measuring technique was performed and is shown in dot-dashed red covering wavelengths from 380 to 600 nm. The NLSP derivations are shown in black. Dashed black shows a repeated measurement where we rotated the part by 45 deg. Our sixth-order polynomial fits done directly to each data set are shown as dashed magenta lines. The NLSP data, MLO data, and sixth-order polynomial fits are all within roughly two nm of phase. For clarity, we have shifted all 158-deg retarder curves down by an 87-nm phase.

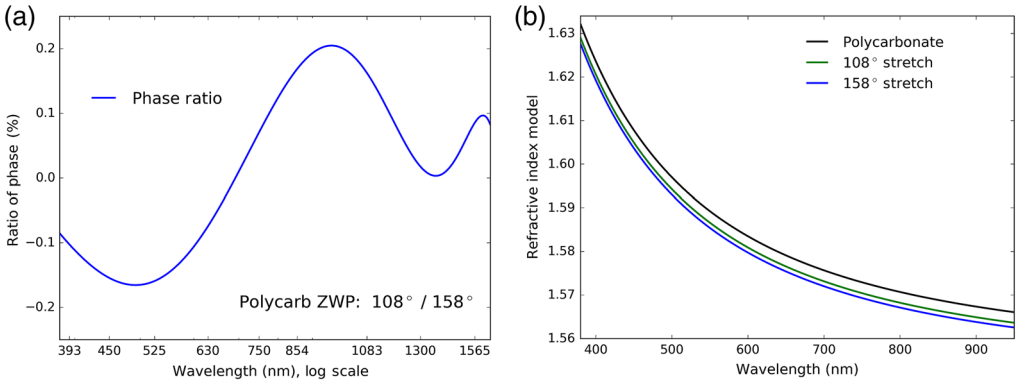

Fig. 30 The differences between polynomial models for phase retardance with wavelength. (a) The ratio of our sixth-order polynomials compensated for the 64.72% scale difference between the two fits. The two polynomials show linear scaling of 0.647 is accurate between fits to better than $\pm 0.2\%$. The polynomial fit is stable and follows a simple linear scaling to a factor better than 300×. (b) We show the refractive index derived for the extraordinary beam of both retarder magnitudes assuming the index of Eq. (3) is scaled appropriate to the measured retardance.

describe a range of layer retardance magnitudes for the purposes of design and tolerance analysis. We then convert this phase difference between polarization states to a refractive index change between ordinary and extraordinary beams following a scaling of Eq. (3) appropriate for the measured retardance given a 75-μm physical thickness measured for this material shown in Fig. 30(b). The smaller retardance stretch of the 108-deg sheet leads to a smaller index change seen as the green curve. The blue curve shows a larger retardance of the 158-deg sheet and a subsequent drop of refractive index. We use this refractive index drop in later spectral fringe modeling.

6.2 *Measured Deviation from Theoretical Achromatic Zero-Order Linear Retarder*

The stretched PC layers are not perfect ideal linear retarders. Figure 31 shows departures from the ideal linear retarder model in both fast axis orientation and circular retardance for a single

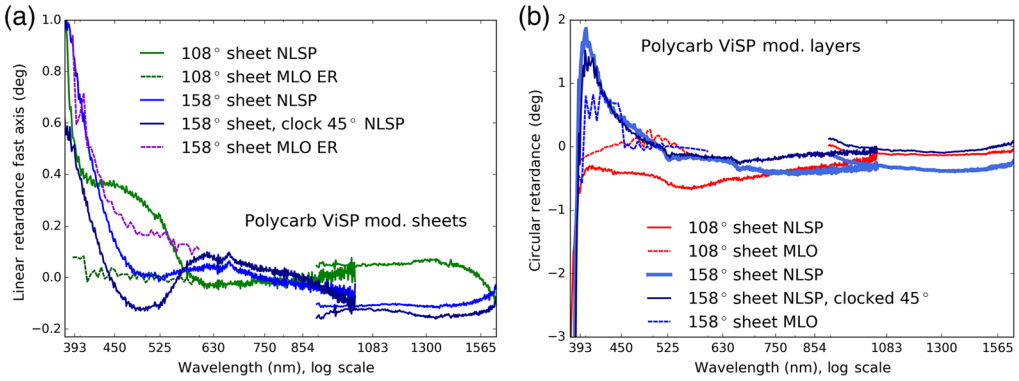

Fig. 31 Retardance properties derived from NLSP Mueller matrix measurements. (a) The fast axis of linear retardance varying with wavelength. The median fast axis value was subtracted from each curve to center all curves about zero. (b) The circular retardance component derived from an elliptical retarder model fit to the Mueller matrix. The 158-deg sheet circular retardance fits are both shown in shades of blue. Both curves agree to a fraction of a degree, though the optic was clocked 45 deg between two separate measurements. The 108-deg sheet does not show the same spectral behavior.

sheet of stretched PC. In an ideal zero-order linear retarder model, both terms should be zero at all wavelengths. The NLSP data are calculated from Mueller matrix elements after deriving the Mueller matrix with NLSP. For the MLO ER technique, they directly estimate these parameters via their photometric technique at each individual wavelength. The circular retardance and non-negligible fast axis variation with wavelength will be seen as slight departures between the models and as-built optics at short wavelengths.

We show wavelength variation of the linear retardance fast axis in Fig. 31(a). The family of blue curves shows data sets for the 158-deg sheet. The green curve compares the NLSP data set as a solid line against the MLO technique as the dashed line. We find agreement in the wavelength-dependent fast axis change for the 158-deg sheet, but the NLSP data sets show 0.1 deg to 0.4 deg variations between measurements clocking the optic. We show wavelength variation of the circular retardance in Fig. 31(b). Again, the wavelength variation of circular retardance agrees slightly better for the 158-deg sheet with a change of over 0.5 deg for wavelengths short of 450 nm.

6.3 *Designing for Uniformity: Optimizing with Many Large Area Sheets*

We took additional steps to select more spatially uniform sheets and to account for temporal changes in the PC net retardance with time between various metrology steps. We reoptimized the design based on the measured magnitude from many large area PC sheets after stretching and updating of the retardance polynomial model. We included the full wavelength range, particularly with changes in the short-wavelength bandpass. Three sheets were selected and labeled 3B–2C–3A. The orientations of 0 deg, 40 deg, and 146 deg had the best balance of efficiency after we apply 2.5-deg retardance magnitude decrease at a 640-nm wavelength as an estimate from the temporal relaxation measurements of the PC over 9 weeks. With the sheet selection, Meadowlark proceeded to measure retardance maps at 5-mm grid spacing for those particular layers. The April 2019 data on an 8-mm grid had mean retardances of 159.1 deg to 105.8 deg to 153.4 deg. The June maps at 5-mm spatial sampling have mean retardances of 157.7 deg to 104.8 deg to 152.6 deg. Estimated laminate aging from the maps is 1.02 deg to 0.83 deg to 1.43 deg. We ran another optimization using the newer mean retardance magnitudes at 0.5-deg clocking steps. A suitable efficiency balanced design is at orientations of 0 deg to 40.0 deg to 146.5 deg. We use the aperture-averaged retardance magnitude from the maps with the sixth-order polynomial to assign linear retardance spectra to each layer. We then combine each layer in a range of orientations to find a balanced efficiency and assess manufacturing tolerances. We computed a ± 0.5-deg orientation uncertainty on the individual layer orientations to assess manufacturing tolerances. The efficiency changes were <3% showing the clocking of the PC layers is very insensitive compared to other design factors. Note that this simulation only uses the average retardance over the entire spatial map as well as the sixth-order polynomial interpolation, both of which come with several errors.

In Fig. 32, we show the higher spatial sampling maps at 5-mm grid spacing for the 3B–2C–3A layers. The peak-to-valley (P-V) variation changes from 8.60 deg–13.60 deg–11.8 deg to slightly lower values of 8.21 deg–12.36 deg–11.8 deg with this higher sampling. When we trim the apertures to 105-mm circular, the mean values over the subapertures increase by 0.12 deg–0.40 deg–0.33 deg.

We simulated the likely spatial variation of ER by clocking and stacking the maps of individual layer retardance errors. As we noted in HS18,[46] different retarder designs can be factors of several more or less sensitive to spatial variations of the individual retarder components. With the clocked maps of individual layers, we can simulate the spatial variation of the three-layer stack to ensure we choose the layers most appropriate for spatial uniformity. We account for both the magnitude variation as well as the small fast axis orientation variation across the aperture. These simulations agree with the spatial variation statistics derived on the as-built optic.

In Fig. 33, we show examples of the spatial variation in ER magnitude scaled to ± 6 deg at three different wavelengths. We see similar results for the fast axis of linear retardance scaled to ± 1.5 deg. The patchy retardance variation on spatial scales of many millimeters will contribute to the depolarization and efficiency loss as the beam sweeps across this optic during modulation.

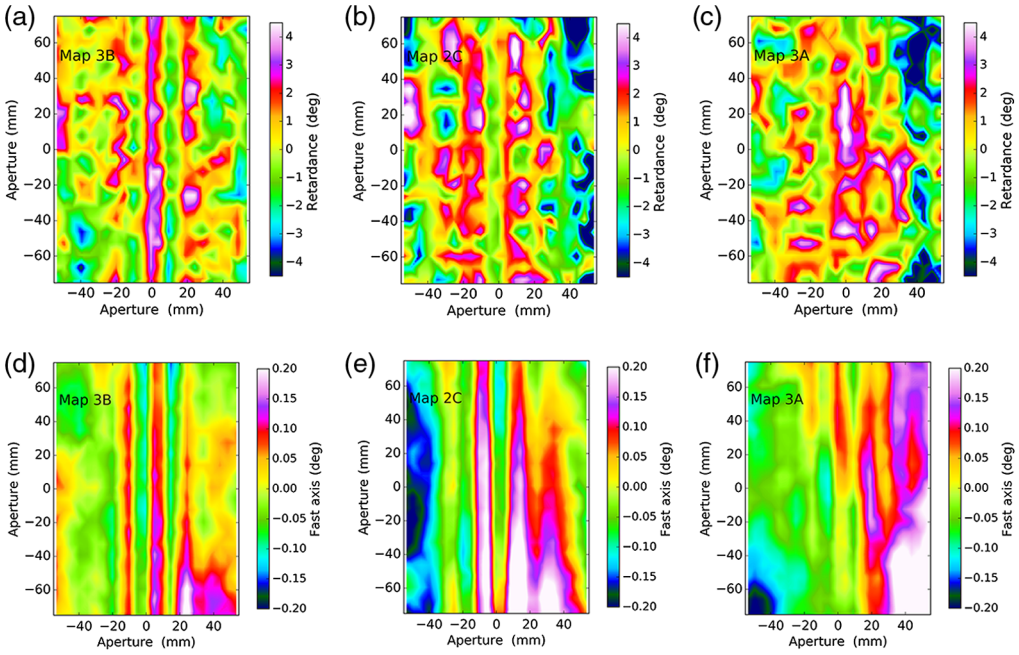

Fig. 32 Spatial retardance variation maps at 5-mm grid spacing for 3B–2C–3A measured over ± 55 mm in X and ± 75 mm in Y in June 2019: (a)–(c) linear retardance magnitude scaled to ± 4.5 deg and (d)–(f) the fast axis of linear retardance scaled to ± 0.2 deg.

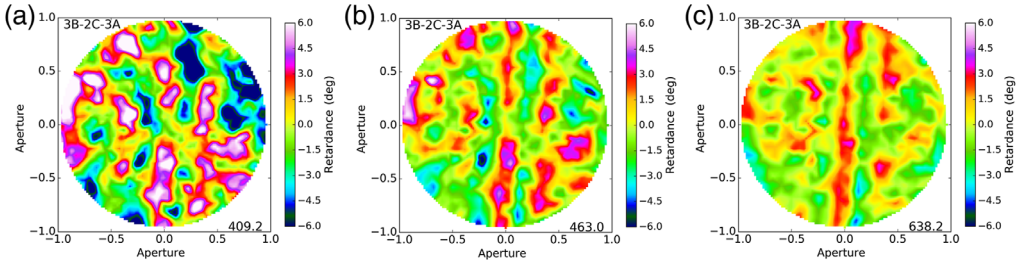

Fig. 33 Spatial variation of ER magnitude for the three-layer stacked simulation across the normalized clear aperture range of ± 1. (a) 409-nm wavelength, (b) 463-nm wavelength, and (c) 638-nm wavelength. Elliptical magnitude is scaled to ± 6 deg.

6.4 *Meadowlark Elliptical Retardance and Rotation Matrix Decomposition*

As retarders represent rotations in QUV coordinates, any rotation-based formalism can be used to describe a pure retarder. In HS18b[46] Appendix A, we used the Euler axis-angle rotation matrix representation common to DKIST retarders[79] and compared it the $Z-X-Z$-based Euler angle rotation matrix.

In the axis-angle representation of a rotation, a vector axis and the rotation magnitude are given. The axis is a unit vector e indicating the direction of an axis for the rotation. The second is an angle θ describing the magnitude of the rotation about the axis. Only two numbers are needed to define the direction of a unit vector because the magnitude of e is a specified constraint. The equation for the rotation in matrix notation is thus a magnitude times the basis vector $\mathbf{r} = \theta e$. Alternatively, the three individual components of the axis vector can be specified and the magnitude computed from the length of the three vector components

$$d = \sqrt{r_x^2 + r_y^2 + r_z^2}. \tag{4}$$

We allow the vector to not have unit length, but to be normalized explicitly in the matrix equation. We then explicitly normalize every component of $\mathbf{r}$ by d as in Eq. (4). This makes the

notation similar to common engineering references on rotation matrices as the naming corresponds to conventions of horizontal as x or preservation of Stokes Q, 45 as y or preservation of Stokes U, and R as z or preservation of Stokes V. The rotations are about the (x, y, z) axes, respectively, when the Poincaré sphere QUV coordinates are represented in (x, y, z) coordinates.

In Eq. (5), we use a notation where $\cos(\theta)$ is denoted C_θ and $\sin(\theta)$ is denoted S_θ. We adopted the notation for rotations about (QUV) as (XYZ) with the vector components (r_x, r_y, r_z) to explicitly denote an xyz coordinate frame for the rotation matrix $(\mathbb{R}_{ij})$

$$\mathbb{R}_{ij} = \begin{bmatrix} \frac{r_x^2}{d^2} + \left(\frac{r_y^2+r_z^2}{d^2}\right) C_\theta & \frac{r_x r_y}{d^2}(1-C_\theta) + \frac{r_z}{d} S_\theta & \frac{r_x r_z}{d^2}(1-C_\theta) - \frac{r_y}{d} S_\theta \\ \frac{r_x r_y}{d^2}(1-C_\theta) - \frac{r_z}{d} S_\theta & \frac{r_y^2}{d^2} + \left(\frac{r_x^2+r_z^2}{d^2}\right) C_\theta & \frac{r_y r_z}{d^2}(1-C_\theta) + \frac{r_x}{d} S_\theta \\ \frac{r_x r_z}{d^2}(1-C_\theta) + \frac{r_y}{d} S_\theta & \frac{r_y r_z}{d^2}(1-C_\theta) - \frac{r_x}{d} S_\theta & \frac{r_z^2}{d^2} + \left(\frac{r_x^2+r_y^2}{d^2}\right) C_\theta \end{bmatrix}. \tag{5}$$

In earlier works, we have used a Euler formalism to describe rotation matrices.[41,42,58,80–84] In the three Euler angle rotation formalism, there are three successive rotations about specific coordinate axes. We denote the three Euler angles as (α, β, γ). We use notation where $\cos(\gamma)$ is shortened to c_γ.

Equation (6) shows a Euler angle style rotation matrix $(\mathbb{R}_{ij})$ using the ZXZ convention. Successive rotations are applied in sequence, first about the Z axis, second about the X axis, then third about the new Z axis. This would be analogous to a circular retarder (Q to U, x to y) followed by a linear retarder with fast axis at zero (U to V, y to z) followed by another circular retarder (Q to U, x to y). There are 12 independent Euler angle conventions for a sequence of rotations about the coordinate axes such as XZX, YZY, etc.,

$$\begin{aligned} \mathbb{R}_{ij} &= \begin{pmatrix} c_\gamma & s_\gamma & 0 \\ -s_\gamma & c_\gamma & 0 \\ 0 & 0 & 1 \end{pmatrix} \begin{pmatrix} 1 & 0 & 0 \\ 0 & c_\beta & s_\beta \\ 0 & -s_\beta & c_\beta \end{pmatrix} \begin{pmatrix} c_\alpha & s_\alpha & 0 \\ -s_\alpha & c_\alpha & 0 \\ 0 & 0 & 1 \end{pmatrix} \\ &= \begin{pmatrix} c_\alpha c_\gamma - s_\alpha c_\beta s_\gamma & s_\alpha c_\gamma + c_\alpha c_\beta s_\gamma & s_\beta s_\gamma \\ -c_\alpha s_\gamma - s_\alpha c_\beta c_\gamma & -s_\alpha s_\gamma + c_\alpha c_\beta c_\gamma & s_\beta c_\gamma \\ s_\alpha s_\beta & -c_\alpha s_\beta & c_\beta \end{pmatrix}. \end{aligned} \tag{6}$$

MLO provided their ER data in the form of a $Z - X - Z$ style decomposition

$$\mathbb{R}_{ij} = \mathbb{R}_z(-\alpha)\left[\mathbb{R}_z\left(\frac{\beta}{2}\right)\mathbb{R}_x(\gamma)\mathbb{R}_z\left(\frac{\beta}{2}\right)\right]\mathbb{R}_z(\alpha). \tag{7}$$

In Eq. (7), they use three parameters (α, β, γ) in a five-matrix series of rotations. The outer rotations about Z by the parameter α represent a physical rotation of the optic. The two interior rotations about Z with magnitude $\beta/2$ correspond to circular retarders. The interior rotation about x with magnitude γ is a linear retarder with fast axis at zero. In Eq. (8), we show the interior rotation matrix in terms of β and γ explicitly after combining the $Z - X - Z$ rotations. The exterior rotations about Z for the parameter α are just a clocking of the optic against the incoming beam (fast axis rotational orientation)

$$\mathbb{R}_{ij}(\beta, \gamma) = \begin{bmatrix} c_\beta^2 - c_\gamma s_\beta^2 & (1+c_\gamma) s_\beta c_\beta & -s_\gamma s_\beta \\ -(1+c_\gamma) s_\beta c_\beta & -s_\beta^2 + c_\gamma c_\beta^2 & -s_\gamma c_\beta \\ -s_\gamma s_\beta & s_\gamma c_\beta & c_\gamma \end{bmatrix}. \tag{8}$$

We translate the Meadowlark parameter sets between this formalism and our axis-angle style. We find exact numerical equivalences between rotation matrix formalisms and also agreement between multiple metrology techniques.

6.5 *MLO and NLSP Metrology Comparison: Elliptical Retardance Parameters*

Our NLSP metrology agrees quite well with the new ER technique used at MLO for this project. We procured a 1-in. diameter test part with uncoated BK7 windows using the same layers, stretch design values, and epoxy as the full-sized ViSP modulator upgrade. MLO also adapted their spectral retardance metrology system to output ER parameters using a $Z - X - Z$ style rotation decomposition. The three PC layers were stretched to magnitudes of 156.88 deg, 106.59 deg, and 157.95 deg, respectively. This corresponds to phases of 278.9, 189.5, and 280.8 nm at a 640-nm wavelength. The polymer layers have thicknesses of 72, 74, and 72 μm. This particular optic was clocked at 0 deg, 42 deg, and 147 deg. Note that the reoptimized design for the ViSP optic is 0 deg, 40 deg, and 146.5 deg. The two BK7 windows have thicknesses of 3.247 and 3.234 mm, respectively. The total part thickness was 6.753 mm. The difference between the measured total part thickness and the thickness of each component is 54 μm, which we attribute to the adhesive with an average thickness of 13.5 μm in each of the four layers. The beam deviation is 3.9 arc sec at a 632.8-nm wavelength. The transmitted wavefront is 0.114 waves PV with a root mean square (rms) of 0.020 waves over a 21-mm area. The power was 0.026 waves with 0.07 waves astigmatism.

We compare MLO metrology to Mueller matrix measurements with NLSP. Figure 34 shows the MLO elliptical retarder parameter fits using their decomposition in (a). In Fig. 34(b), we translate their measured ER parameters to our axis-angle formalism through fitting the derived Mueller matrix for the optic. Note that the two rotation matrices are numerically identical. Differences are only from measurement and modeling errors. The axis-angle elliptical parameters derived from the Mueller matrix predicted by the MLO measurements are shown as the thick dashed lines. The thin solid lines show axis-angle ER parameters derived from NLSP measurements of the 1-in. mock up Mueller matrix. The optic was clocked in NLSP to show the level of systematic errors upon rotation of an optic with the 4 arc sec of beam deflection and spatial retardance variations. The three NLSP parameter set fits have been derotated to set the fast axis of linear retardance to zero at an 800-nm wavelength. The MLO measurements and the three NLSP measurements over plot within the line width. The dot-dashed line shows the axis-angle ER parameters derived from an as-built model of this one-in. mock up. We use the individual layer stretch values measured by MLO and the nominal clocking orientations. This model is thus three pure linear retarders with sixth-order polynomial fit retardance magnitudes scaled to 156.88 deg, 106.59 deg, and 157.95 deg at a 640 nm-wavelength, respectively. The nominal clocking is 0 deg,

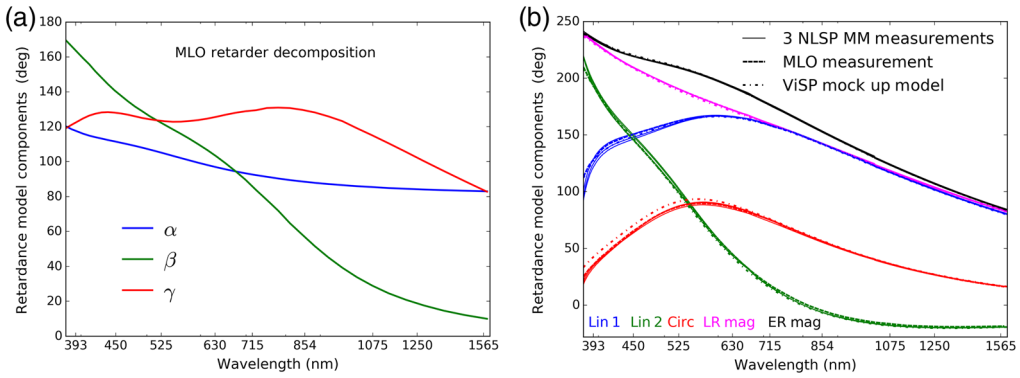

Fig. 34 (a) The MLO decomposition model for an elliptical retarder parameter. The azimuth α is shown in blue. The linear magnitude as γ is shown as red. The optical rotation component is shown in green as β. (b) The Euler axis-angle parameters with all parameters rotated to have a linear fast axis of 0 deg at 800-nm wavelength. The model for the 1-in. test part made by Meadowlark using the polynomial equations fit to the as-built 640-nm retardances and orientations are shown as dot-dashed lines. Three NLSP Mueller matrix measurement parameter fits are shown as thin solid lines. The axis-angle parameter fit to the Mueller matrix created with the MLO measurements at left are shown as the thick dashed lines. Note that both the MLO decomposition and the axis-angle formalism produce numerically identical Mueller matrices and are equivalent representations of the retardance for this as-built optic.

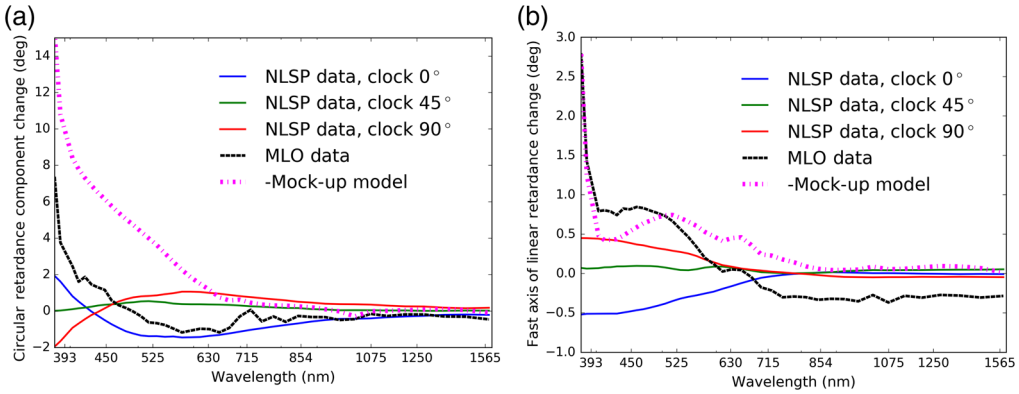

Fig. 35 (a) The difference between each individual circular retardance curve and the average of the three clocked NLSP measurements. The dashed magenta model calculation used the magnitudes measured at a different spatial location likely leading to the differences through the high parameter sensitivity shown above. The MLO and NLSP measurements were both roughly centered on the aperture of the as-built part and sample much more similar spatial regions of the optic. (b) The difference between each linear retardance fast axis individual curve and the average of the three clocked NLSP measurements.

42 deg, 147 deg for each layer. There are two major error sources between this model and both measurement sets. The individual layers were not measured at the same spatial location as the aperture-center of the 1-in. mock up part. We expect at least a few degrees variation in magnitude per layer from this spatial variation given a few centimeters of spatial difference between the individual layer metrology and the final centered and epoxied stack. There is also a nominal ± 0.3-deg clocking error from normal manufacturing tolerances contributing to the difference between model and measurements.

In Fig. 35(a), we compare the circular retardance measurements and the spectral differences between the various measurements and model. As we showed above, the circular retardance parameter shows spatial variation at amplitudes more than double the two linear components. The MLO measurements agree with the NLSP data sets to within a few degrees of that component. In Fig. 35(b), we compare the fast axis of linear retardance and the spectral differences between the various measurements and model. Figure 35(a) shows the smooth and consistent spectral variation of the fast axis with wavelength between all models and measurements. Figure 35(b) shows the difference between each individual curve and the average of our three NLSP measurements derotated at an 800-nm wavelength. There is a 0.5-deg divergence between the three NLSP measurements. The MLO data are different from NLSP by up to 2.5 deg at blue wavelengths, but this is well within the range of anticipated spatial variation.

6.6 *ViSP Polycarb Modulator Beam Deflection and Transmission*

We contracted Meadowlark to collaborate and develop a new active alignment technique to minimize the wedge in the final assembly after curing the adhesive and installation of cover windows. Typical commercially available PC retarders have beam deflection from cover window parallelism errors of roughly a few arc minutes. Here, we show successful development of optics that hit beam deflections of a few arc sec, 60× lower than is typically available.

A common statement is that PC retarders do not cause polarization fringes. This statement is generally misleading as PC retarders are also effectively wedged by a few arc minutes or more, which suppresses fringes. Many applications must minimize the image displacement caused by optic rotation during calibration or modulation. We required beam deflection in the range of arc sec, not arc min. In Table 15, we list some of the optical properties derived from measurements of the transmitted wavefront. We compare the six-crystal super achromat ViSP PCM with this upgrade ViSP PC modulator. With the cover windows and adhesive, we manage to get factors of a few to several improvements in all the transmitted wavefront properties. This reduces image motion and image degradation.

Table 15 Comparing six-crystal versus PolyCarb.

Parameter	Six-crystal	PolyCarb	Dif
Beam deflect.	6.4 arc sec	2.3 arc sec	2.8×
Power TWE	4.04 waves	0.56 waves	7.2×
Irreg TWE	1.64 waves	0.67 waves	2.4×
Total TWE	4.56 waves	0.92 waves	5.0×

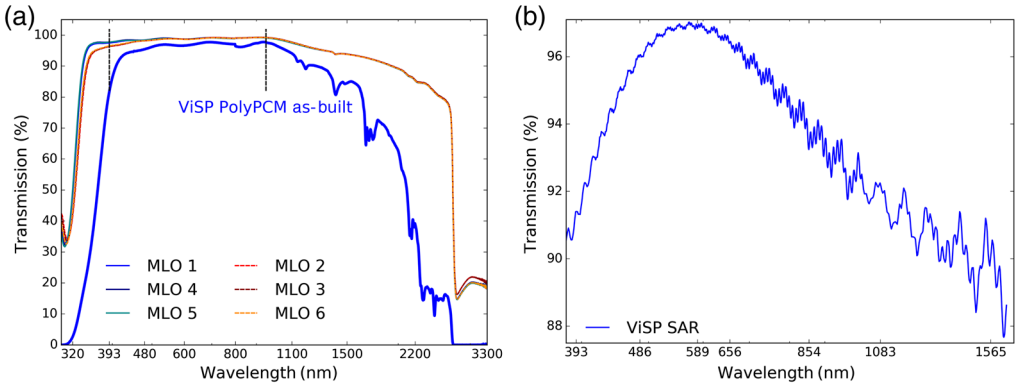

Fig. 36 (a) Transmission of the PC modulator upgrade for the ViSP along with multiple coating witness sample comparisons. Some coatings showed significantly different UV absorptions. (b) Transmission measured with NLSP for the ViSP SAR. Many oscillations are seen.

Figure 36(a) shows the transmission measured for the final assembly of the PC modulator covering the full 300 to 3000 nm spectral bandpass measured at 0-deg incidence angle in the MLO Varian Cary spectrophotometer as the solid blue curve. The 393-nm wavelength transmission is 82.3% rising to 85.2% at 396 nm. The loss can be roughly attributed to two 4% surface losses combined with 7% absorption of the combined three PCs and four adhesive layers. In addition, we tested single PC retarder sheet samples containing two BK7 windows, two adhesive layers, and a single PC layer. Another sample was tested with just two windows and one adhesive layer. We discovered that roughly half of the coating samples used to create the single-layer test retarders showed some UV absorption. Subsequent data from Infinite Optics, MLO, and our own systems confirmed this behavior. We show six sample spectrophotometric measurements taken at MLO and note the few percent disagreements between samples as possible coating absorption present in the upgraded ViSP modulator. A set of individual BK7 windows were also measured with a Fourier transform infrared spectrophotometer. Thus, we can separate the behavior of the coatings from internal absorption for the purposes of the fringe models here.

Figure 36(b) shows the transmission of the six-quartz crystal SAR measured with NLSP for reference. Interference is obvious with oscillations across the wavelength range. The single-layer MgF_2 coating design thickness was quarter wave at 525 nm causing the transmission peak at that wavelength. However, the loss of coating transmission and subsequent fringe magnitudes can be seen at short and long wavelengths.

7 Appendix C. Optical Contact Quartz Retarder *F*/13

Significant metrology was done during fabrication of each crystal before coating. The first crystal was polished, measured for transmitted wavefront, sent for deterministic fluid jet polishing, and received with a final 4.233-mm physical thickness. The preliminary polish was 10^{th}-wave transmitted wavefront error (TWE), but the deterministic polishing improved this to better than a 12-nm peak error ($\lambda/53$). Note that 12 nm of TWE is roughly 7.7 nm of physical thickness

Table 16 Crystal thickness and WFE.

N	Thk (mm)	TWE (P-P)	rms (wvs)	Pwr (wvs)	BDev (arc sec)
1	4.233	0.124	0.012	0.022	0.05
2	4.247	0.510	0.110	0.228	1.85
B	8.475	0.66	0.12	0.32	1.20

variation at refractive index 1.55. Given the crystal quartz birefringence, this transmitted wavefront spec would correspond to 0.04-deg retardance variation across the aperture.

The second crystal must be polished to a physical thickness identical to the first crystal plus or minus 0.23 waves net retardance. This corresponds to a 15.974-μm physical thickness difference. We specify a tolerance of ± 0.02 waves retardance about this target to ensure reasonable calibration efficiency. We note that the spatial retardance maps of the air gapped parts shown later suggest 0.224 waves net retardance and a corresponding thickness difference of 15.557 μm. The total thickness of both crystals would be around 8.48 mm. Table 16 shows the metrology of the crystals before AR coatings as well as testing the final as-built optic performed at MLO. The first column identifies the crystal number. The B denotes both crystals after contact. The second column shows the physical thickness measurements with the Heidenhain linear gauge set up. Note that any dust under the optic can skew the thickness measurements by a micron or a few in optical contact.

Both parts were also remeasured in the Heidenhain gauge without optical contact and the difference was still roughly 14 μm. However, each crystal was on an $\sim$10-μm-thick air layer adding thickness (4.244 and 4.257 mm) and measurement uncertainty. The third column shows the TWE for both crystals with piston-tip-tilt removed in waves. The fourth column shows the rms wavefront error in waves. The fifth column shows the Zernike power term of wavefront error (Pwr) in waves. The sixth column shows the beam deflection measured in an offset subaperture using a reference flat. The beam deflection was 0.05 arc sec for crystal 1, which compares very well with the 0.06 arc sec measured at the fluid polishing vendor. The second crystal has a beam deflection of 1.85 arc sec. The optically contacted part was measured at 1.2 arc sec beam deflection.

7.1 *Quartz Optical Contact—Fluid Polishing and Spatial Mapping of Retardance*

We attempted to substantially improve the spatial uniformity of retardance for this calibration optic, but identified a significant limitation in the manufacturing process. We added a deterministic fluid jet polishing procedure to one of the crystals on the assumption that transmitted WFE correlates with retardance through the thickness variation. However, this does not account for other effects internal to the crystals. The fluid polish procedure reduced the TWE on one crystal from $\lambda/10$ to $\lambda/52$. This process did substantially improve the retardance uniformity compared to the nominal blocked stick polishing technique, leaving a residual retardance spatial variation with a ridge type feature at $\sim$1 deg P-P generally following along the fast axis direction. The fluid polish flattened the wavefront to 12 nm P-P TWE. The 12-nm WFE would contribute 7.7 nm of crystal thickness variation, which would correspond to 0.04 deg retardance variation. This is a factor of roughly 20× less than the residual error on crystal retardance map 1. This suggests that using wavefront error or thickness as a proxy for retardance is not sufficient to achieve uniformity better than 1 deg. Compound retarders are also pathologically bad for uniformity on this particular type of error. Ridges of high retardance along the fast axis are maximally exacerbated in the compound retarder with the required 90-deg fast axis relative orientation. With each crystal having a 1-deg ridge, a 2-deg "saddle" will be produced in a compound retarder. We see this behavior in all the DKIST quartz retarders published in HS18b[46] (Figs. 14, 42, and 44). In these optics, three compound retarders were combined in an A–B–A style with the calibrators as a linear super achromat.

Table 17 Retardance spatial mapping properties.

N	Bias (wve)	λ (nm)	δ_{avg} (wve)	δ_{med} (wve)	θ_{fast} (deg)	rms (deg)	P-P (deg)
1	60	631.0	0.75383	0.75351	0	0.56	2.90
2	60	633.4	0.75083	0.75084	90	1.10	4.66
B	120	630.0	0.22379	0.22401	90	1.35	7.95

The individual crystals were spatially mapped for retardance along with an air-gapped assembly of both crystals in compound zero-order configuration. In Table 17, we compile the thickness and retardance properties of the crystals during mapping. The first column shows the crystals. The B denotes both crystals mounted together in compound zero-order retarder configuration. The individual crystals have a bias retardance of 60.0 waves around the 630-nm wavelength shown in the second column. With thick crystals, the sensitivity to temperature and incidence angle is very strong making comparison between different equipment and theories difficult.

The retardance spatial mapping equipment is more accurate and faster with optics near some odd integer multiple of quarter wave net retardance. Thus, the spatial retardance mapping was done at slightly different wavelengths to ensure both were quarter waves. Crystal 1 was predicted to be 60.368 waves retardance at 20°C and the 631.0-nm wavelength. Crystal 2 is 0.23 waves retardance and 16.7 μm thicker leading to a prediction of 60.351 waves retardance at 20°C and a 633.4-nm wavelength. The measurement wavelength is shown in the third column of Table 17. The wavelengths were chosen so the optic was close to quarter wave retardance at laboratory temperatures. Note that 5°C temperature change corresponds to 0.05 waves net retardance changes for these 4.2-mm-thick crystals around a 630-nm wavelength.

The fourth column of Table 17 shows the average retardance over the aperture (δ_{avg}) for each map. The fifth column shows the median retardance to show the impact of the few outlier data points is minimal (δ_{med}). In the sixth column, we show the rough orientation of the fast axis of linear retardance (θ_{fast}). The seventh column shows the rms variation of magnitude across the measured aperture. The eighth column shows the P-P variation of ER magnitude across the measured aperture in degrees. Figure 37 shows the retardance of the individual 4.2-mm-thick quartz crystals spatially mapped at 3 mm spatial sampling with a 4-mm-diameter beam at the 631-nm wavelength. The wavelength range sampled for each map is roughly 0.15 nm FWHM around the 630-nm wavelength giving a 0.024% bandpass or one part in 4200 with the combined

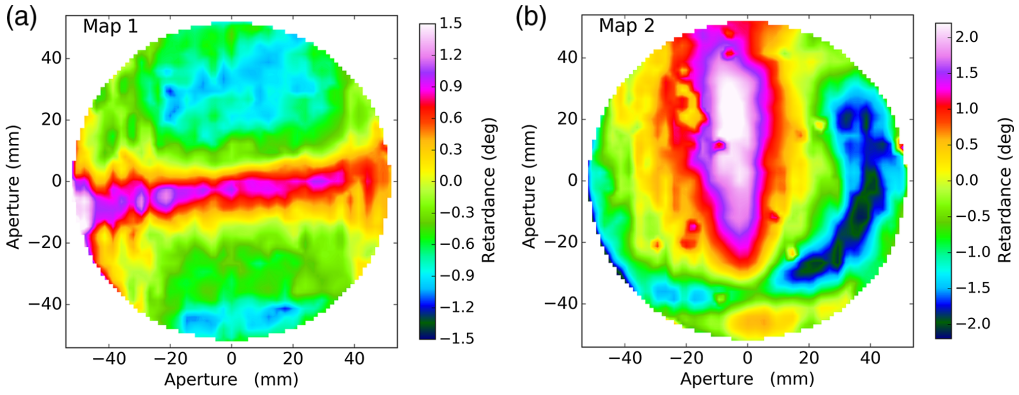

Fig. 37 Preliminary spatial retardance elliptical magnitude variation map of individual crystals at 3-mm sample spacing, 631-nm wavelength. Crystal 1 shown in (a) has been fluid jet polished and is displayed on a $\pm$1.5-deg retardance color scale. Crystal 2 is shown in (b). Crystal 2 was polished to match crystal 1 thickness plus ~16 μm for a net retardance 0.23 waves greater than crystal 1. The crystal 2 map is shown on a $\pm$2.2 deg retardance color scale.

monochromator and narrowband isolation filter. Retardance was thermally compensated every 10 measurements (15-min cadence) via linear interpolation from measurements at part center. The orientation of each individual crystal was matched to the air-gapped compound zero-order configuration presented later. The first crystal (fluid polished) was oriented with the chord down and the surface marking arrow up. The second crystal was oriented chord right and the surface marking arrow down. Thus, the fast axis for the first crystal is vertical and is horizontal for the second crystal. In the color scheme of Fig. 37, there is an obvious linear feature as the white-magenta coloring essentially following the fast axis of each retarder, horizontal for crystal 1 and vertical for crystal 2.

7.2 *NLSP Mueller Matrix Mapping: Spectrograph Upgrade and Statistics*

We implemented a new option in our NLSP to use an Avantes evolutionary (EVO) CMOS-based spectrograph for our visible channel. This upgrade increases the effective NLSP pixel count by a factor of three and our spectral resolving power by a factor of four. Our CCD system covers 379 to 1120 nm with 1320 spectral pixels. This new CMOS system covers 541.7 nm of bandpass with 4032 spectral pixels from 390.3 to 931.9 nm wavelengths. We also use masked reference pixels from each end of the EVO CMOS sensor. The EVO unit delivers an optical FWHM of 0.3 nm compared to 1.2 nm for our CCD system.

We ran a spatial map of Mueller matrix spectra with NLSP covering a 90-mm aperture in a rosette spatial pattern with 3-mm sample steps and a 60-deg first ring radius. We collected 721 Mueller matrix spectra over 6.5 days of machine time at 13 min per spatial position. We show the spectral clocking oscillations for the central spatial location in our aperture in Fig. 38(a). We now have the spectral resolving power to measure these oscillations clearly. Figure 38(b) shows the spatial variation of each retardance component as a function of wavelength. We take the 721 measurements across the aperture and compute the standard deviation for each component. The black dashed curve shows the ER magnitude, which tracks very closely to the blue curve as the first component of linear retardance. The green curve is the second linear component multiplied by 3 for clarity. The red curve shows the spatial variation of circular retardance multiplied by 4 for clarity. The fast axis of retardance was essentially noise limited about zero spatial variation. The clocking oscillations are clearly seen in the spatial variation. These 6.5 days of data collection were done in a university campus lab that is not temperature or access controlled. The maps at different wavelengths are essentially identical. The standard deviation and spatial variation follow the expected λ^{-1} behavior well.

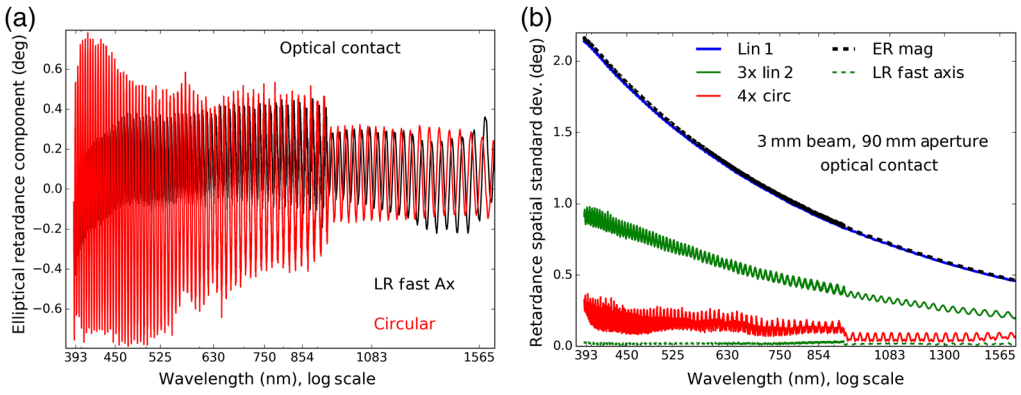

Fig. 38 (a) The clocking spectral retardance oscillations at the NLSP map center point. The new EVO system covers wavelengths short of 930 nm. Circular retardance oscillations in red are over 1.2 deg P-P. The fast axis oscillations are at roughly 0.4 deg with some systematic errors visible in the wavelength dependence. (b) The standard deviation of the spatial variation for each retardance component at each wavelength. Blue shows the first component of linear retardance. Green shows the second component multiplied by 3. Red shows circular retardance multiplied by 4. The dashed green curve down near zero shows the fast axis of linear retardance.

7.3 *Optical and Quartz Retarder Lab Testing with 300-W Beam*

There are several concerns about using a large area optical contact bond in an optic used in an enclosure tracking ambient outdoor temperatures on a mountain top environment with significant heating anticipated from use in the concentrated solar beam. Stress birefringence is also a concern. We contracted a detailed thermal analysis to Hofstadter Analytical LLC to assess the optical contact quartz in response to the 300-W beam, similar to H18.[43] We initially intend to use this retarder in calibration sequences always protected by the calibration polarizer. This reduces the heat load by a factor greater than 2 and reduces depth-dependent heating after accounting for the polarizer substrate IR absorption plus reflection of more than half the flux. The flux budget combined with depth-dependent absorption give rise to roughly 0.56 W being dissipated through the 8.4-mm volume of the optic. Similar to H18,[43] we test several assumptions about convection coefficients, natural convection versus forced air flow inside the DKIST Gregorian Optical System enclosure, and conductivity through the room-temperature vulcanizing silicone bond line into the cell and rotation stage. We ran models with no convection, natural convection, and forced convection with a worst-case geometry where the optic surface is normal to gravity, suppressing convection on the bottom optical surface.

In Fig. 39, we show outputs of the finite-element model after 60 min of illumination for the natural convection case. Figure 39(a) shows the physical deformation on a color scale from −2.17 to +0.80 μm. Deformation of a few microns from the differential expansion along *o*- and *e*-directions will not cause significant impact on wavefront or retardance. Depending on the convection model assumed, the temperature rise is between 2°C and 4°C after 1 h of illumination in the beam. Figure 39(b) shows a temperature distribution on a color scale from 22.47°C to 23.11°C. There is a mild temperature gradient from the center of the optic to the edge of <1°C. The thicker, optically contacted crystals conduct the load with depth to reduce temperature differences below 0.1°C between the top and bottom of the optic. The temperature gradients with radius and depth have impact on the field angle-dependent calibration with this optic as outlined in HS18.[43] Assumptions about the balance between surface convection and conduction to the cell slightly change both the depth gradient and the radial gradient, but these terms remain small.

Figure 39(c) shows the von Mises stress in the crystal on a color scale from 14 to 378 kPa. This stress combines normal and shear stresses to estimate a single-stress value relevant for the stress birefringence calculations, though not necessarily normal to the optical beam. The shear stresses internal to the optic relevant to the optical bond are roughly 50% less than the von Mises stress levels. Most of the illuminated aperture is below 200 kPa. We note that the stress-induced retardance from this stress is well below many other error sources. We performed multiple optical contacts to obtain a clean bond. To debond the crystals, they had to be differentially heated on a hot plate and pried apart with a blade and substantial manual force. The nominal DKIST operating temperatures even under a 300-W beam load should be a safety factor of several below

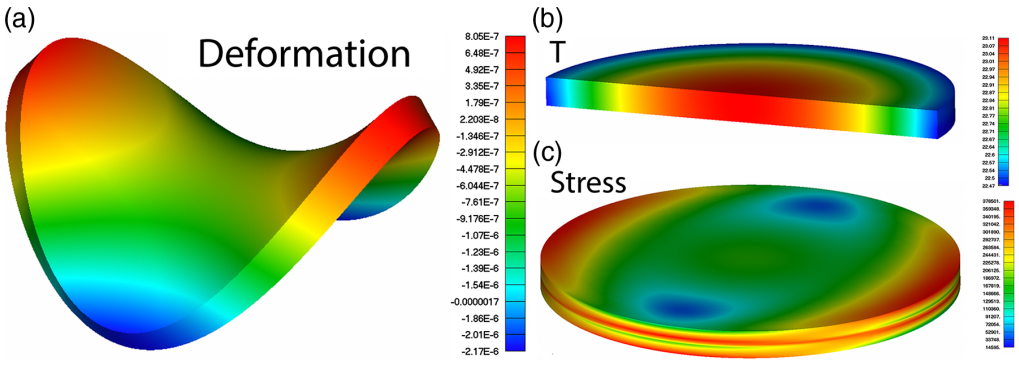

Fig. 39 Optical contacted quartz compound retarder thermal finite-element models. (a) Deformation on a −2.17- to +0.80-μm scale after 60 min of heating at 0.56 W using depth-dependent absorption. (b) Temperature from 22.47°C to 23.11°C for a 2.8°C average rise. (c) von Mises stresses in the deformed crystal in the range of 14 to 378 kPa.

the bond yield strength. We also put the optic through 168 h of environmental chamber testing. We used a 40-min cadence changing from 1°C to 40°C with a 4°C ramp rate and 20-min hold times for 252 thermal cycles. Pictures pre- and post-testing showed no measurable change in the bond nor the known points of noncontact.

We also note that we were able to roughly confirm some of the thermal predictions of H18[43] for absorptive heating of a solar beam using the six-crystal quartz test retarder. We used a 24-in. diameter $F/5.3$ collecting mirror at IfA Maui to direct solar flux through test optics. We observed in the morning from an elevation of 10 deg to 30 deg collecting an estimated 180 W early to 240 W later through the optic, compared to a maximum around 294 W for DKIST Gregorian focus at an airmass of 1. We combined atmospheric radiative transfer models with a range of protected aluminum coating models for the collector mirror to estimate the spectral flux absorbed by the optic. We estimate this thermal testing to have produced 0.9 to 1.7 W absorbed power in the quartz test retarder as a function of airmass compared to a 2.5-W peak at DKIST. We observed a roughly 10°C rise using an FLIR camera calibrated for the Fresnel losses and atmospheric path. This is compared with the DKIST model prediction of 13°C rise at Gregorian under similar conditions.

8 Appendix D. Five-Layer PolyCarb Retarders: NCSP, NLSP, and DL-NIRSP

We procured four optics of 1.5 arc sec diameter as part of the project to develop low beam deflection PC retarders. One ultimately became the upgrade modulator for DL-NIRSP, though these optics were designed for lab use over a wider wavelength range than DL-NIRSP covers. Two of these retarders became upgrades to our NLSP used in our prior works.[46,48] The retarder with the lowest beam deflection at 2.5 arc sec will be used in an upcoming metrology system installed on the DKIST Coudé Laboratory using the full telescope optical path to provide system calibration at wavelengths 380 to 1700 nm. We call this system the NSO Coudé Spectropolarimeter (NCSP).

8.1 *Transmitted Retardance MLO versus NLSP Comparison and Beam Deflection Metrology*

Table 18 shows the four optics fabricated for this effort along with the intended application for each optic. The beam deflection was first measured within a few days of bonding then again after several days and application of edge sealing material. We also show some of the preliminary spatial retardance maps delivered around October 2018 at 525 and 790 nm wavelengths. We note that many more retardance maps on build 4 were done later as well as some spatial variation assessment with NLSP.

We obtained NLSP Mueller matrix spectra for three of these retarders as well as Meadowlark linear retardance spectra. Figure 40 compares the MLO spectral measurements with NLSP Mueller matrix fits. Meadowlark delivered a preliminary 61-point retardance spectra in October 2018 and then reran the metrology with 87 spectral points in November 2018. Solid colored lines show this revised metrology. NSO measured builds 1, 2, and 3 in NLSP

Table 18 MLO TWE and beam deflection for PolyCarb retarders.

Serial no.	Name	Applic.	BDev init	BDev final	Ret maps λ (nm)	Transmitted WFE error, waves at 633 nm
G18125	Build 1	NCSP Mod	2.5	2.11	525	0.080 PV, 0.015 rms, 0.095 pwr
G18126	Build 2	NLSP Refl Mod	8.8	8.16	525, 790	0.153 PV, 0.030 rms, 0.081 pwr
G18127	Build 3	NLSP CalRet	12	9.04	525, 790	0.068 PV, 0.012 rms, 0.038 pwr
G18128	Build 4	DL modulator	4.5	4.70	525 *x*2, 790	0.125 PV, 0.023 rms, 0.032 pwr

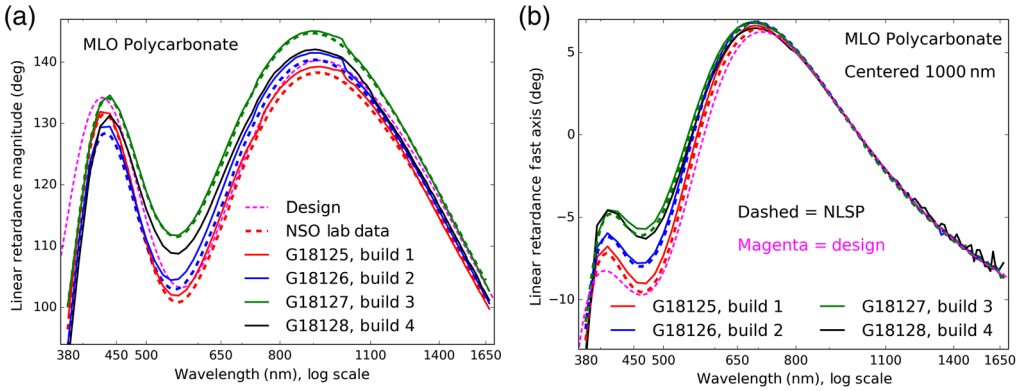

Fig. 40 (a) Linear retardance magnitude and (b) fast axis orientation from the MLO PC retarder builds 1, 2, 3, and 4. The solid lines show MLO data. Wide dashed lines of the same color show NSLP data of the part. We do not have NSLP data on Build 4 G18128, so there is no black dashed line. The theoretical design derived in our Berreman code using PC refractive indices and birefringence is the thick dashed magenta lines. The fast axis orientations were all centered at 0 deg using the 1000-nm wavelength average over a 50-nm bandpass.

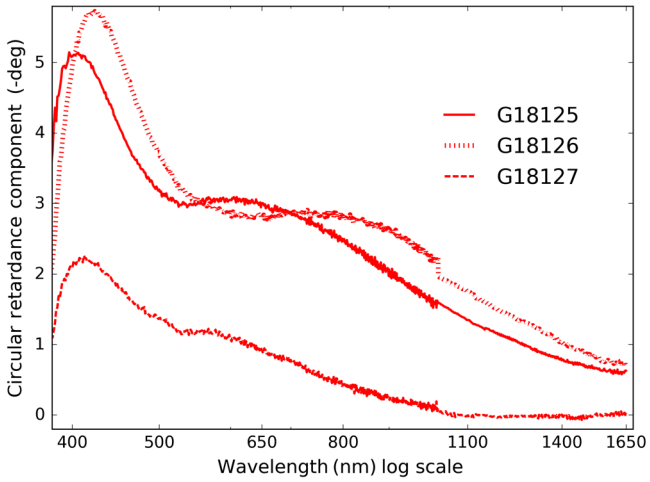

Fig. 41 Circular retardance parameter fits to the NLSP Mueller matrix data sets for PC retarder builds 1, 2, and 3 alone on a 0-deg to 5-deg scale.

giving good agreement between measurements. Build 4 needed special mounting in a cell for use in DL-NIRSP so we do not have an NLSP measurement for this particular optic. We also show the theoretical design as the dashed magenta curve using the nominal PC refractive index and birefringence curves along with the net retardance and orientation for each individual layer.

Figure 41 shows the circular retardance component of the fit to NLSP Mueller matrix measurements. The MLO measurements were made before updating their technique to measure the full ellipse. Subsequent testing showed that NLSP and the new MLO technique agreed to values much smaller than the optic-to-optic variation here. Though these five-layer retarders were designed to be purely linear, manufacturing tolerances always create some mild ellipticity.

8.2 *NLSP Retardance Spectra: Spatial Mapping the PolyCarb NCSP Modulator*

We compile the metrology from NLSP spatial mapping of the NCSP modulator in May 2019. This is a 38-mm-diameter optic with five layers of PC. We used a 2.0–mm-diameter mask attached to the lens tube holding the collimating lens on the collimated beam side. A spatial sampling pattern used a 2-mm radial step and 60-deg angular sampling for the first annulus

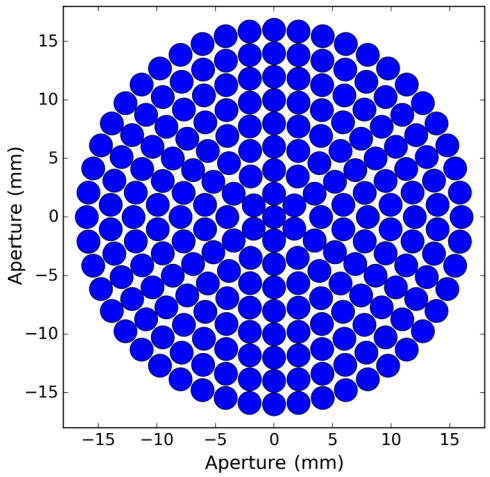

Fig. 42 The aperture sampling with 2-mm beam diameter, 2-mm radial step and 60-deg clocking step on the first ring. The maximum radius was 16 mm.

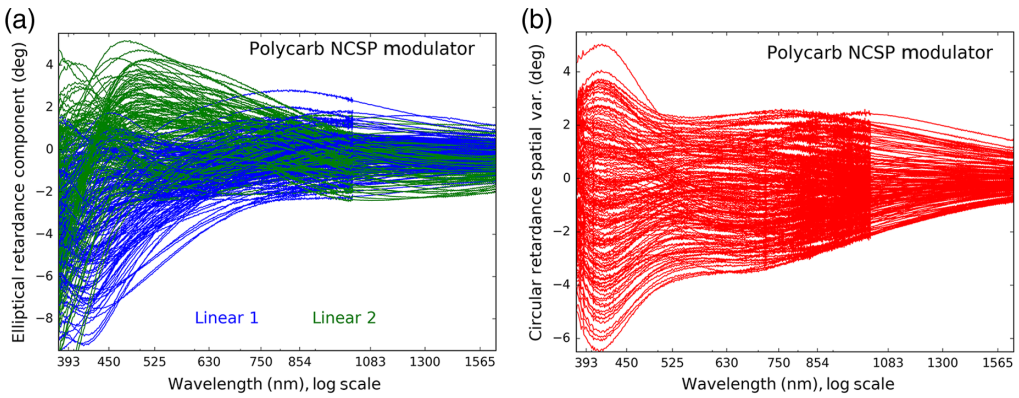

Fig. 43 The spatial variation of elliptical retarder models computed as the difference between the 217 individual measurements across the aperture and the measurement at the center of the spatial pattern. (a) The two linear retardance components in blue and green and (b) circular retardance in red.

decreasing as x^{-1} to the last radius of 16 mm. Figure 42 shows a diagram of the radial sampling pattern covering an aperture of 32-mm diameter measured from footprint center to footprint center. We record 217 individual Mueller matrix spectra across the aperture.

Note that with circular retardance <2 deg and the linear retardance magnitude more than 90 deg there is little difference between elliptical magnitude and linear magnitude. At a wavelength of 393 nm, this PC layer had a measured linear retardance magnitude fit of 262.695 deg and an elliptical magnitude only 0.001 deg higher when the circular component was 0.57 deg. Figure 43 shows the spatial variation of elliptical retarder fit parameters. Note that we have trimmed to 95% aperture for these statistics and residual errors to avoid the edge effects.

Figure 44(b) shows the standard deviation of each retardance fit component at each wavelength across the 217 measurements of the spatial sampling pattern. Figure 44(a) shows P-P spatial variation computed in the same way. This optic shows that circular retardance varies by 10-deg P-P with a standard deviation of 2.0 deg at a 393-nm wavelength. At an 854-nm wavelength, this circular retardance variation falls to 5-deg P-P with a standard deviation of 1.5 deg. We also note that the fast axis of linear retardance, computed as half the inverse tangent of the two linear components, shows much smaller spatial variation. The variation in retardance magnitude is much greater than the variation in the orientation of linear retardance. For instance, the ER magnitude at the 393-nm wavelength varies by 13-deg P-P while the fast axis of linear

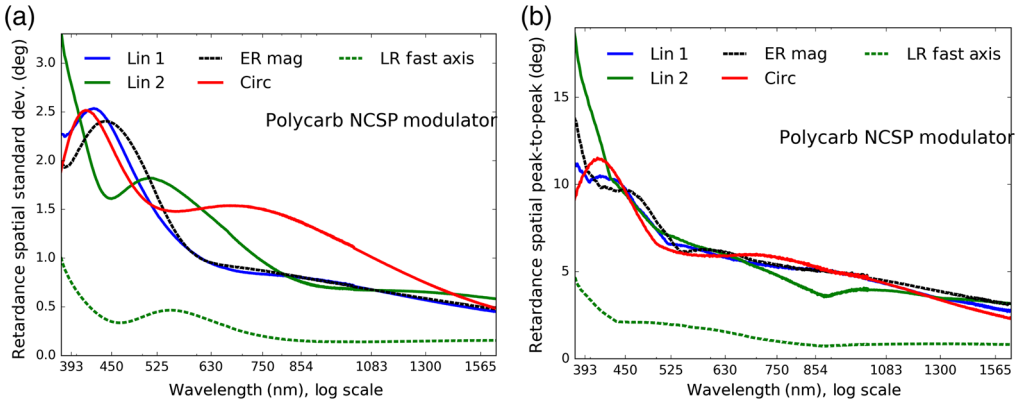

Fig. 44 (a) The standard deviation of the spatial variation of elliptical retarder models. (b) The P-P spatial variation for each component across the aperture is shown. The blue, green, and red curves show the three ER components. Black shows the ER magnitude. Dashed green shows the fast axis of linear retardance. There is roughly a factor of 5 difference between the P-P and standard deviation curves, but with deviations over 50% as a significant function of wavelength.

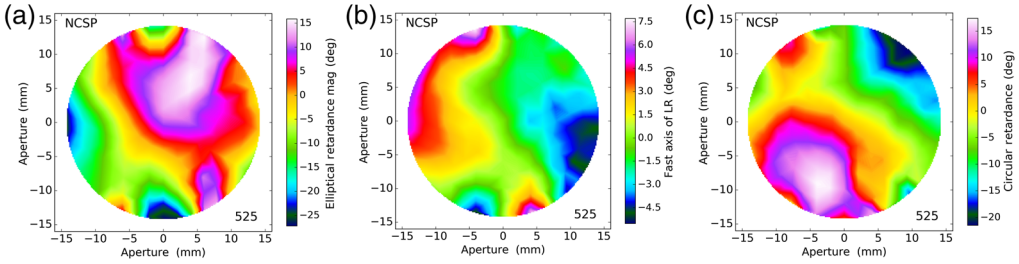

Fig. 45 ER component spatial variation at 525-nm wavelength for the NCSP modulator, part G18125 recorded in May 2019. (a) The ER magnitude, (b) the fast axis of linear retardance, and (c) the circular retardance.

retardance only varies by 4 deg. Note that we have trimmed to 95% aperture for these statistics and residual errors to avoid the edge effects.

The spatial variation has smooth patterns but with different morphologies between the different retardance components. In Fig. 45, we show the spatial maps of ER magnitude in (a), the linear retardance fast axis in (b), and the circular retardance in (c). We note that the spatial form of the variation changes substantially with wavelength. We also note that these parts had a grinding tool used to trim off excess PC outside the glass cover windows likely leading to heating at the aperture edge, causing the stronger variations seen in the outer edge of the aperture. The clear aperture specification for the optic was 80% of the diameter. This area is essentially the entire aperture mapped in Fig. 45.

8.3 *MLO Spatial Mapping of Retardance: Magnitude and Fast Axis at 525 and 789 nm*

All four builds were measured at the 525-nm wavelength. The second, third, and fourth builds were also measured at the 789-nm wavelength. The three builds not shown have very different spatial nonuniformity trends with wavelength and between the elliptical components. However, they mostly have similarly smooth spatial patterns to Figure 45. We compare some of these results here as this represents typical part-to-part manufacturing variability. In Table 19, we compare the statistics of spatial variation at 525 and 790 nm wavelengths for these maps of build 2, build 3, and build 4. The fast axis (FAx) variation was constant with wavelength for two builds, but larger at shorter wavelengths for one build. The standard deviation of the retardance error over the clear aperture is 0.95 deg for build 1, 0.59 deg for build 2, 0.85 deg for build 3, and

Table 19 STDDEV (ret. variation).

525 nm, mag (deg)	790 nm, mag (deg)	525 nm, FAx (deg)	790 nm, FAx (deg)
0.59	1.08	0.76	0.25
0.85	0.79	0.41	0.31
1.194	0.43	0.37	0.29

1.194 deg for build 4. We note that Meadowlark repeated a map of build 4 later and the standard deviation was repeated to better than 0.01 deg as 1.20 deg. The standard deviation of the linear retardance fast axis error over the clear aperture is 0.45 deg for build 1, 0.76 deg for build 2, 0.41 deg for build 3, and 0.370 deg for build 4. We note in a later section that Meadowlark repeated a map of build 4 later and the standard deviation was repeated to better than 0.02 deg orientation as 0.351 deg.

8.4 *NLSP Measurements of DL-NIRSP Polycarb Retardance with Optic Tilt Angle*

We tested for changes in retardance with beam tilt angle measured using NLSP. This range of angles shows the level of expected beam footprint variation in the converging or diverging beams of the ViSP and DL-NIRSP instruments. This aperture variation from a range of incidence angles contributes to the depolarization and loss of modulation efficiency for this kind of optic. The spatial variation of retardance across the aperture will cause more depolarization from the aperture average than the beam angle of incidence (AOI) spread across the aperture for all but the longest DL-NIRSP wavelengths. The two combine to produce a mild loss of modulation efficiency, but both are readily calibrated. We tilt the NCSP upgrade modulator optic by ± 5 deg in steps of 0.5 deg using the nominal 4.5-mm-diameter NLSP beam. We show the tilt angle variation of ER parameters in Fig. 46. The retardance components have been vertically offset for clarity. Black shows the magnitude. Blue and green show the two linear components. Red shows circular retardance. There is significant wavelength variation to the tilt angle sensitivity along this particular tilt axis as expected for multicomponent systems. We note that this tilt angle dependence is also dependent on the clocking as expected for a varying incidence angle. See Ref. 79 for an example on tilt sensitivity of the DKIST six-crystal modulators. This measurement of the NCSP modulator is relevant to the converging beam inside DL-NIRSP as both retarders share the same design and sensitivity. The DL-NIRSP feed optics are at $F/24$ and

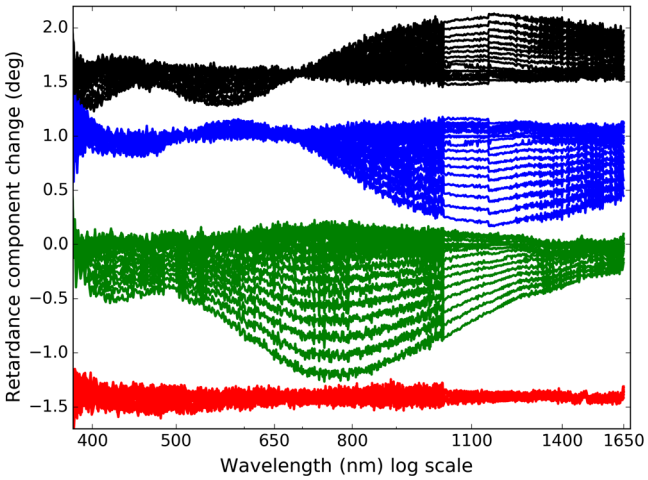

Fig. 46 Change in retardance parameter with beam tilt angle for the NLSP data on build 1 serial number G18125, the NCSP modulator.

62 giving angular spreads of ± 1.2 deg and ± 0.5 deg, respectively. Different wavelengths see up to 1-deg change in a retardance component. We also repeated this test with a 1.5-mm-diameter beam and tilts of ± 2 deg to show that results follow Figure 46 but are scaled down by the lower AOI.

9 Appendix E. DL-NIRSP Polycarb 5-Layer Modulator At *F*/24 and *F*/62

In Table 20, we show the layers included in the DL-NIRSP PC modulator fringe model. The BK7 windows were drawn from an Ohara S-BSL-7 glass formula with very similar refractive index equations. The nominal thickness was 3/16th of an inch, but the actual polished glass blanks were 4.83 mm each. The five individual PC layers were drawn from 75-μm stock. The six adhesive layers were assigned a 13-μm thickness as typical from the Heidenhain gauge measurements for several test optics. The coating is the same the WBBARcq formula of a <20-nm-thick strippable layer followed by 14 oscillating layers of SiO_2 and Ta_2O_5 ending with a thicker MgF_2 outer layer for a 0.74-μm total coating thickness and 16 total layers. The UV cured Summers P92 adhesive is assigned a 13-μm physical thickness, similar to the measured layer thicknesses in the small samples and also the ViSP PC modulator.

Table 21 shows the fringe properties predicted for the DL-NIRSP PC modulator. We compute optical sampling properties assuming a $R = 100$ K sampling FWHM. The top section shows the fringes for the full stack of layers; two windows, five PC layers, and six epoxy layers. The bottom section shows fringes for just a single 4.83-mm-thick BK7 cover window. As an example, at the 854-nm wavelength, this instrument would see the fastest fringe period at 23.9 pm. DL-NIRSP would optically resolve spectral features at 8.5 pm per FWHM giving 2.8 optical profiles per spectral fringe. In the $F/24$ configuration, there would be 3.4 waves of spatial fringes (equal inclination fringes) across a single-beam footprint, reducing the spectral fringe magnitude by roughly one order of magnitude. In the $F/64$ configuration, the marginal ray only sees half a wave of optical path difference, leading to less than a wave of spatial fringe across the footprint

Table 20 DL polyPCM fringe model.

Layer	T (μm)	Desc
Coating	74	WBBAR cq
S-BSL-7	4830	Window
Adhesive	13	Summers P92
PolyCarb1	75	Retarder 1
Adhesive	13	Summers P92
PolyCarb2	75	Retarder 2
Adhesive	13	Summers P92
PolyCarb3	75	Retarder 3
Adhesive	13	Summers P92
PolyCarb4	75	Retarder 4
Adhesive	13	Summers P92
PolyCarb5	75	Retarder 5
Adhesive	13	Summers P92
S-BSL-7	4830	Window
Coating	74	WBBARcq

Table 21 DL-NIRSP fringe properties for sampling and OPD with $F/24$ and 62.

Description	393 nm	486 nm	630 nm	854 nm	1083 nm	1565 nm
FWHM 100 K (pm)	3.93	4.86	6.30	8.54	10.8	15.7
Waves thick full stack	78,959	63,426	48,684	35,779	28,147	19,397
Marg. ray OPD $F/24$	7.3	5.9	4.6	3.4	2.7	1.9
Marg. ray OPD $F/62$	1.1	0.9	0.7	0.5	0.4	0.3
Fringe period full stack (pm)	4.98	7.66	12.94	23.87	38.48	80.68
Optical samples at 100K	1.27	1.58	2.05	2.79	3.55	5.16
Waves thick BK7 window	37,652	30,260	23,233	17,078	13,437	9262
Marg. ray OPD $F/24$	3.5	2.8	2.2	1.6	1.3	0.9
Marg. ray OPD $F/62$	0.5	0.4	0.3	0.2	0.2	0.1
Fringe period for window (pm)	10.44	16.06	27.12	50.01	80.6	168.98
Optical samples at 100 K	2.66	3.30	4.30	5.86	7.44	10.8

and some small reduction of spectral fringe magnitude. At $F/24$, the marginal ray is at 1.19 deg in air, refracting to 0.77 deg in an index = 1.55 medium. At $F/62$, the marginal ray is at 0.46 deg in air, refracting to 0.30 deg in an index = 1.55 medium.

The marginal ray path in the $F/62$ configuration is less than one wave for the nominal DL-NIRSP bandpass of 500 to 1800 nm. There will not be any substantial mitigation of fringe magnitudes in the $F/62$ configuration from a spatial fringe average. However, the new AR coatings will provide some fringe magnitude reduction as this new modulator has anticipated the change in DL-NIRSP wavelengths from the 900- to 2500-nm bandpass of several years ago to the currently anticipated shorter wavelength range.

9.1 *DL-NIRSP Fringes Mitigated with Coatings and Beam* F*/Number*

We combine the impacts of AR coatings reducing fringes as $4R$ for a highly transparent plane parallel window and with the $F/$number per H18.[43] We compare the PC modulator upgrade for DL-NIRSP with the six-crystal super achromat fabricated during the construction project. The six-crystal SAR was presented in H18[43] for fringe thermal instability.

Figure 47(a) shows the predicted fringe magnitude for a collimated beam compared to an $F/24$ beam for a range of interfaces. Both the PC modulator and quartz SAR are overplotted. Solid lines show fringe magnitudes for a collimated beam. Dashed lines show fringe magnitudes scaled by the r^{-2} spatial fringe average we approximated (see H18[43]). Figure 47(b) shows the fringe reduction factors in an $F/24$ beam for 10.1 mm of BK7, 12.8 mm of crystal quartz, and 2.1 mm of crystal quartz. Note that the dashed blue line represents the anticipated fringe magnitude for the PC retarder. This should be compared with the dashed green line anticipated as the limiting fringe magnitude for the quartz crystal modulator representing the air facing crystal to oil reflection. The fringe magnitude reduction is over 20× at short wavelengths, but with less substantial gains for longer wavelengths.

For the $F/62$ configuration, we will ignore any spatial fringe averaging and compare the collimated beam cases. The solid red curve representing the coated crystal interface to air through the full stack has fringe magnitudes up to 18% at visible wavelengths due to the coating central wavelength at 1300 nm. Similarly, single crystal magnitudes of the solid green curve are up to 7% for a coated crystal with air on one side and oil on the other side. The solid blue line of the PC modulator is always in the 2% to 8% range under these same circumstances.

In Table 22, we compile values for some fringe magnitudes and $F/$number fringe reduction properties. The first column shows the interfaces between air or oil and the optical elements of

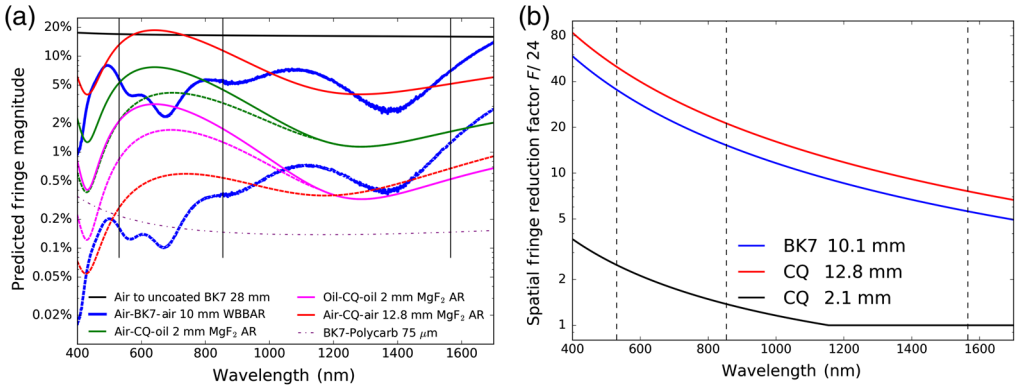

Fig. 47 (a) Fringe magnitudes predicted from coating reflectivity measurements from IOI combined with the marginal ray path estimates per H18.[43] BK7 samples were used at an incidence angle of 8 deg in reflection. (b) The spectral fringe reduction factor derived with the r^{-2} scaling envelope for the spatial fringe average from H18.[43] Blue shows 10.1 mm of BK7, the full thickness of the PC modulator. Red shows 12.8 mm of crystal quartz, the nominal six-crystal modulator thickness. Black shows 2.1 mm of crystal quartz, the thickness of an individual crystal within the modulator. Vertical dashed black lines show common observing wavelengths of 530, 854, and 1565 nm.

Table 22 DL fringe magnitude: collimated versus $F/24$.

Optical interfaces	λ	Col	$F/24$	Fact.
Enter–optic–exit	nm	%	%	
Air–10-mm BK7c–air	530	5.68	0.16	35
Air–10-mm BK7c–air	854	5.63	0.37	15
BK7–PolyCarb–BK7	530	0.35	0.35	–
BK7–PolyCarb–BK7	854	0.15	0.15	–
Air–12-mm CQc–air	530	13.25	0.27	50
Air–12-mm CQc–air	854	11.41	0.54	21
Air–2-mm CQc–oil	530	5.30	2.13	2.5
Air–2-mm CQc–oil	854	4.46	3.24	1.3
Oil–2-mm CQc–oil	530	2.12	0.85	2.5
Oil–2-mm CQc–oil	854	1.74	1.27	1.3

BK7, crystal quartz with a simple AR coating (CQc) or the bare PC. As an approximation for this table, we ignore the simultaneous solution of all coherent reflections following the Berreman calculus and simply approximate each layer as if it was alone and free standing. For instance, oil–2-mm CQc–oil would be the fringe magnitude for an AR coated quartz crystal immersed in $n = 1.3$ oil. The second column shows the wavelength for each row. The third column shows the fringe magnitude for the collimated beam (Col) for comparison with solid lines in Fig. 47(a). The fourth column shows the peak fringe magnitude predicted with the r^{-2} envelope scaling to $F/24$. The fifth column shows the fringe reduction factor for that particular wavelength and $F/$number for the particular optic producing individual fringes.

The black curve of Fig. 47 shows the fringe magnitudes of 16% to 18% for an uncoated a BK7 window in air with a collimated beam. As measured in the lab, fringe magnitudes in

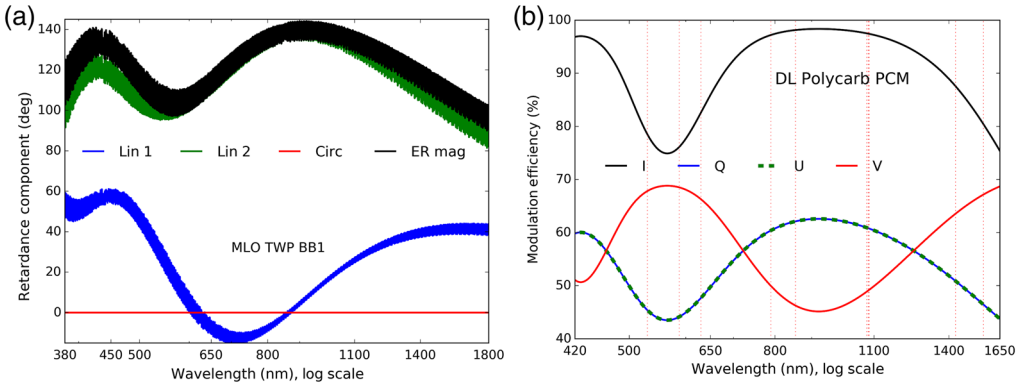

Fig. 48 (a) Retardance fringes for the uncoated DL-NIRSP PC modulator for a collimated beam. Blue, green, and red show the three ER components. Black shows the magnitude of ER. (b) Modulation efficiency for an eight-state sequence with evenly spaced steps through 180-deg rotation. The *Q* and *U* efficiencies are identical.

transmission windows are well approximated by $4\sqrt{R_1}\sqrt{R_2}$. The blue curve shows our AR-coated BK7 window fringes at few percent magnitudes when in a collimated beam. The dashed blue line shows additional impact of the 10.1-mm-thick windows in an $F/24$ beam reducing this fringe magnitude by factors of 5× to over 80× at the shorter wavelengths.

Red shows the fringe magnitude corresponding to the air to crystal quartz interface where the quartz is coated with a single 233.8-nm-thick isotropic MgF_2 AR coating. This corresponds to a quarter wave at the 1300-nm central wavelength and gives rise to the coating reflectivity minimum. The air–quartz–air interface represents the full 12.8-mm thickness of the entire six-crystal retarder stack. Green shows a single 2.1-mm-thick crystal quartz retarder, but with an interface to the oil at refractive index roughly 1.3 used in the assembly of the six-crystal modulator. The first and last crystals are modeled as air to coated crystal to oil. Magenta in Fig. 47(a) shows this same AR-coated crystal quartz but now immersed in oil representing the interior crystals in the stack. The single dot-dashed magenta line shows the internal interface between PC and BK7. As the individual adhesive layers are 13-μm thick and the PC is only 75-μm thick, there is no change in the $F/24$ beam.

Figure 48 shows the elliptical retarder model fit to the Berreman fringed Mueller matrix modeled without BBAR coatings assuming all surfaces are perfectly flat and parallel. Figure 48(b) shows the modulation efficiency of the design without fringes.

9.2 *Additional Spatial Mapping of the DL-NIRSP Modulator*

Spatial behavior of the PC DL-NIRSP modulator is important for deriving expected modulation matrix efficiency loss as a function of optical configuration. Figure 49 shows the individual field

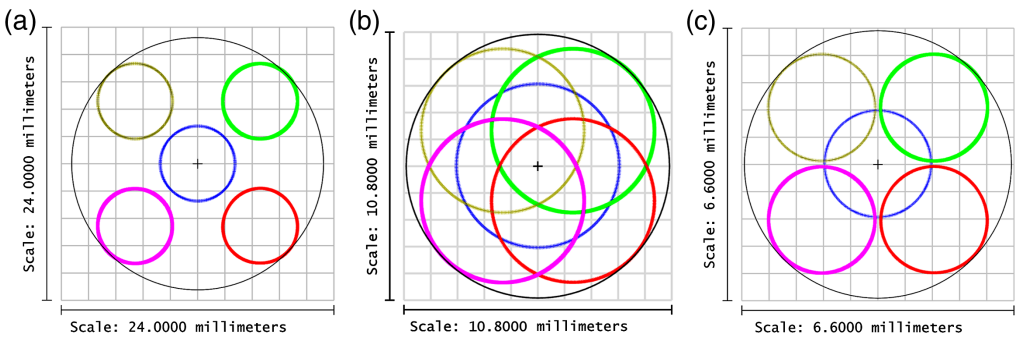

Fig. 49 Footprints for the beam center and points at the field edge on the DL-NIRSP modulator entrance surface with the beam converging toward exit: (a) $F/8$, (b) $F/24$, and (c) $F/62$.

Table 23 MLO new spatial map wavelengths (nm).

392	420	531	588	630	787	851	931	1066	1565

angle beam footprints on the PC optic for the three anticipated optical modes. The beam is either $F/24$ or $F/62$ when propagating through this optic, but with the coronal lens, the footprint is extended as the beam on the imaging fiber array becomes $F/8$ covering a wider field. The beam footprints are quite different between modes. The $F/8$ configuration covers 27.8×18.6 arc sec with a 24-mm clear aperture. The $F/24$ mode covers 6.2×4.6 arc sec with a 10.8-mm clear aperture. $F/62$ at right covers 2.4×1.8 arc sec with a 6.6-mm clear aperture. The individual field point footprint is the same 6.7-mm diameter in both $F/8$ and $F/24$ modes though the coronal lens separates those footprints significantly. At $F/62$, the individual field footprint is 2.6 mm.

Meadowlark remapped build 4 over the new extended wavelength range. Table 23 shows the new extended wavelength range used for the additional metrology and the new fast axis determination technique. Meadowlark expanded the range of available mapping wavelengths to include testing at 392 and 1565 nm. Meadowlark also changed techniques to use double the machine time (a few hours per wavelength on this optic) to possibly reduce issues with fast axis orientation. Figures 50 and 51 show example spatial retardance and fast axis orientation maps of build 4, the DL-NIRSP modulator upgrade at these new wavelengths.

The Meadowlark spatial mapping procedure was repeatable. A systematic difference of 0.3-deg retardance magnitude and 0.14-deg fast axis orientation was present between the two maps repeated at the 630-nm wavelength. The spatial variation seen in the maps was also repeatable to 0.2-deg magnitudes and better than 0.1 deg in fast axis across those repeated maps. After adopting the new fast axis measurement technique, the 630-nm map was repeated 3 times and the 931-nm map was repeated twice. Similar results were obtained at other wavelengths. The spatial variability of elliptical magnitude between the two procedures did not change significantly, but the fast axis orientation errors did improve.

There is good agreement between both spectral and spatial measurement systems at MLO. Figure 52(b) shows the elliptical retardance magnitude measured with both the spectrograph systems with an overlay of the spatial map averages as the symbols. The blue and green dots show repeatability between spatial maps, and the blue line is the spectral scan agreeing with all spatial maps. Because the behavior in a small beam footprint at the center of the optic is

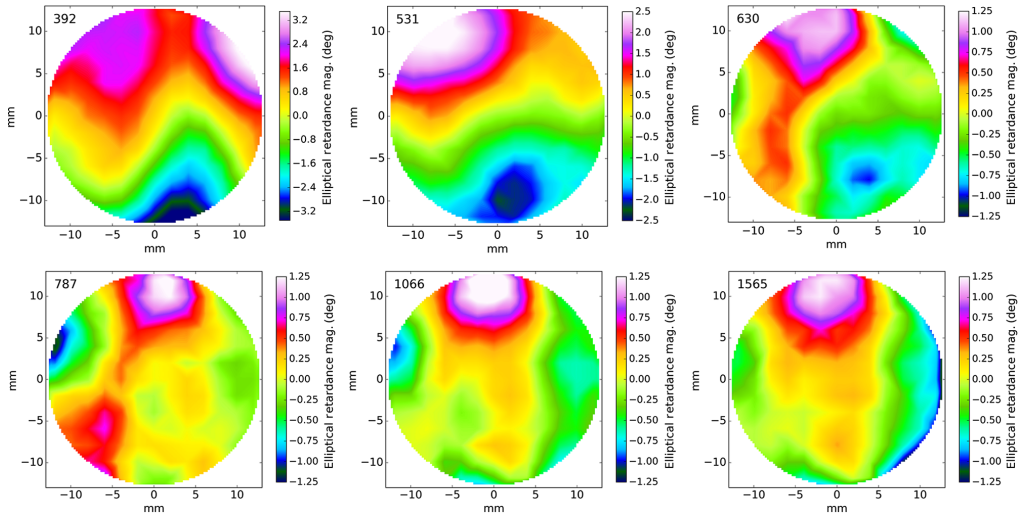

Fig. 50 Spatial variation of ER magnitude for the DL-NIRSP PC modulator part G18128. The new fast axis mapping technique was used for this January 2019 data set.

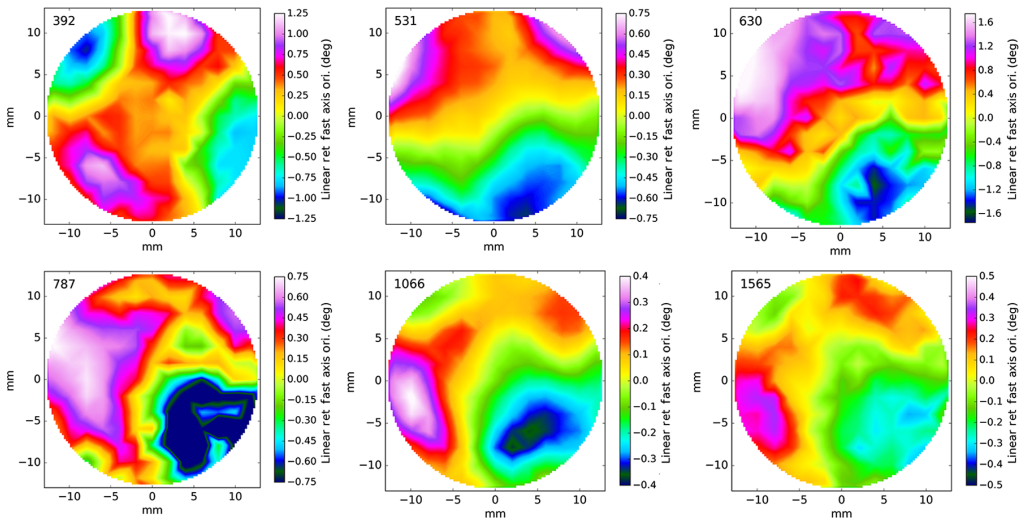

Fig. 51 Spatial variation of linear retardance fast axis for the DL-NIRSP PC modulator part G18128. The new fast axis mapping technique was used for this January 2019 data set.

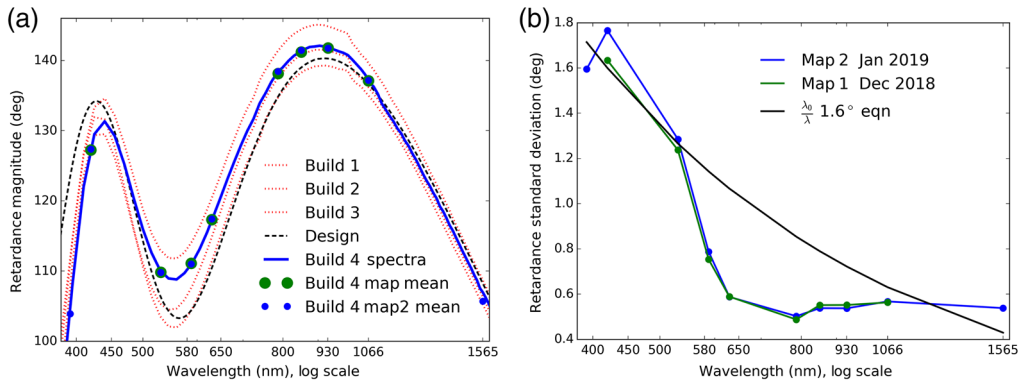

Fig. 52 (a) The spectral measurements of retardance for all four builds. The blue line shows build 4. The blue dots show the mean of the retardance spatial maps with very good agreement between systems. The theoretical model is shown as the dashed magenta line. (b) The spatial variance of retardance across the aperture as a function of wavelength. The blue line and symbols show the data for each map. Black shows a simple λ^{-1} curve scaled to 1.6 deg at 420-nm wavelength.

not expected to be identical to the average over the entire clear aperture, the slight offsets for some points is expected and is significantly above the system noise limits. We show the spectra of the other three builds as thin red lines for reference. Figure 52(a) shows the standard deviation of retardance spatial variation. The black line shows a λ^{-1} trend with significant repeatable departure from this trend.

The fast axis data set was somewhat less repeatable with 2-deg changes between data sets at three wavelengths attributed to room light contamination in the MLO labs. We compared the repeated spatial map averages as the blue and green dots. The blue solid line shows the MLO spectral system data. The repeatability is quite good outside these three wavelengths, as is the agreement with the MLO spectral systems. Figure 53 shows the linear retardance fast axis measured with both the spectrograph system with an overlay of the spatial map averages as the symbols. There is good agreement between both spectral and spatial measurement systems. Figure 53(b) shows the standard deviation of the fast axis spatial variation. The new fast axis computation technique did lower the spatial standard deviation by 0.15 deg compared to the spatial variation magnitudes of over ± 1.5 deg in some cases of Fig. 51. There is no obvious λ^{-1} trend for the fast axis spectral variation.

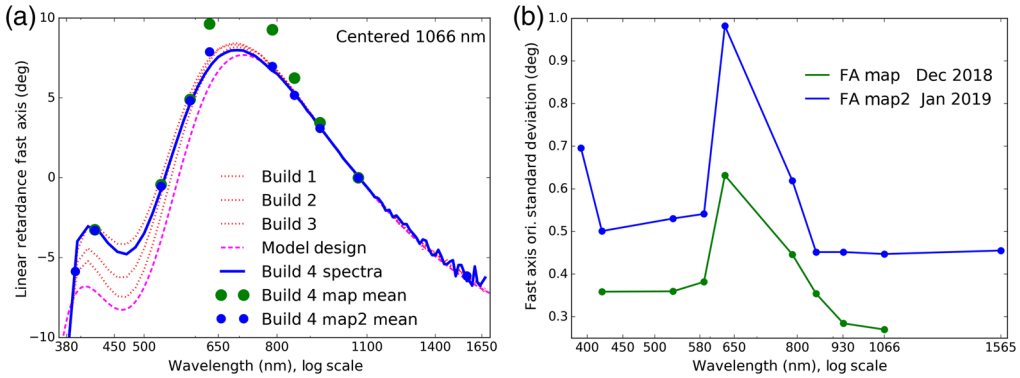

Fig. 53 (a) The spectral measurements of fast axis for all four builds. The blue line shows build 4. The blue dots show the mean of the fast axis spatial maps with agreement between systems. The theoretical model is shown as the dashed magenta line. (b) The spatial variance of fast axis across the aperture as a function of wavelength. The blue line and symbols show the data for each map.

10 Appendix F. Cryo-NIRSP: Six MgF_2 Crystal Modulator at *F*/18

In Table 24, we show the nominal design properties for the six-crystal super achromat. At 633-nm wavelengths, the A–B–A superachromat design is 1.89 waves at 0 deg then 1.29 waves at 71.9 deg ending with 1.89 waves at 30.4 deg. The five oil layers are estimated at 10-μm physical thickness though lab tests between small windows have given possible thickness ranges between 5 and 20 μm as in H18a.[43] We note that we have published the as-built net retardance of each crystal pair in subtraction in H18[43] with the crystal thickness being within a few 10s of microns of the nominal design. We combine the impacts of AR coatings reducing fringes as $4R$ for a highly transparent plane parallel window and with the $F/$number per H18.[43] Figure 54 shows the predicted fringe magnitude using the refractive index equations for a collimated beam compared to an $F/18$ beam for a range of interfaces. Solid lines show fringe magnitudes for a collimated beam. Dashed lines show fringe magnitudes scaled by the r^{-2} spatial fringe average for the nominal thickness of each particular optic (see H18[43]). Vertical dashed black lines show common observing wavelengths of 854 and 1430 nm.

Table 25 shows the fringe properties predicted for the Cryo-NIRSP six MgF_2 crystal super achromatic modulator. We compute optical sampling properties assuming an $R = 100$ K

Table 24 CN MgF_2 PCM.

Layer	T (μm)	Note
MgF_2 1	2155.0	0 deg
Oil	10.0	$n \sim 1.3$
MgF_2 2	2153.1	90 deg
Oil	10.0	$n \sim 1.3$
MgF_2 3	2222.1	71.86 deg
Oil	10.0	$n \sim 1.3$
MgF_2 4	2153.1	161.86 deg
Oil	10.0	$n \sim 1.3$
MgF_2 5	2255.0	30.39 deg
Oil	10.0	$n \sim 1.3$
MgF_2 6	2153.1	120.39 deg

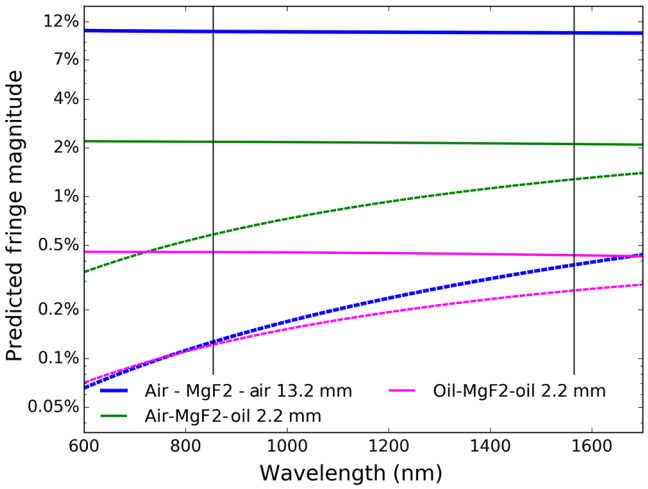

Fig. 54 Fringe magnitudes as solid lines with the marginal ray path r^{-2} scaling estimates per H18[43] applied as dashed lines. Blue shows uncoated 13.2-mm crystal MgF_2. Green shows 2.2 mm of crystal MgF_2 with one side exposed to air, the other to oil. Magenta shows a 2.2-mm crystal MgF_2 immersed completely in oil.

Table 25 Cryo-NIRSP modulator fringes $F/18$.

Description	854 nm	1430 nm
FWHM 100k (pm)	8.54	14.3
Waves thick 13.2 mm stack	42,776	25,491
Marg. ray OPD $F/18$	8.6	5.1
Fringe period stack (pm)	19.9	56.1
Optical samples at 100K	2.3	3.9
Waves thick 2.2-mm MgF_2	7134	4251
Marg. ray OPD $F/18$	1.4	0.9
Fringe period 2.2 mm (pm)	119.6	336.1
Optical samples at 100 K	14.0	23.5

sampling FWHM. The top section shows the fringes for the full stack of six crystals totaling 13.2-mm thickness, the nominal six-crystal modulator thickness. The bottom section shows fringes for just a single 2.2-mm-thick MgF_2 crystal, the average thickness of an individual crystal within the modulator. As an example, at an 854-nm wavelength, this instrument would see the fastest fringe period at 19.9 pm. Cryo-NIRSP would optically resolve spectral features at 8.54 pm per FWHM giving 2.3 optical profiles per spectral fringe period. In the $F/18$ configuration, there would be 8.6 waves of spatial fringes (equal inclination fringes) across a single-beam footprint, reducing the spectral fringe magnitude by roughly a factor of 80×. The air-to-crystal interface for the exterior 2.2-mm-thick MgF_2 crystals would produce a fringe period at 119.6 pm sampled by 14 optical FWHM profiles. With 1.4 waves optical path difference between marginal and chief rays, we estimate a 3.7× reduction in fringe magnitude using the simple r^{-2} envelope.

In Table 26, we illustrate some fringe properties for wavelengths of 854 and 1430 nm. The first column shows the interfaces between air or oil and the optical elements in the six MgF_2 crystal modulator with uncoated surfaces. We ignore the simultaneous solution of all coherent reflections following the Berreman calculus. We simply approximate each layer as if it was alone

Table 26 Fringe magnitude collimated versus $F/18$.

Optical interfaces	λ	Col	$F/18$	Fact.
Enter–optic–exit	nm	%	%	
Air–13-mm MgF_2–air	854	10.48	0.13	83
Air–13-mm MgF_2–air	1430	10.32	0.32	32
Air–2-mm MgF_2–oil	854	2.18	0.59	3.7
Air–2-mm MgF_2–oil	1430	2.13	1.16	1.8
Oil–2-mm MgF_2–oil	854	0.46	0.12	3.7
Oil–2-mm MgF_2–oil	1430	0.44	0.24	1.9

and free standing. For instance, oil–2-mm MgF_2–oil would be the fringe magnitude for an uncoated MgF_2 crystal at 2.2-mm thickness immersed in $n = 1.3$ oil. The second column shows the wavelength for each row. The third column shows the fringe magnitude for the collimated beam (Col) for comparison with solid lines in Fig. 54(a). The fourth column shows the peak fringe magnitude predicted with the r^{-2} envelope scaling to $F/18$. The fifth column shows the fringe reduction factor for that particular wavelength and $F/$number for the particular optic producing individual fringes.

10.1 *NLSP Spatial Mapping of the Cryo-NIRSP Modulator over 78-mm Aperture*

We compiled the metrology from NLSP spatial mapping of the Cryo-NIRSP six-crystal modulator in June 2019. This is a 105-mm-diameter optic clear aperture. We used a 2.0-mm-diameter mask attached to the lens tube holding the collimating lens on the collimated beam side. A spatial sampling pattern used a 3-mm radial step and 60-deg angular sampling for the first annulus decreasing as x^{-1} to the last radius of 39 mm. We record 547 individual Mueller matrix spectra across the aperture. We compiled the metrology performed and fit ER models.

Figure 55(a) shows a retardance model fit to the aperture-center NLSP data set. The elliptical parameters are driven through zero at the 790-nm wavelength. We anticipate that the retarder is actually 1 wave net magnitude at this wavelength. However, the Mueller matrix residuals and other derived spatial quantities are identical for this retarder model without exacerbating the retardance spatial variation statistics. In Fig. 55(b), we show the modulation efficiency.

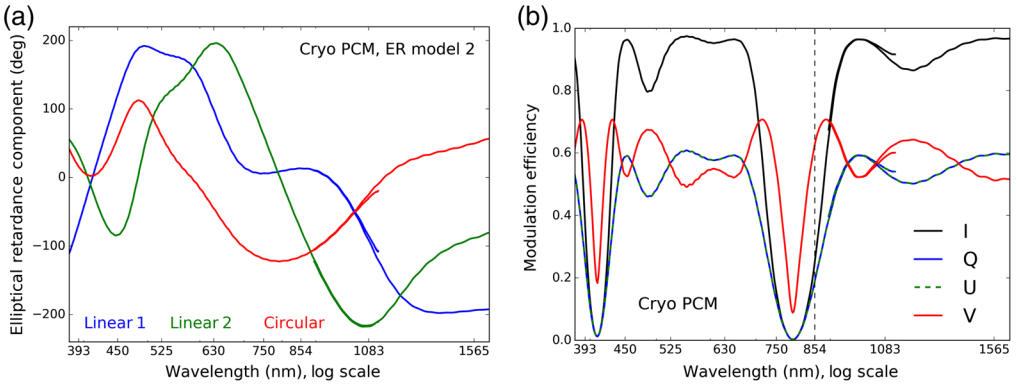

Fig. 55 (a) The elliptical retarder model fit to aperture center. Different colors show the three elliptical retarder components. Note we use a model that forces net zero retardance at short wavelengths. (b) The modulation efficiency for this optic using an eight-state discrete uniform sequence. 854-nm wavelength is shown as the vertical dashed black line.

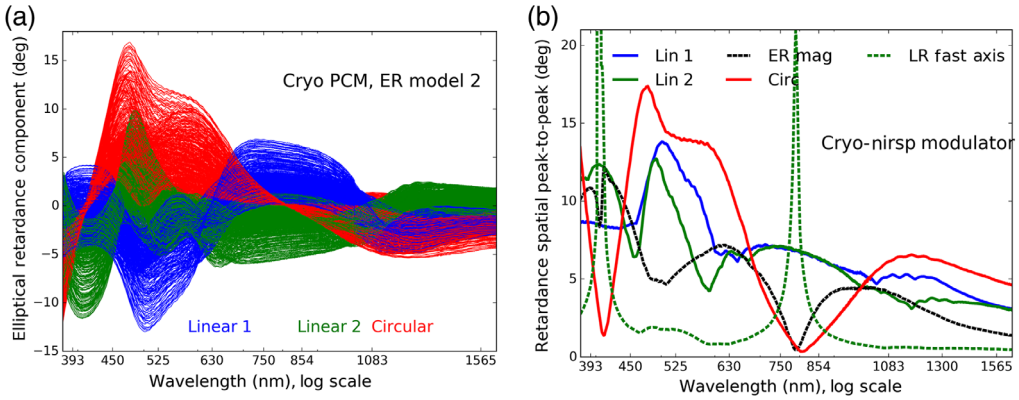

Fig. 56 The NLSP retardance spectra difference from the aperture center. Blue and green show the two axis-angle linear retardance components. Red shows circular retardance. The standard deviation of the spatial variation of ER parameters over the 78-mm aperture is at right. Note that the linear retardance magnitude goes to 0 and 1 at 790 and 400 nm. This makes the fast axis ill defined, increasing the spatial variation statistic. We note that the two linear curves show smooth spectral behavior in spatial variation.

The design bandpass was for wavelengths between 1 and 5 μm so there are gaps in efficiency at shorter wavelengths with nonzero efficiency at the 854-nm wavelength shown as the dashed black vertical line. The Cryo-NIRSP has since added an 854-nm wavelength filter and can expand to other wavelengths in the future.

The NLSP spatial uniformity measurements show a complex spectral pattern. Figure 56(a) shows the difference between aperture center and any individual spatial location. Figure 56(b)

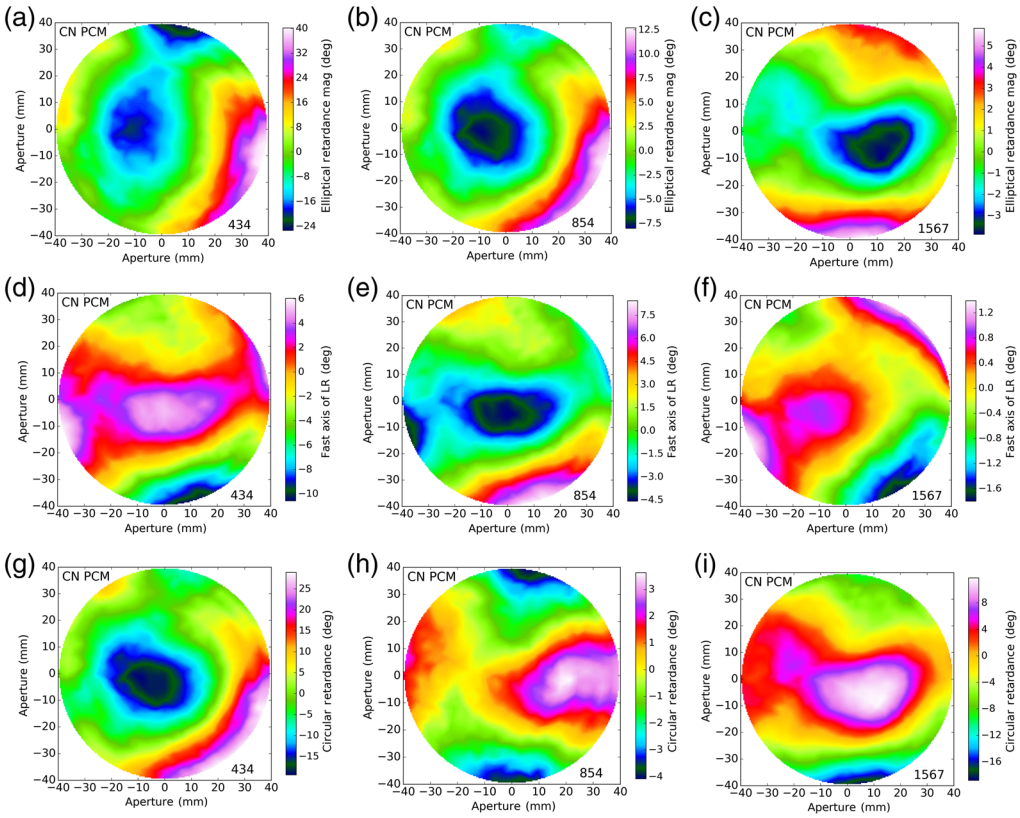

Fig. 57 ER spatial variation for the Cryo-NIRSP modulator measured by NLSP in June 2019: (a), (d), (g) 434 nm; (b), (e), (h) 854 nm; and (c), (f), (i) 1567 nm. (a)–(c) Elliptical magnitude, (d)–(f) fast axis of linear retardance, and (g)–(i) circular retardance.

shows the standard deviation of each retardance fit component at each wavelength across the 547 measurements of the spatial sampling pattern. Red shows circular retardance, whereas blue and green show the two linear components. We can see that the circular retardance variation is somewhat anticorrelated with the linear retardance components. At integer multiples of half-wave and full-wave, the fast axis variation shown as the dashed green curve gets exacerbated by noise. The linear component variation stays at roughly constant magnitudes. Figure 57 shows the spatial maps of ER magnitude, fast axis, and circular retardance at three wavelengths. The spatial variation has changing patterns with wavelength seen as the left to right variation in each row. The color scaling shows the decreasing retardance component magnitudes at longer wavelengths.

11 Appendix G. Clocking Oscillations in SiO_2 and MgF_2 Retarders

Misalignments in orientation between layers in many layer retarders cause spectral oscillations in retardance. For multiorder retarders, especially thick compound retarders, these oscillations can be many degrees.

The clocking oscillation period can be estimated for a retarder using the physical thickness (d) and the difference between extraordinary and ordinary beam refractive indices (n_e and n_o), which is called the birefringence ($b = n_e - n_o$). To compute the clocking oscillation period, we solve for the wavelength interval ($\lambda_1 - \lambda_2$) required to change the optical path difference between the extraordinary and ordinary beams of exactly one wave in the following equation:

$$\frac{2d(n_e - n_o)}{\lambda_2} - \frac{2d(n_e - n_o)}{\lambda_1} = \frac{2db(\lambda_1 - \lambda_2)}{\lambda_1\lambda_2} \sim 1. \tag{9}$$

For retarders with many waves of retardance per crystal, we can approximate λ_1 and λ_2 as about the same. For typical retarder crystals at visible wavelengths, the optic is at least millimeters thick with tens of waves net retardance. With this approximation, we can simplify Eq. (9) to get a simple formula for the clocking oscillation period in wavelengths ($\delta\lambda$) expressed as the wavelength squared (λ^2) divided by the optical path difference for the beam ($2db$). As an example, consider a 2-mm-thick crystal quartz window with a refractive index of 1.553 for the extraordinary beam and 1.544 for the ordinary beam observed at the 500-nm wavelength. We compute a clocking oscillation period of 6.94 nm with birefringence of $b = 0.009$. Since the difference between wavelengths λ_1 and λ_2 is one part in 70, the assumption of $\lambda_1 \sim \lambda_2$ produces a period estimate better than 2%

$$\lambda_1 - \lambda_2 = \delta\lambda = \frac{\lambda_1\lambda_2}{2db} \sim \frac{\lambda^2}{2db}. \tag{10}$$

We show here examples of six-crystal retarder models to illustrate the magnitude of these misalignments in the DKIST six crystal retarders. Note that we used the CCD system in NLSP that had optical profiles of 1.2-nm spectral width so we do not resolve clocking oscillations well at short wavelengths compared to the 0.3 nm profiles of our new EVO CMOS spectrograph described in Appendix C.2

The SiO_2 VISP SAR described above in Sec. 3.3, Table 8, and detailed in HS18b[46] has measured spectral oscillations over 1 deg in retardance component magnitudes. The individual crystals had ~30 waves net retardance bias at a 633-nm wavelength with less than half a wave retardance difference polished between the compound pairs as in Table 4. Figure 58 shows retardance fits to our NLSP lab metrology data and an example theoretical model perturbed for manufacturing errors. We rotate the NLSP data set by −7.25 deg to match the orientation of the theoretical perturbed model over the NLSP bandpass. We then apply a clocking perturbation to simulate our estimated manufacturing errors. The perturbations applied to the six crystals are: crystal 2 + 0.3 deg clocking, crystals 2, 3, 5, 6 + 0.698 μm, 0.01 waves, 3.6 deg at 633 nm.

Figure 58(a) shows the measured data as dashed lines while the perturbed model is solid lines. Figure 58(b) highlights the circular retardance component showing how polishing and clocking errors both combine to create net ER and also clocking oscillations at magnitudes of at least 1 deg. Note that the spectral resolving power of the NLSP data set is insufficient

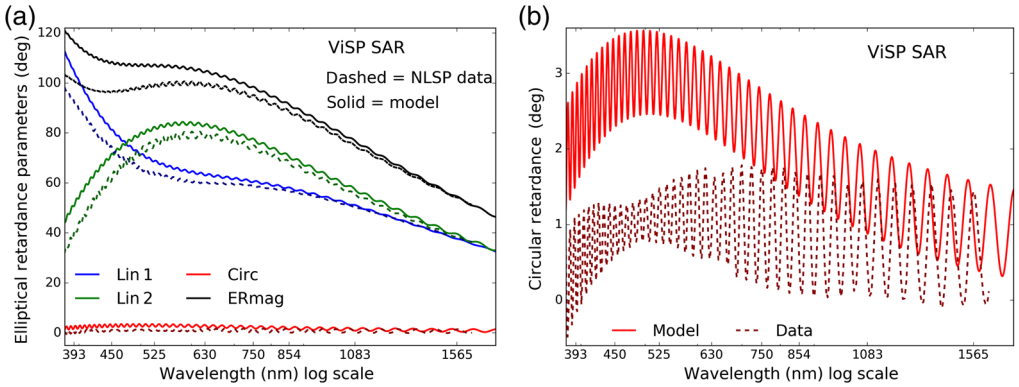

Fig. 58 (a) Perturbations to the elliptical retarder model. The second crystal was offset by 0.3 deg. Crystals 3 and 5 were thickened by 0.5 μm. The differences in ER parameters show both spectral oscillations and magnitude changes. (b) The circular retardance from this model as a solid curve to the measured circular retardance in the dashed curve with NLSP.

to fully resolve the clocking oscillations at shorter wavelengths leading to a reduced magnitude detected in the data set. In our prior publication (Fig. 27 of HS18b[46]), we had even lower spectral resolving power set for NLSP and did not resolve the oscillations at all for wavelengths shorter than 550 nm. Note that we did not have spatial retardance maps nor retardance spectra of the individual compound retarders in the A–B–A style super achromatic design. We do not currently have enough information to provide for six thickness errors and six alignment errors to exactly match the retardance curves.

The Cryo-NIRSP MgF_2 SAR had similar oscillations with larger magnitudes at shorter wavelengths. The individual crystals had ~40 waves net retardance bias at the 633-nm wavelength with more than 2 and 3 waves net retardance difference polished between the compound pairs as in Table 4. We show that the thermal sensitivity of the spectral clocking oscillations is of similar magnitude for the expected 20-deg ambient temperature swings. We use the example of NLSP data on the Cryo-NIRSP calibration retarder. We recorded NLSP Mueller matrix spectra of this optic before deployment at the telescope. ER parameters are fit to the Mueller matrix. We rotate the Cryo-NIRSP SAR NLSP data by 133.75 deg to match the theoretical six-crystal model with an average angle derived over the NLSP bandpass. We then apply clocking and polishing errors consistent with the manufacturing tolerances. Figure 59 shows the NLSP data and the six-crystal theoretical model for the CN SAR after perturbation in (a). Figure 59(b) highlights circular retardance. The perturbations applied to the six crystals are crystal 2 + 0.3 deg clocking, crystals 3, 5 + 0.538 μm, 0.01 waves, 3.6 deg at 633 nm.

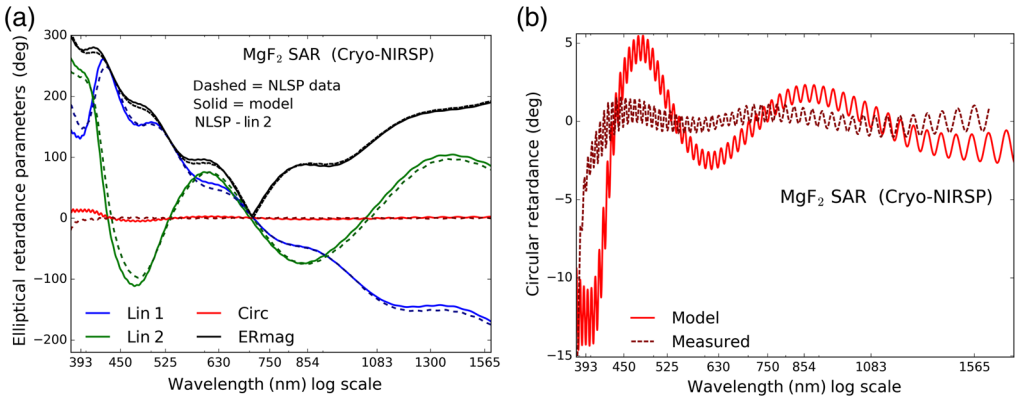

Fig. 59 (a) Perturbations to the elliptical retarder model. The second crystal was offset by 0.3 deg. Crystals 3 and 5 were thickened by 0.5 μm. The differences in ER parameters show both spectral oscillations and magnitude changes. (b) The circular retardance from this model as a solid curve to the measured circular retardance in the dashed curve with NLSP.

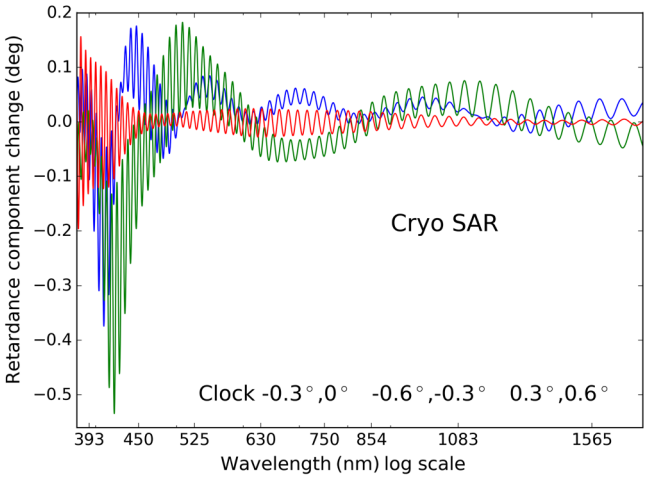

Fig. 60 Thermal change of the ER parameters for a clocking error scenario. We use a ±0.6- deg *y* scale and a temperature change of 1°C. Five of the six crystals are perturbed to produce clocking errors of magnitude 0.3 deg in each compound pair and then each crystal stack is thermally perturbed then differenced.

The thermal sensitivity of this MgF_2 six-crystal retarder is similar to the SiO_2 retarders. Figure 60 shows the thermal drift of clocking oscillations for the Cryo-NIRSP SAR model. The anticipated temperature change within a few minutes of illumination for this optic is significantly <0.5°C when the polarizer is used ahead of this optic during calibration. Given the higher net retardance of the compound crystal pairs, the design differences and spectral clocking oscillations are larger and also spectrally faster. For high-spectral resolving power instruments, there is a strong need to minimize these clocking spectral oscillations through tight manufacturing tolerances.

12 Appendix H. VTF Ferroelectric Liquid Crystal Modulator

The VTF instrument will be delivered and integrated with DKIST in the coming years. This instrument will be calibrated with the retarders described in this paper. The polarization fringes from the VTF modulator and DKIST calibration retarder need to be assessed. We note that we worked with MLO to characterize the spatial retardance variation of the VTF modulator in HS18.[46] VTF has a modulator designed with liquid crystals and a fringe mitigation strategy deploying wedged windows on entrance and exit. The wedge removes fringes from the air-facing surfaces, but will not mitigate fringes between internal plane-parallel interfaces. Given the optical location, greatly reduced UV flux, greatly reduced heat loads, and availability of liquid crystal retarders covering a much smaller wavelength bandpass, this type of modulator can substantially suppress fringes. However, fringes internal to the stack of layers are still anticipated but at very low amplitudes. We include this optic here for completeness and for comparison of design strategy.

The nominal VTF design is to use two FLC retarders along with two zero-order PC retarders (PolyCarb) from MLO. Table 27 shows the orientation and retardance for the as-built four-retarder achromatic modulator measured by the VTF team. The first column shows the material, either an FLC or a PC retarder. The second column shows the orientation of the fast axis in degrees. The third column shows the nominal design retardance in waves at the 650-nm wavelength. We outline the wavelength dependence below. These materials have very different spatial characteristics. The clear aperture is 60 mm with the optic illuminated by a diverging $F/40$ beam. The optic is close to the $F/40$ focus with a single-field point having a footprint of 4.4- to 5.1-mm diameter on the polarization components internal to this modulator. Spatial nonuniformity can be expected at some small amplitude for the PC parts similar to the maps shown above in Figs. 7 and 8 as well as in HS18b.[46] The Meadowlark FLC material is reasonably well oriented at zero voltage, though this material has shown retardance and fast axis switching angle

Table 27 VTF modulator.

Material	θ (deg)	ϕ (waves)
FLC	–7.1	0.4720
PolyCarb	–79.9	0.2235
FLC	47.3	0.4570
PolyCarb	–20.2	0.2935

that depend mildly on the voltage applied. Measured spatial retardance variation for one of the two VTF FLCs was shown Fig. 51 in Appendix C of HS18b[46] for a few wavelengths. When this instrument is integrated with DKIST, the fringes, spatial variation of retardance, thermal stability of our Coudé Laboratory, and field angle-dependent mirror calibration errors will all combine to limit the VTF delivered polarization accuracy

$$n = 1.447193 + \frac{383343.3}{\lambda^2} + \frac{5.661342e11}{\lambda^4}. \tag{11}$$

The VTF team uses a Cargille fused silica matching liquid with code 06350. The refractive index is computed with Eq. (11). We note that this is a very good index match to the fused silica windows used to interface between the PC and FLCs. The major refractive index mismatch in the stack is the PC to fused silica interface at 0.2% single surface magnitudes. Note that the $n = 1.3$ oil mismatches the MgF_2 crystals by roughly 0.08 index at visible wavelengths producing a 0.10% to 0.14% single-surface reflection. Had DKIST used this $n = 1.46$ oil with the $n = 1.55$ crystal quartz, we would have seen a 0.08% to 0.01% single-surface reflection and suppressed fringes in the SiO_2 crystals to below the magnitude predicted for the MgF_2 crystals. At present, longevity under heavy UV radiation, infrared transmission properties at high-spectral resolving power, and associated heat loads remain unknown. We also note that fringes would have been further suppressed with uncoated crystals and this new oil than with the existing single layer isotropic MgF_2 coatings and $n = 1.3$ oil as applied to the DKIST SiO_2 optics. The VTF modulators nominally use a nonstandard FLC from MLO of material type we designate type A. This material showed some retardance dependence on voltage, which is not typical of traditional FLCs. MLO measured the retardance in a cell with a 3.12-μm-thick gap. The VTF FLCs were subsequently fabricated with a smaller gap.

Several studies show that FLCs have very high birefringence with refractive indices in the range of 1.4 to 1.6 for the ordinary beam and 1.7 to 1.9 for the extraordinary beam. We adopt a nominal Cauchy equation for the Cargille oil used in the VTF modulator from Eq. (11) as a reasonable starting point for the calculation of FLC refractive indices. With the measured retardance, measured cell thickness, and the ordinary beam refractive index, we can determine the birefringence and hence the refractive index required for the extraordinary beam. Figure 61 shows the derived refractive indices for FLC material A using these assumptions in (a). The extraordinary beam is in the range of 1.7 to 1.8 while the ordinary beam is around 1.5. Example FLC refractive index measurements can be seen in Fig. 19.[85]

MLO delivered two of these PC retarders to the VTF team. With a 35:1 aspect ratio, the adhesive layer is anticipated to be thicker as less force can be applied to the stack per MLO staff. We approximate the thickness as 30 μm, greater than the 14 μm found above. Table 28 summarizes the transmitted wavefront properties. One part had a 22.6 arc sec beam deviation and relatively better transmitted wavefront properties. The part had 0.38 waves power and 0.69 waves astigmatism. The remaining irregularity was 0.97 waves P-V and 0.19 waves rms with both power and astigmatism removed. The second part had 16.5 arc sec beam deviation with 3.03 waves power and 0.53 waves astigmatism. The remaining irregularity was 3.30 waves P-V and 0.88 waves rms with both power and astigmatism removed.

Figure 61(b) shows a third-order polynomial fit to the MLO measured retardance data on FLC material type A in solid black. The retardance is roughly two waves at a 400-nm wavelength

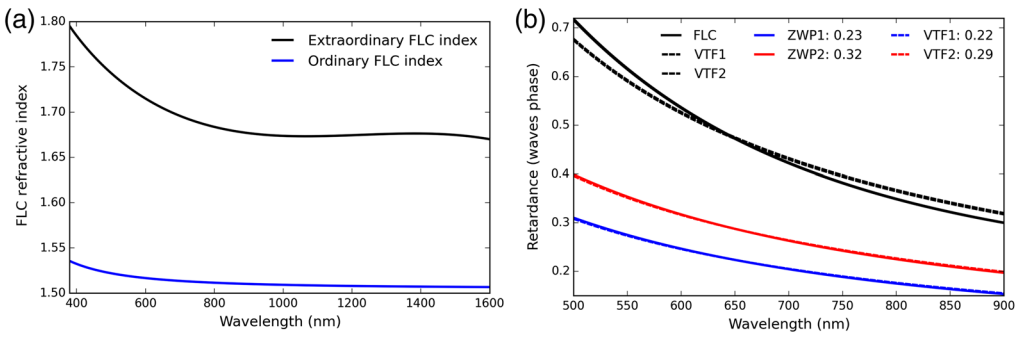

Fig. 61 (a) The refractive indices estimated for the extraordinary and ordinary beams through the FLC material in the fringe model. (b) The retardance spectra for the FLC and polycarbonate components.

Table 28 VTF PolyCarb TWE.

Optic	BD (arc sec)	Pwr	Ast	P-V	RMS
PolyC 1	22.6	0.38	0.69	0.97	0.19
PolyC 2	16.5	3.03	0.53	3.30	0.88

giving an 800-nm phase retardance. MLO measured 10 wavelengths spaced between 400 and 1600 nm wavelengths. We also show the nominal PC retardance for each zero-order retarder as blue and red in the righthand graphic of Fig. 61. We use the nominal PC retardance of 0.22 and 0.28 waves and FLC retardance of 0.5 waves at the 650-nm wavelength.

Table 29 shows the material stack used in the Berreman fringe calculation. Fused silica is used for the 10 windows included in the design. The ferroelectric liquid crystal material is denoted FLC. The refractive index matching liquid is denoted oil and is chosen by the VTF team. Oil thickness values measured at DKIST are in the range of 5 to 20 μm and we denote 10 μm as a nominal value. The PC zero-order retarder material is denoted PolyCarb. Thickness values for PC retarders depend a lot on the manufacturer, required stretching, and part wavelength range. We use 125 μm for the nominal value as MLO was almost exclusively using material of this thickness during the time these VTF retarders were ordered. The stretch reduces this by only a few microns. The adhesive bonding the PC to the windows is the same Summers P92 as our other PC parts and is denoted Adh. The refractive index for this epoxy can be chosen to either match the PC and make the low-frequency fringes faster or it can be an intermediate index between the fused silica and the PolyCarb to modify fringe magnitudes. Thicknesses can range from as low as 20 μm to over 100 μm depending on the properties of the chosen cement. We use 50 μm as a nominal value. The as-built PC retarders were measured with calipers to give total thicknesses of 4320 and 4350 μm, respectively. The windows were ordered with a 2 ± 0.1-mm thickness specification and these also passed caliper tests. Given the total thickness of the stack, we attribute a nominal 2050 μm physical thickness to the windows in the PC retarders.

The FLC material is spaced between 12.7-mm-thick fused silica windows in the VTF design. Spacing of the FLC cell was chosen to achieve the nominal half-wave retardance at a 650-nm wavelength using the measured birefringence. The Meadowlark measurements combined with our assumed refractive index calculations above solve for a 1.7146-μm physical thickness of the FLC when using refractive indices around 1.8 for the extraordinary beam and 1.5 for the ordinary beam following Eq. (11).

Following the design of the Polarimetric Littrow Spectrograph[28,39,40,86] for the Vacuum Tower Telescope and for GREGOR, the modulator has wedged exterior window to air interfaces. In the VTF design of Table 29, these windows are denoted as wedged with a subscript (fused silica$_{\mathrm{wdg}}$). The wedge on the exterior window reduces ghosting as the modulator is mounted near an

Table 29 VTF stack.

Layer	T (μm)
AR	0.1
Fused silica$_{w15'}$	10000.0
Oil	10.0
Fused silica	12700.0
FLC 1	1.7
Fused silica	12700.0
Oil	10.0
Fused silica	2050.0
Adh	30.0
PolyCarb 1	125.0
Adh	30.0
Fused silica	2050.0
Oil	10.0
Fused silica	12700.0
FLC 2	1.7
Fused silica	12700.0
Oil	10.0
Fused silica	2050.0
Adh	30.0
PolyCarb 2	125.0
Adh	30.0
Fused silica	2000.0
Oil	10.0
Fused silica$_{w15'}$	10000.0
AR	0.1

intermediate focal plane. In addition, the larger amplitude fringes are moved to a higher spectral frequency as the largest amplitude back-reflection component is from the air to glass interfaces. Provided the internal materials are all close in refractive index, the fringe components from these internal reflections will be reduced. As we showed above in Fig. 24, we can expect an index mismatch between PC and fused silica of order 0.2%, which gives rise to fringes at 0.8% in a collimated beam. The $F/40$ beam focal ratio for VTF should mitigate the internal fringes from the mismatch between the PC and the fused silica.

The broadband AR coatings are denoted AR and the formula is unknown. For now, we assume a single layer of isotropic MgF_2 at quarter-wave thickness for a nominal 600-nm central wavelength to create a simple Berreman model for a collimated beam. This gives a physical thickness of 108 nm for this AR coating. Figure 62 shows the ER components of the fringed Berreman model. The BBAR coating in VTF does not need to cover a wide wavelength range and provides quite good reflection suppression in the 500- to 900-nm bandpass. The model shows no individual wavelength with a reflection above 0.5% for a single surface with near zero reflection at the 630-nm wavelength. However, we have shown extensively that the as-built

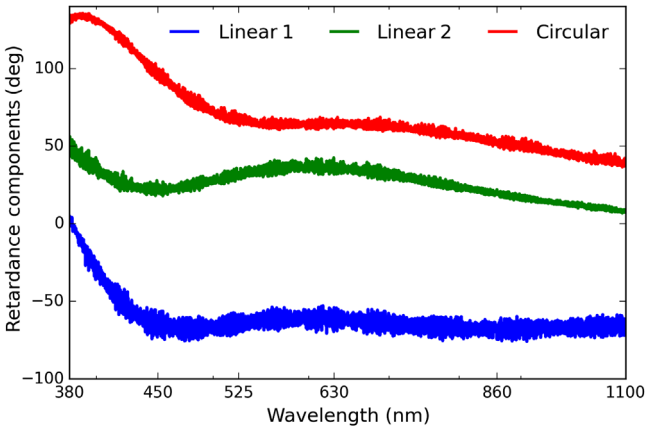

Fig. 62 The ER components in the fringed Berreman model for the VTF modulator, ignoring wedges, and with a simple coating approximation.

coatings can be quite different from a model, and the internal interfaces represent a significant contribution to fringe magnitudes. The wedged entrance and exit interfaces do indeed suppress fringes significantly. However, the remaining internal interfaces are plane-parallel and we do expect some fringes in the data, mitigated by the $F/40$ beam. These models provide the basis for the fringe periods and thermal sensitivities when the instrument is installed at DKIST.

Acknowledgments

This work was supported by the National Science Foundation's Daniel K Inouye Solar Telescope project (DKIST). Amanda White acknowledges funding from the George Ellery Hale Graduate Fellowship at the University of Colorado Boulder. Thanks goes to MLO staff, the metrology from Michael Kraemer, assistance from Larry Opila on metrology equipment, spectroscopy, data analysis, and also for numerous lengthy discussions with Tom Baur. We thank Daniel Gisler for sharing the design details, metrology, and information about the VTF modulator and testing. We thank Alfred de Wijn and Roberto Casini for their engagement in review and acceptance of this optic to upgrade the ViSP. This research made use of Astropy, a community-developed core Python package for Astronomy.[87,88]

References

1. J. P. McMullin et al., "Construction status of the Daniel K. Inouye solar telescope," *Proc. SPIE* **9145**, 914525 (2014).
2. S. L. Keil et al., "ATST: the largest polarimeter," in *Solar Polarization 6. Proc. Conf. Held in Maui*, Vol. 437, p. 319 (2011).
3. T. R. Rimmele et al., "Instrumentation for the advanced technology solar telescope," *Proc. SPIE* **5492**, 944 (2004).
4. J. Marino, E. Carlisle, and D. Schmidt, "Simulation of DKIST solar adaptive optics system," *Proc. SPIE* **9909**, 99097C (2016).
5. J. P. McMullin et al., "Construction status of the Daniel K. Inouye solar telescope," *Proc. SPIE* **9906**, 99061B (2016).
6. L. C. Johnson et al., "Status of the DKIST system for solar adaptive optics," *Proc. SPIE* **9909**, 99090Y (2016).
7. D. F. Elmore, S. R. Sueoka, and R. Casini, "Performance of polarization modulation and calibration optics for the Daniel K. Inouye Solar Telescope," *Proc. SPIE* **9147**, 91470F (2014).
8. D. F. Elmore et al., "The Daniel K. Inouye solar telescope first light instruments and critical science plan," *Proc. SPIE* **9147**, 914707 (2014).
9. W. Schmidt et al., "A two-dimensional spectropolarimeter as a first-light instrument for the Daniel K. Inouye solar telescope," *Proc. SPIE* **9147**, 91470E (2014).

10. H. Socas-Navarro et al., "High precision polarimetry with the advanced technology solar telescope," *Proc. SPIE* **5901**, 590105 (2005).
11. S. R. Sueoka, R. A. Chipman, and D. F. Elmore, "Characterization of DKIST retarder components with polarization ray tracing," *Proc. SPIE* **9293**, 929308 (2014).
12. W. H. Schubert, E. Petrak, and T. G. Baur, "Measurement of polarization assemblies for the Daniel K. Inouye solar telescope," *Proc. SPIE* **9369**, 93690N (2015).
13. A. G. de Wijn et al., "Preliminary design of the visible spectro-polarimeter for the advanced technology solar telescope," *Proc. SPIE* **8446**, 84466X (2012).
14. D. F. Elmore et al., "Utilization of redundant polarized solar spectra to infer the polarization properties of the new generation of large aperture solar telescopes," *Proc. SPIE* **7735**, 77354E (2010).
15. J. Sánchez-Capuchino et al., "Current concept for the 4-m European Solar Telescope (EST) optical design," *Proc. SPIE* **7733**, 773336 (2010).
16. F. C. M. Bettonvil et al., "The polarization optics for the European Solar Telescope (EST)," *Proc. SPIE* **7735**, 77356I (2010).
17. M. Collados et al., "European Solar Telescope: project status," *Proc. SPIE* **7733**, 77330H (2010).
18. M. De Juan Ovelar et al., "Instrumental polarisation at the Nasmyth focus of the E-ELT," *Astron. Astrophys.* **562**, A8 (2014).
19. F. Joos et al., "Reduction of polarimetric data using Mueller calculus applied to Nasmyth instruments," *Proc. SPIE* **7016**, 70161I (2008).
20. C. U. Keller and F. Snik, "Polarimetry from the ground up," in *Solar Polarization 5: In Honor of Jan Stenflo ASP Conf. Ser.*, Vol. 405, p. 371 (2009).
21. C. U. Keller et al., "EPOL: the exoplanet polarimeter for EPICS at the E-ELT," *Proc. SPIE* **7735**, 77356G (2010).
22. C. U. Keller, "Solar polarimetry close to the diffraction limit," *Proc. SPIE* **4843**, 100 (2003).
23. M. Rodenhuis et al., "The extreme polarimeter: design, performance, first results and upgrades," *Proc. SPIE* **8446**, 84469I (2012).
24. R. Roelfsema et al., "The ZIMPOL high-contrast imaging polarimeter for SPHERE: design, manufacturing, and testing," *Proc. SPIE* **7735**, 77354B (2010).
25. J. S. Almeida, "Instrumental polarization in the focal plane of telescopes. 2: effects induced by seeing," *Astron. Astrophys.* **292**, 713–721 (1994).
26. J. S. Almeida and V. M. Pillet, "Instrumental polarization in the focal plane of telescopes," *Astron. Astrophys.* **260**, 543–555 (1992).
27. J. S. Almeida, V. M. Pillet, and A. D. Wittmann, "The instrumental polarization of a Gregory-Coude telescope," *Sol. Phys.* **134**, 1–13 (1991).
28. W. Schmidt et al., "POLIS: a spectropolarimeter for the VTT and for GREGOR," *Astron. Nachr.* **324**, 300 (2003).
29. F. Snik et al., "Design of a full-Stokes polarimeter for VLT/X-shooter," *Proc. SPIE* **8446**, 844625 (2012).
30. F. Snik et al., "The upgrade of HARPS to a full-Stokes high-resolution spectropolarimeter," *Proc. SPIE* **7014**, 70140O (2008).
31. F. Snik, "Calibration strategies for instrumental polarization at the 10^{-5} level," *Proc. SPIE* **6269**, 62695P (2006).
32. H. Socas-Navarro et al., "Characterization of telescope polarization properties across the visible and near-infrared spectrum. Case study: the Dunn Solar Telescope," *Astron. Astrophys.* **531**, A2 (2011).
33. H. Socas-Navarro, "Polarimetric calibration of large-aperture telescopes. II. Subaperture method," *J. Opt. Soc. Am. A* **22**, 907 (2005).
34. H. Socas-Navarro, "Polarimetric calibration of large-aperture telescopes. I. Beam-expansion method," *J. Opt. Soc. Am. A* **22**, 539 (2005).
35. P. Spano et al., "Optical design of CAOS: a high-resolution spectropolarimeter for the Catania Astrophysical Observatory 0.91-m telescope," *Proc. SPIE* **5492**, 373 (2004).
36. K. G. Strassmeier et al., "PEPSI: the Potsdam Echelle polarimetric and spectroscopic instrument for the LBT," *Proc. SPIE* **7014**, 70140N (2008).

37. K. G. Strassmeier et al., "PEPSI spectro-polarimeter for the LBT," *Proc. SPIE* **4843**, 180 (2003).
38. J. Tinbergen, "Accurate optical polarimetry on the Nasmyth platform," *Publ. Astron. Soc. Pac.* **119**, 1371–1384 (2007).
39. C. Beck et al., "A polarization model for the German Vacuum Tower Telescope from in situ and laboratory measurements," *Astron. Astrophys.* **443**, 1047–1053 (2005).
40. C. Beck et al., "Polarimetric Littrow spectrograph—instrument calibration and first measurements," *Astron. Astrophys.* **437**, 1159–1167 (2005).
41. D. M. Harrington and S. R. Sueoka, "Polarization modeling and predictions for DKIST part 1: telescope and example instrument configurations," *J. Astron. Telesc. Instrum. Syst.* **3**, 018002–20 (2017).
42. D. M. Harrington, J. R. Kuhn, and A. L. Ariste, "Daytime sky polarization calibration limitations," *J. Astron. Telesc. Instrum. Syst.* **3**, 018001 (2017).
43. D. M. Harrington and S. R. Sueoka, "Polarization modeling and predictions for DKIST part 3: focal ratio and thermal dependencies of spectral polarization fringes and optic retardance," *J. Astron. Telesc. Instrum. Syst.* **4**(1), 018006 (2018).
44. D. W. Berreman, "Optics in stratified and anisotropic media: 4 × 4-matrix formulation," *J. Opt. Soc. Am.* **62**, 502 (1972).
45. M. W. McCall, I. J. Hodgkinson, and Q. Wu, *Birefringent Thin Films and Polarizing Elements*, 2nd ed., Vol. **1**, Imperial College Press, London (2014).
46. D. M. Harrington and S. R. Sueoka, "Polarization modeling and predictions for Daniel K. Inouye Solar Telescope part 4: calibration accuracy over field of view, retardance spatial uniformity, and achromat design sensitivity," *J. Astron. Telesc. Instrum. Syst.* **4**, 044006 (2018).
47. J. Selbing, "SST polarization model and polarimeter calibration," Master's Thesis, Dissertation, Stockholm (2005).
48. D. M. Harrington, S. R. Sueoka, and A. J. White, "Polarization modeling and predictions for DKIST part 5: impacts of enhanced mirror and dichroic coatings on system polarization calibration," *J. Astron. Telesc. Instrum. Syst.* **5**, 1–57 (2019).
49. M. Semel, "Spectropolarimetry and polarization-dependent fringes," *Astron. Astrophys.* **401**, 1–14 (2003).
50. D. Clarke, "Interference effects in compound and achromatic wave plates," *J. Opt. A: Pure Appl. Opt.* **6**, 1041–1046 (2004).
51. D. Clarke, "Effects in polarimetry of interference within wave plates," *Astron. Astrophys.* **434**, 377–384 (2005).
52. D. Clarke, "Interference effects in single wave plates," *J. Opt. A Pure Appl. Opt.* **6**, 1036–1040 (2004).
53. D. Clarke, "Interference effects in Pancharatnam wave plates," *J. Opt. A Pure Appl. Opt.* **6**, 1047–1051 (2004).
54. D. Clarke, *Stellar Polarimetry*, John Wiley & Sons, Weinheim, Germany (2009).
55. O. S. Heavens, *Optical Properties of Thin Solid Films (Dover Books on Physics)*, Dover, New York (1965).
56. D. K. Aitken and J. H. Hough, "Spectral modulation, or ripple, in retardation plates for linear and circular polarization," *Publ. Astron. Soc. Pac.* **113**, 1300 (2001).
57. T. J. Harries and I. D. Howarth, "Linear spectropolarimetry of the Hα emission line of ζ Puppis," *Astron. Astrophys.* **310**, 533 (1996).
58. D. M. Harrington et al., "Correcting systematic polarization effects in Keck LRISp spectropolarimetry to 0.05 percent," *Publ. Astron. Soc. Pac.* **127**, 757–775 (2015).
59. A. Derks, C. Beck, and V. Martinez Pillet, "Inferring telescope polarization properties through spectral lines without linear polarization," *Astron. Astrophys.* **615**, A22 (2018).
60. F. Snik et al., "A multi-domain full-Stokes polarization modulator that is efficient for 300–2500 nm spectropolarimetry," *Proc. SPIE* **9613**, 96130G (2015).
61. E. Collett, *Polarized light. Fundamentals and Applications*, 1st ed., Vol. **1**, CRC Press, Boca Raton, Florida (1992).
62. R. A. Chipman, "Polarimetry," Chapter 15 in *Handbook of Optics*, 3rd ed., Vol. **1**, pp. 14.1–14.44, McGraw Hill, New York (2014).

63. R. A. Chipman, "Mueller matrices," Chapter 14 in *Handbook of Optics*, 3rd ed., Vol. **1**, pp. 15.1–15.46, McGraw Hill, New York (2010).
64. F. Snik and C. U. Keller, *Astronomical Polarimetry: Polarized Views of Stars and Planets*, 2nd ed., Vol. **1**, Springer, Dordrecht (2013).
65. D. M. Harrington et al., "Polarization modeling and predictions for DKIST part 2: application of the Berreman calculus to spectral polarization fringes of beamsplitters and crystal retarders," *J. Astron. Telesc. Instrum. Syst.* **3**, 048001 (2017).
66. M. Born and E. Wolf, *Principles of Optics*, 7th ed., Cambridge University Press, Cambridge (1999).
67. P. Hariharan, *Basics of Interferometry*, 2nd ed., Academic Press, Burlington (2007).
68. S. Bäumer, *Handbook of Plastic Optics*, Vol. **2**, John Wiley & Sons, Hoboken, New Jersey (2011).
69. G. Ghosh, *Handbook of Thermo-Optic Coefficients of Optical Materials with Applications*, Academic Press, San Diego (1998).
70. S. N. Kasarova, N. G. Sultanova, and I. D. Nikolov, "Temperature dependence of refractive characteristics of optical plastics," *J. Phys. Conf. Ser.* **253**, 012028 (2010).
71. N. Sultanova, S. Kasarova, and I. Nikolov, "Dispersion properties of optical polymers," *Acta Phys. Pol. A* **116**, 585 (2009).
72. N. G. Sultanova, S. N. Kasarova, and I. D. Nikolov, "Optical properties of plastic materials for medical vision applications," *J. Phys. Conf. Ser.* **398**, 012030 (2012).
73. J. C. del Toro Iniesta and M. Collados, "Optimum modulation and demodulation matrices for solar polarimetry," *Appl. Opt.* **39**, 1637 (2000).
74. S. Tomczyk et al., "Wavelength-diverse polarization modulators for Stokes polarimetry," *Appl. Opt.* **49**, 3580–3586 (2010).
75. F. Snik, T. Karalidi, and C. Keller, "Spectral modulation for full linear polarimetry," *Appl. Opt.* **48**(7), 1337–1346 (2009).
76. G. van Harten et al., "Atmospheric aerosol characterization with a ground-based SPEX spectropolarimetric instrument," *Atmos. Meas. Tech.* **7**, 4341–4351 (2014).
77. G. van Harten et al., "Prototyping for the spectropolarimeter for planetary EXploration (SPEX): calibration and sky measurements," *Proc. SPIE* **8160**, 81600Z (2012).
78. F. Snik et al., "SPEX: the spectropolarimeter for planetary exploration," *Proc. SPIE* **7731**, 77311B (2010).
79. S. Sueoka, "Polarization optical components of the Daniel K. Inouye solar telescope," PhD Thesis, University of Arizona (2016).
80. D. Harrington, J. R. Kuhn, and R. Nevin, "Calibrating and stabilizing spectropolarimeters with charge shuffling and daytime sky measurements," *Astron. Astrophys.* **578**, A126–A120 (2015).
81. D. M. Harrington, J. R. Kuhn, and S. Hall, "Deriving telescope Mueller matrices using daytime sky polarization observations," *Publ. Astron. Soc. Pac.* **123**, 799 (2011).
82. D. M. Harrington et al., "Achromatizing a liquid-crystal spectropolarimeter: retardance vs. Stokes-based calibration of HiVIS," *Publ. Astron. Soc. Pac.* **122**, 420 (2010).
83. D. M. Harrington and J. R. Kuhn, "Spectropolarimetric observations of Herbig Ae/Be Stars. I. HiVIS spectropolarimetric calibration and reduction techniques," *Publ. Astron. Soc. Pac.* **120**, 89–117 (2008).
84. D. M. Harrington, J. R. Kuhn, and K. Whitman, "The new HiVIS spectropolarimeter and spectropolarimetric calibration of the AEOS telescope," *Publ. Astron. Soc. Pac.* **118**, 845 (2006).
85. J. Li, "Refractive indices of liquid crystals and their applications in display and photonic devices," PhD Thesis (2005).
86. A. Hofmann and J. Rendtel, "Polarimetry with GREGOR," *Proc. SPIE* **4843**, 112 (2003).
87. Astropy Collaborationet al., "The Astropy project: building an inclusive, open-science project and status of the v2.0 core package," arXiv.org, p. 123 (2018).
88. Astropy Collaboration et al., "Astropy: a community python package for astronomy," arXiv:1307.6212, p. A33 (2013).

Biographies of the authors are not available.